2016

Thermoelectric Properties of Novel Layered Transition-Metal Compounds

Zhenyu Diao
Louisiana State University and Agricultural and Mechanical College

THERMOELECTRIC PROPERTIES OF NOVEL LAYERED TRANSITION-METAL COMPOUNDS

A Dissertation

Submitted to the Graduate Faculty of the
Louisiana State University and
Agricultural and Mechanical College
in partial fulfillment of the
requirements for the degree of
Doctor of Philosophy

in

The Department of Physics and Astronomy

by
Zhenyu Diao
B.S., University of Science and Technology of China, 2008
M.S., The Chinese University of Hong Kong, 2010
December 2016

Acknowledgements

I wish to express my sincere gratitude to my advisor, Dr. Rongying Jin who provides me with the opportunity to study science and fundamental research in condensed matter physics. I wish to thank her for the scientific insight and endlessly help throughout my Ph.D. study. I also feel grateful for her mental guidance and for her willingness to develop me to be professional. I greatly benefit from not only the scientific instructions but also the mental help to assist me to finish my dissertation.

I would like to send my thanks to my committee members: Dr. Ward Plummer, Dr. Jiandi Zhang, Dr. David Young, and Dr. Suniti Karunatillake for their reviews and suggestions to my dissertation.

I feel grateful to our big group led by Dr. Plummer, Dr. Zhang and Dr. Jin. I benefit a lot from the journal club and the discussions among the group members. I also wish to send my thanks to all my colleagues: Amar B. Karki, Biao Hu, Jiayun Pan, Guixin Cao, Chetan Dhital, Silu Huang, Guorong Li, Chen Chen, Fangyang Liu, Lina Chen, Hangwen Guo, Jisun Kim, Zhenyu Zhang, Yifan Yang, Mohammad Sahgayezhian, Joel Taylor, Gaomin Wang, Weimei Xie.

I wish to acknowledge my collaborators at LSU: Dr. Shane Stadler, Ahmad Ikhwan Us Saleheen for powder X-ray diffraction and high temperature magnetic property measurement using SQUID; Nele Muttik for WDS measurement; Dr. Cao and Dr. Wu for EDX measurement; Dr.William Phelan for single crystal XRD. Also I would like to thank my collaborators in Oak Ridge National Lab: Dr. H.N. Lee and Dr. M. Chisholm for the thin film growth and characterizations, Huibo Cao and Qiang Zhang for single crystal neutron scattering measurement and data analysis.

At last, I would like to express my most heartfelt gratitude to my family members, for their endless love, support during the past of my life.

Table of Contents

List of Tables

List of Figures

Abstract

This dissertation is designed to search for new good thermoelectric materials. Considering that both the low dimensionality and high spin entropy are in favor of thermoelectric performance, we focused on several layered transition-metal compounds including $Bi_2Sr_2Co_2O_{9-\delta}$, $Sr_3(Ru_{1-x}Mn_x)_2O_7$, $BaMn_2Sb_2$ and $Ba_2Mn_3Sb_2O_2$. By investigating their structural, electrical and thermal transport, and magnetic properties, we discuss the relationship between structure, thermoelectric, and magnetic properties in these materials.

For $Bi_2Sr_2Co_2O_{9-\delta}$, both single crystal and thin film forms were studied. Among all films, the film grown 675 ℃ has the best power factor (S^2/ρ, where S is Seebeck coefficient and ρ is electrical resistivity), which is also much higher than those of single crystals. By annealing single crystal in Ar-atmosphere, S was enhanced while ρ was increased. Together with the almost unchanged thermal conductivity (κ), figure of merit ZT ($Z=S^2/\rho\kappa$) of the annealed single crystal becomes smaller.

For $Sr_3(Ru_{1-x}Mn_x)_2O_7$, Mn doping causes metal-insulator transition with much higher ρ. On the other hand, S is found to be slightly enhanced, possibly caused by the improvement of symmetry and increase of degeneracy of Ru by reduction of rotation angle of RuO_6-octahedra upon Mn doping. Although Mn doping decreases ZT, the dramatic change of ρ with almost unchanged S provides another route to achieve high ZT.

S of $BaMn_2Sb_2$ is relatively small with twice sign changes, due to coexistence of both types of carriers. Both ρ and κ decrease with increasing temperature. With no structural transition observed from 6 K to 780 K in the single crystal neutron scattering measurement, $BaMn_2Sb_2$ is found to be a G type antiferromagnet (T_N = 443 K) with easy axis along c direction. Obtained β

is 0.34 (1) which is consistent with 3D Ising model, indicating 3D magnetic structure in the layered crystal structure.

Compared to layered $BaMn_2Sb_2$, $Ba_2Mn_3Sb_2O_2$ has another Mn-O layer in addition to alternative Ba layer and Mn-Sb layer. S also changes sign twice. In contrast to $BaMn_2Sb_2$, ρ and κ has opposite trend with much smaller magnitudes. From single crystal neutron scattering measurement, $Ba_2Mn_3Sb_2O_2$ is found to have two spin sublattice. Mn(2) (Mn-Sb) exhibits G-type antiferromagnetism with T_N = 314 K while Mn(1) (Mn-O) has a new magnetic ordering below 40 K.

Chapter 1 Introduction

1.1 Fundamentals of Thermoelectricity

Energy crisis has been a critical issue for long time. The energy need is increasing over year and year. However, over two-thirds of used energy is lost as waste heat.[1] Likewise, the global climate change due to the combustion of fossil fuels to satisfy energy demand is becoming impending. Renewable energy has been proposed to provide electricity needs and to slash the greenhouse pollution coming from fossil fuel consumption. Using thermoelectric materials to convert waste heat from home heating, automotive exhaust and industrial process into electricity is one way for energy recycling. The thermoelectric generators are silent and reliable solid-state devices without moving parts. They are environment friendly without the production of deleterious waste. They are also scalable and thus suitable for small, distributed power generation. For example, the automotive industry is developing the thermoelectric generators using waste heat from engines, exhaust systems and radiators. Moreover, some novel applications have been proposed, including biothermal batteries to power heart pacemaker and radioisotope thermoelectric power generator for deep-space probes. Similarly, the thermoelectric materials could be used as Peltier coolers to replace the compression-based refrigeration. They are quite suitable for the small scale, localized cooling of small components, such as computer processors, electronic devices and infrared detectors.

A thermoelectric generator is based on Seebeck effect that voltage difference generates between two dissimilar materials with the presence of a temperature gradient. It can be described as

$$S = \Delta V/\Delta T \qquad 1.1$$

where S refers to the Seebeck coefficient or Seebeck coefficient; ΔV and ΔT denote the voltage and temperature difference, respectively. The route to generate electricity by utilizing heat source is as shown in Figure 1-1 (a). The heat source creates a temperature gradient that drives both types of charge carriers to diffuse from the hot side to the cold side, resulting in electrical current I in the circuit. This can be understood as followings. Fermi-Dirac distribution f(E, T) = $\frac{1}{e^{(E-\mu)/k_B T}+1}$ describes the number of carriers as a function of energy levels and temperature. At higher temperatures, the carriers would have higher concentrations above Fermi energy, establishing a concentration gradient along temperature gradient. Moreover, electrons at higher temperatures would have larger momentum. The higher concentration and larger momentum at higher temperatures lead to the diffusion of carriers from high temperature region to low temperature region. As holes in the left and electrons flow from the hot side to cold side, electrical current is generated in the circuit. Conversely, heat flow accompanies with the electrical current which can be described as Q = ΠI, where Q and I are the heat flow and the electrical current, and Π denotes the Peltier coefficient. As shown in Figure 1-1 (b), an anticlockwise current flows in the circuit. Both holes in the left and electrons in the right flow from upper junction to the lower junction, generating two heat flow from upper to lower junctions. Hence the upper junction is cooled while the lower junction is heated. The heat sink helps to release the heat. For all non-magnetic materials in the absence of an externally applied magnetic field, the Seebeck coefficient and Peltier coefficient are related by the second Thomson relation.

$$S = \Pi/T \qquad 1.2$$

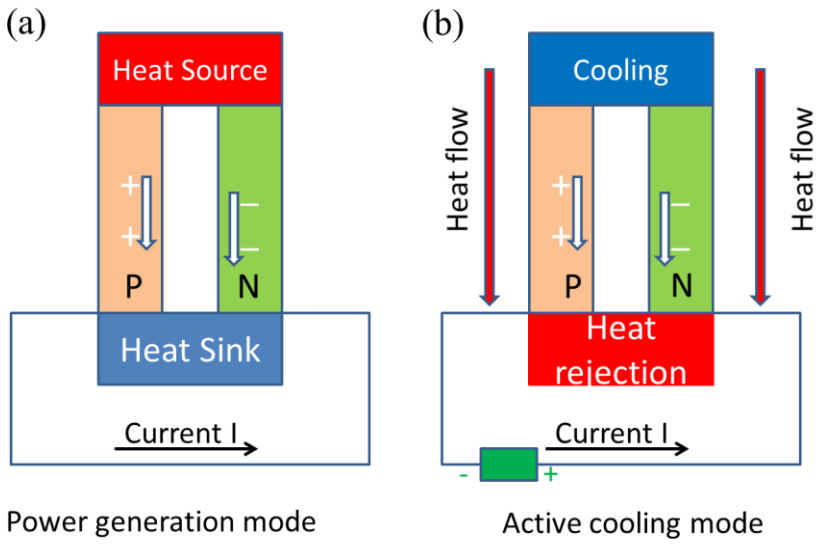

Figure 1-1 Schematic illustrations of thermoelectric power generation (Seebeck Effect) (a) and refrigeration (Peltier Effect) (b). P and N represent the p type and n type carriers, respectively.

The efficiency of a thermoelectric device depends on system parameters, such as the applied voltage or load resistance, hot and cold side temperatures, and the length and area of the thermoelectric parts. We can study the intrinsic thermoelectric properties of thermoelectric materials to improve the performance of thermoelectric devices. In the most simplified cases, the efficiency of a single thermoelectric element can be obtained in terms of only intrinsic variables including no external parameters. The calculated efficiency for power generation η is [2]

$$\eta = \frac{T_H - T_C}{T_H}\left\{\frac{(1+ZT_M)^{\frac{1}{2}}-1}{(1+ZT_M)^{\frac{1}{2}}+\left(\frac{T_C}{T_H}\right)}\right\} \qquad 1.3$$

where T_H and T_C are the temperatures at hot and cold sides, T_M is the average temperature, $\frac{T_H - T_C}{T_H}$ is the Carnot efficiency for a reversible heat engine and the thermoelectric parameter Z is defined as:

$$Z=S^2\sigma/\kappa \quad (1.4)$$

where σ is the electrical conductivity and κ represents the thermal conductivity. ZT_M is called figure of merit which determines the efficiency of a thermoelectric generator with the fixed external parameters. Similarly, the efficiency for thermoelectric refrigeration in the simplest case is [2]

$$\phi = \frac{T_C}{T_H - T_C}\left\{\frac{(1+ZT_M)^{\frac{1}{2}} - \frac{T_H}{T_C}}{(1+ZT_M)^{\frac{1}{2}}+1)}\right\} \quad (1.5)$$

Obviously, both efficiencies depend on the figure of merit ZT. When ZT approaches infinity, the efficiencies can reach the ideal Carnot efficiency. In order to obtain high efficiency, higher value of ZT is required which requires larger Seebeck coefficient and electrical conductivity but lower thermal conductivity.

1.2 Traditional Thermoelectric Materials

Traditional thermoelectric materials are usually bulk semiconductors. The electronic structures are well described by the band theory. For semiconductors with parabolic band under energy-independent scattering approximation, the Seebeck coefficient is given by

$$S = \frac{8\pi^2 k_B^2}{3eh^2} m^* T\left(\frac{\pi}{3n}\right)^{2/3} \quad (1.6)$$

where n is the carrier density and m* is the effective mass of the carrier. The electrical conductivity can be written as:

$$\sigma = ne\mu \quad (1.7)$$

where μ is the carrier mobility depending on m*. Both Seebeck coefficient and electrical conductivity depend on the carrier density. As shown in Figure 1-2, the Seebeck coefficient S would increase with decreasing carrier density while the electrical conductivity σ decreases with decreasing carrier concentration. The effective mass m* provides another barrier because larger m* gives higher S but lower σ. Conventional thermoelectric materials were usually improved by compromising between low electric resistivity and large Seebeck coefficient via adjusting carrier density. The maximum of power factor $S^2\sigma$ is estimated to be achieved at the carrier density $10^{19} \sim 10^{20}$ cm^{-3}.

Thermal conductivity consists of both contributions from lattice and electrons. Wiedemann Franz law illustrates that the electronic thermal conductivity κ_e is proportional to the electrical conductivity satisfying

$$\frac{\kappa_e}{\sigma} = L_0 T, \tag{1.8}$$

where L_0 is the Lorentz number ($L_0 = 2.45\times10^{-8}$ $W\Omega/K^2$ for free electrons). As shown in Figure 1-2, with higher carrier density, the electrical conductivity is enhanced. The increase of electrical conductivity would lead to larger electronic thermal conductivity which limits the increase of Z. Considering the effect of carrier density on Seebeck coefficient, electrical conductivity and thermal conductivity, the optimal carrier density is around 10^{20} cm^{-3} to achieve maximum of figure of merit ZT, as illustrated in Figure 1-2. We can also rewrite the figure of merit as

$$ZT = \frac{S^2}{L_0}\left(\frac{1}{1+\frac{\kappa_L}{\kappa_e}}\right) \tag{1.9}$$

which gives the two approaches to enhance the figure of merit by either increasing the Seebeck coefficient or reducing the relative lattice thermal conductivity compared to electronic thermal conductivity. The lattice thermal conductivity can be written as:

$$\kappa_L = \frac{1}{3} V_s C L_{ph}, \qquad 1.10$$

where V_s is the velocity of sound, C is specific heat and L_{ph} is the mean free path of phonons. The sound velocity and heat capacity are temperature-independent at high temperatures (Θ_D > 300 K) in typical materials. Then the phonon mean free path determines the lattice thermal conductivity. In the semiconductors discussed above, $\kappa_e << \kappa_L$ usually holds. Therefore, the large figure of merit requires reducing lattice thermal conductivity. The ideal thermoelectric materials were suggested by Slack to be "phonon-glass electron-crystal" which has the electrical properties of crystalline materials and thermal properties of glass-like materials.[3] The low lattice thermal

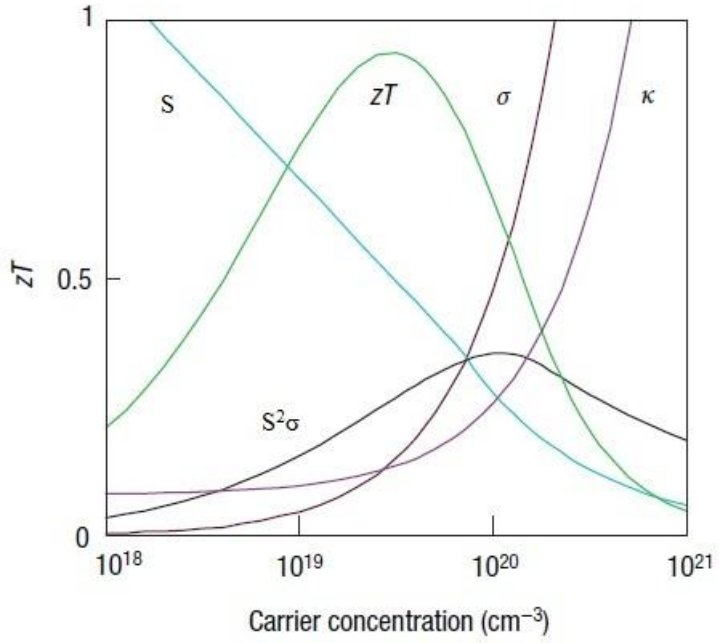

Figure 1-2 Dependence of Seebeck coefficient (S), electrical conductivity (σ), electronic thermal conductivity (κ_e), lattice thermal conductivity (κ_L) and figure of merit on carrier concentration.[4]

conductivity can be obtained in semiconductors with heavy atoms. A typical method proposed in late 1950's is to adopt the form of alloy.[5] A commercial thermoelectric cooler based on the alloys of Bi_2Te_3 and Sb_2Te_3 with a ZT value close to 1 at room temperature.[6] This value has been

a practical upper limit at room temperature for more than 30 years. Because of the interplay of Seebeck coefficient, electrical conductivity and thermal conductivity, it is quite difficult to tune them simultaneously. Yet there are no theoretical reasons for the existence of upper limit of ZT.

1.3 New Types Thermoelectric Materials with Low Dimensionality

In 1990's, the ideas that low dimensionality may improve ZT reinvigorated research on thermoelectric materials based on the realization that quantum confinement changes the degree of freedom of electrons and enhance density of states.[7] The low dimensionality may lead to new approaches for high ZT materials. In a quantum confined structure the electron bands are narrower when the confinement enhances and dimensionality decreases, leading to increased density of states at Fermi level. According to Mott relation,[8]

$$S = \frac{\pi^2 k_B T}{3e}\left\{\frac{\partial \ln \sigma(\varepsilon)}{\partial \varepsilon}\right\}_{\varepsilon=E_F} \quad 1.11$$

Assuming a temperature-independent relaxation time, σ can be approximately represented by the density of state N(ε) at the Fermi level.[8]

$$S \approx \frac{\pi^2 k_B T}{3e}\left\{\frac{\partial \ln N(\varepsilon)}{\partial \varepsilon}\right\}_{\varepsilon=E_F} \quad 1.12$$

The Seebeck coefficient depends on the slope of density of state at Fermi level. As a result, low dimensionalities may enhance the Seebeck coefficient via the enhancement of density of states near Fermi level. Moreover, the heterostructures may decouple the Seebeck coefficient and electrical conductivity explained by electron filtering model using quantum-mechanical transmission.[9] Both Seebeck coefficient and electrical conductivity could be enhanced simultaneously for high ZT. In addition, low thermal conductivity in the low dimensional materials may be achieved due to the interface scattering.

Engineered structures, such as superlattice, quantum well, quantum dots and quantum wires have been studied for given materials to improve ZT value. Theoretical calculations show that the ZT value of the Bi_2Te_3 with quantum well structures may reach 13 times of the bulk value.[7] Subsequent studies show exciting experimental realizations for ZT enhancement. The first approach was proposed that thermal conductivity can be significantly reduced in superlattices by interface scattering of phonons.[10] In 2001, Venkatasubramanian et al. reported a ZT value of about 2.4 for p-type 10 Å/50Å Bi_2Te_3/Sb_2Te_3 superlattice devices along the cross-plane direction.[11] The superlattice structures can show significantly the reduction of κ_L by tuning the thickness without much effect on the power factor $S^2\sigma$. Another approach is to obtain enhanced electronic density of states (DOS) near Fermi level by the quantum confinement. In 2007, a reported two dimensional $SrTiO_3$ confined within a unit cell layer thickness show an approximately 5 times larger S than the bulk value.[12] The best value reaches as high as 850 μV/K. Simultaneously, the σ still maintains a high value of 1.4×10^3 $S \cdot cm^{-1}$. In the superlattice structures, it is of great importance to use interfaces for blocking phonons while transmitting electrons along the cross-plane direction. The thermal conductivity can be reduced. Hence, figure of merit ZT is increased.

1.4 Layered Cobaltates with Natural Superlattice Structures

Besides the engineered structures, compounds with natural superlattice structures also attract much attention as potential thermoelectric applications. Layered cobalt oxides consist of nanoblocks with different compositions and structural symmetries. As shown in Figure 1-3, in the Na_xCoO_2, the CdI_2-type CoO_2 layer and Na layer alternatively stack along the c axis. The CoO_2 layer consists of edge-shared distorted CoO_6 octahedra with Co in the center, forming a triangular lattice. The Na content can vary from 0 to 1.0. For $Na_{0.5}CoO_2$ ($NaCo_2O_4$), half of Na

sites are vacant. $Na_{0.5}CoO_2$ with a low mobility (13 cm^2/Vs at 300 K) were reported to show unexpected large in-plane Seebeck coefficient (100 μV/K at 300K) with a low in-plane electrical resistivity (200 μΩcm at 300K), leading to the power factor comparable to the typical bulk Bi_2Te_3.[13] The high electrical conductivity and low mobility indicate high carrier density, which was confirmed by Hall coefficient measurements to be as high as 10^{21} cm^{-3} comparable to typical metals.[14] As reported, the polycrystalline $Na_{0.5}CoO_2$ has the thermal conductivity as small as the Bi_2Te_3 value.[15]

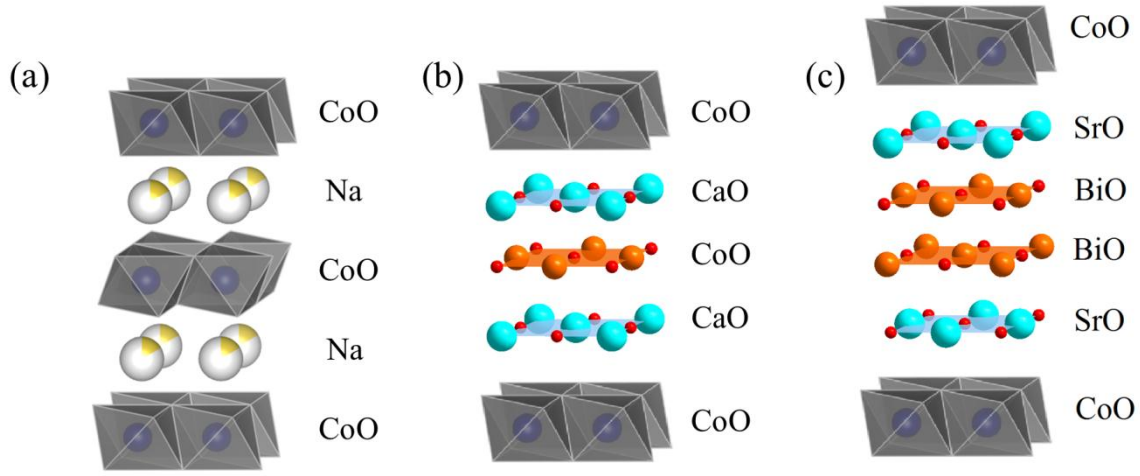

Figure 1-3 Schematic lattice structures of cobalt-based oxides: $NaCo_2O_4$, $Ca_3Co_4O_9$, $Bi_2Sr_2Co_2O_9$.

Good thermoelectric properties have been observed in Na_xCoO_2 for different x.[16, 17] The high disorder of the Na layer reduces the mean free path of phonons to the scale comparable to lattice spacing so that the lattice thermal conductivity can be minimized by the disorder in insulating Na layer which causes little effect on the electronic conduction.[18] The charge carriers are confined in the conducting CoO_2 layer, known as quantum confinement without observable

scattering of the Na layer disorder.[19] As a result, the electrical conductivity can maintain relatively high value. On the other hand, the spin entropy of the CoO_2 layer acts as the likely source for the enhancement of the Seebeck coefficient.[17] In CoO_2 layer of $Na_{0.5}CoO_2$, the average valence value of Co is 3.5. So both Co^{3+} and Co^{4+} ions exist with 6 or 5 3d-shell electrons, respectively. The d-shell orbitals would split into two energy levels under the octahedral crystal field by surrounding oxygen atoms. The first one is a triply degenerate t_{2g} band (d_{xy}, d_{yz}, d_{xz}) with lower energy while the other one is a doubly degenerate e_g band ($d_{x^2-y^2}, d_{z^2}$) with higher energy. The d electrons can be arranged with different spin states, i.e., low spin (LS), intermediate spin (IS), and high spin (HS) states illustrated in Figure 1-4. Magnetic susceptibility measurements suggest the existence of LS Co^{4+} ions with S spin ½ and LS Co^{3+} with S = 0.[17] This is also confirmed by ^{59}Co NMR studies.[20] The charge carriers in the $Na_{0.5}CoO_2$ are holes and the hopping of a hole from Co^{4+} to Co^{3+} transfer a charge +1e and a spin ½. The process creates a contribution to Seebeck coefficient by spin entropy.[17]

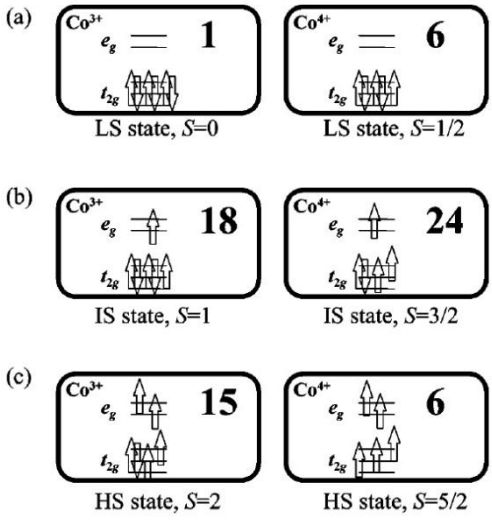

Figure 1-4 Schematic illustrations of spin states of cobalt ions Co^{3+} and Co^{4+}. The numbers in the frame represent the degeneracy of each state.[21]

Koshibae et al. have proposed that not only the degeneracies of Co^{3+} and Co^{4+} ions but also the ratio between them are crucial for the large Seebeck coefficient which can be expressed by using modified Heikes formula in the high temperature limit,[21]

$$S = -\frac{k_B}{e}\ln\left(\frac{g_3}{g_4}\frac{x}{1-x}\right) \quad 1.13$$

where g_3 and g_4 denote the degeneracies of Co^{3+} and Co^{4+} ions, and x is the concentration of Co^{4+} ions.

Considering different cases for degeneracies, the determined Seebeck coefficient are listed in Table 1-1. In the case of LS Co^{4+} ions in $Na_{0.5}CoO_2$, the Seebeck coefficient can reach 154 μV/K (as shown in Table 1-1) which satisfactorily agrees with experimental results.

Table 1-1 The obtained Seebeck coefficient Q in different cases of spin states (x=0.5).[21]

	Co^{3+}	Co^{4+}	g_3/g_4	$Q(x=0.5)$
(i)	HS	HS	15/6	-79 μV/K
(ii)	HS+LS	HS	16/6	-84 μV/K
(iii)	LS	HS+LS	1/12	214 μV/K
(iv)	LS	LS	1/6	154 μV/K
(v)	HS+LS+IS	HS+LS+IS	34/36	5 μV/K

After the striking discovery of Na_xCoO_2 as potential thermoelectric compound, the exploration of cobalt oxides began in earnest. More than ten layered cobalt-based oxides have been proposed as good thermoelectric materials. Further analysis on the structures suggests that the structural misfit may be in favor of thermoelectric performance of $Ca_3Co_4O_9$ and $Bi_2Sr_2Co_2O_9$. As shown in Figure 1-3, the CdI_2 type hexagonal CoO_2 layers (the first sublattice) and the triple rock salt type square Ca_2CoO_3 layers (the second subsystem) alternatively stack along c axis. Both sublattices have the identical a = 4.8376 Å, c = 10.833 Å, and β =98.06º

parameters but different b (Ca_2CoO_3: b = 4.5565 Å; CoO_2: b = 2.8189 Å) parameters, forming a structure misfit along the b-axis.[22, 23] By analogy with Na_xCoO_2, the CoO_2 layers are believed to be responsible for the carrier transport while the Ca_2CoO_3 layers may serve as a charge reservoir to supply charge carrier to the CoO_2 layers.[24, 25] As reported, $Ca_3Co_4O_9$ exhibit unusually large Seebeck coefficient (in-plane S=125 μV/K at 300K), which can be explained by the strongly electronic correlations in the CoO_2 layer.[26] Huang et al. found a method to further enhance the Seebeck coefficient by preparing the polycrystalline through cold-pressing and high-magnetic-field sintering. On the other hand, $Ca_3Co_4O_9$ has a smaller in-plane κ than $Na_{0.5}CoO_2$. In the cobalt-based layered oxides, the electronic contributions based on Wiedemann-Franz law are much smaller and the in-plane κ is predominately dominated by the block layers since compounds with heavier atoms exhibit lower in-plane κ.[27] The misfit block layers lead to smaller κ in the way that distorted structure makes acoustic phonon less dispersive. By doping Fe, Mn, and Cu in the Co sites, the induced structural distortion and size disorder further suppressed κ.[28] Furthermore, a small anisotropy between a and b axis of the ab plane κ in $Ca_3Co_4O_9$ was observed which is thought to be due to the misfit.[27]

Another misfit layered cobalt-base oxide $Bi_2Sr_2Co_2O_9$ has also attracted much attention. Similar to $Ca_3Co_4O_9$, $Bi_2Sr_2Co_2O_9$ consists of conducting CdI_2 type hexagonal CoO_2 layers and insulating rock salt type $Bi_2Sr_2O_4$ layers alternatively stacking along the c axis, resulting in quantum-well-like structures. Large Seebeck coefficient values (130 μV/K in single crystals and 60μV/K in bulk polycrystallines at 300K) were reported.[21, 29, 30] Further structural study revealed that there is a misfit along b axis between the two sets of layers.[31] The isomorphous misfit layer cobaltite $(Bi_{0.87}SrO_2)_2(CoO_2)_{1.82}$ was investigated and exhibits two sublattices with incommensurate periodicities along the b axis ($Bi_{0.87}SrO_2$: 5.112 Å; CoO_2: 2.8081 Å).[32] The

compatibility along the other two directions (identical a, c, and β) was confirmed by further single crystal X-ray diffraction analysis using the five-dimensional superspace-group formalism.[33] Later, large anisotropy of in-plane κ and S and finite in-plane thermal conductivity were observed experimentally. Similar to $Ca_3Co_4O_9$, the anisotropy is attributed to the structural misfit.[27] Moreover, the lattice misfit also leads to significant chemical strain along the b axis on CoO_2 layer imposed by the RS Ca_2CoO_3 layer. Density function theory suggests that applying strain on CoO_2 layer could increase the density of states near Fermi energy.[34] The enhancement of density of states can possibly increase Seebeck coefficient. A more than 15% increase of Seebeck coefficient was found in $Bi_2Sr_2Co_2O_9$ at around 50K.[29] By doping Pb cations at Bi sites ($Bi_{2-x}Pb_xSr_2Co_2O_9$), the misfitness can be tuned. Through varying the strain on CoO_2 layer, the Seebeck coefficient is enhanced by Pb doping with a maximum at x=0.4.[29, 35] Moreover, an upturn of electrical conductivity at low temperatures was observed which can be explained by the pseudogap opening in the density of states caused by the misfit structure or charge ordering of Co^{3+} and Co^{4+}.[29, 35]

These layered cobalt oxides with natural superlattice structures contain conducting CoO_2 layers. By choosing certain insulating layers, the layered cobalt oxides may be typical phonon-glass electron-crystal for thermoelectric materials. We are attempting to search for new promising thermoelectric compounds based on the two basic principles mentioned in the beginning: (1) layered structure that may have quantum confinement effect of carriers; (2) contain transition ions with different spin degeneracy that could contribute to enhance Seebeck coefficient.

1.5 Delafossite Type Cobaltite $PdCoO_2$

$PdCoO_2$ is a quasi-two-dimensional compound with triangular O-Pd-O layers and the CoO_2 layers formed by edge-shared CoO_6 octahedra alternatively stacking along the c axis, as shown in Figure 1.5(a). The Pd atoms are two fold linearly coordinated with oxygen atoms while the oxygen atoms are coordinated with three Co atoms and one Pd atom, forming a distorted tetrahedron. Previous study found that the $PdCoO_2$ is metallic with ab plane electrical conductivity significantly higher than the c axis value. [36, 37] The reported ab plane value of $PdCoO_2$ at 260 K was 4.69 μΩ cm which is the lowest value reported in the oxides, even lower than the Pd metal value 11 μΩ cm.[38] Subsequent studies tried to explore the origin of the good electrical conductivity in $PdCoO_2$.[39-41] The cobalt in the compounds is in the Co^{3+} LS state, which was confirmed by magnetic susceptibility measurements and Co-O distances as well as the Co 2p X-ray absorption spectroscopy (XAS) results.[36, 39, 42] Thus monovalent palladium is present in the delafossite compounds, which are observed experimentally for the first time. It was proposed that the metal-metal interactions in the Pd layers are responsible for the high ab plane electrical conductivity.[36, 39] By measuring the Fermi surface (FS) based on de Haas-van Alphen effects and the calculations effective mass of electrons, it is suggested that the electrical conductivity of $PdCoO_2$ is mainly due to Pd 5s overlap.[43] The resulting FS was quite consistent with theoretical calculations and angle resolved photoemission spectroscopy (ARPES) data.[38, 40] Apart from the small warping parallel to the c axis, the FS is nearly two-dimensional with almost exclusively ab plane Fermi velocities, resulting in the strong anisotropy of electrical conductivity.

Preliminary studies on thermopower showed that a rectangular form of powdered and pelletized fine $PdCoO_2$ single crystal has a thermopower value of 2 – 4 μV/K between 100 and 400 K comparable to normal conventional metal values.[44] On the other hand, Hasegawa et al.

also discussed the possibility of high thermopower based on the deep cave of the density of states at Fermi level in $PdCoO_2$.[44] Ong et al. show that $PdCoO_2$ may have large Seebeck coefficient, using Boltzmann Transport Calculations.[45] As shown in Figure 1-5(b), the ab plane Seebeck coefficient values are positive and with small amplitudes comparable to the normal good metal values. The c axis values are negative with quite large amplitudes (-200 μV/K in $PdCoO_2$ above 400 K).

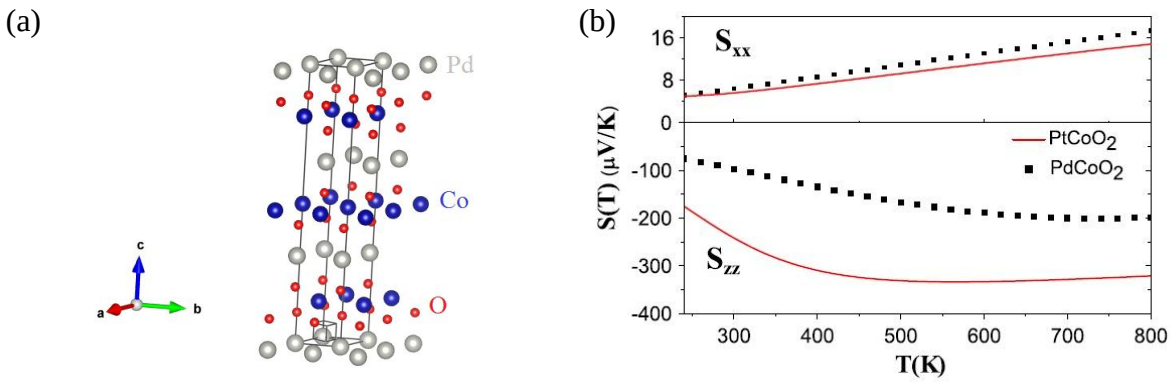

Figure 1-5 (a) Schematic picture of the crystal structure of $PdCoO_2$. (b) Calculated Seebeck coefficient in $PdCoO_2$ and $PtCoO_2$, using Boltzmann Transport Calculations. Picture extracted from Ong et. al.[45]

1.6 Layered Perovskite Ruddleden-Popper Compounds

Ruddleden-Popper compounds $Sr_{n+1}M_nO_{3n+1}$ (n=1, 2, 3… M is a transition metal) has layered structure where each layer consists of corner shared octahedral MO_6. The number n represents the number of octahedron MO_6 interlinked by oxygen atoms in the layer. Layers of ($SrMO_3$) unit cells are separated by SrO layer along the c axis, forming natural superlattice-like structures. Figure 1-6 demonstrates the crystal structure for $SrRuO_3$ (n = ∞), Sr_2RuO_4 (n = 1), $Sr_3Ru_2O_7$ (n = 2) and $Sr_4Ru_3O_{10}$ (n = 3). To better describe the crystal structure, the compounds can also be written as $SrO(SrRuO_3)_n$.

La-doped n-type perovskite $SrTiO_3$ was found to exhibit a very high Seebeck coefficient of S = 420 μV/K at room temperature.[46] But the figure of merit ZT is relatively small because of the high thermal conductivity (κ = 12 W/m-K at room temperature). Due to the high phonon frequencies of major constituent oxygen and its small mass, the lattice thermal conductivity is high. With large number of interfaces (large n) in the superlattice, the lattice thermal conductivity can be reduced through interface phonon scattering at $SrO/(SrTiO_3)_n$ internal interfaces. The total thermal conductivity was reported to be around 5 W/m-K for 5 % Nb-doped $SrO(SrTiO_3)_n$ (n = 1 and 2), significantly smaller compared to 20 % Nb doped $SrTiO_3$.[46, 47] Compared to $Sr_{n+1}Ti_nO_{3n+1}$ with insulating ground state, $Sr_{n+1}Ru_nO_{3n+1}$ have metallic ground states with high electrical conductivity.[48-51] Hence, $Sr_{n+1}Ru_nO_{3n+1}$ is possible thermoelectric candidate with promising figure of ZT. Sr-Ru-O compounds by spark plasma sintering were reported to exhibit larger S as n increases with a maximum value of 42 μV/K at 600K.[52] The reported Seebeck coefficient of $SrRuO_3$ (n = ∞) was 36 μV/K at room temperature.[53] The room temperature Seebeck coefficient for Sr_2RuO_4 (n = 1) is reported as S = 29 μV/K.[54] $Sr_4Ru_3O_{10}$ (n = 3) also has similar Seebeck coefficient values ~ 34 μV/K at room temperature.[55] However, there has been no study reported about the Seebeck coefficient of $Sr_3Ru_2O_7$ (n = 2). The relative large Seebeck coefficient values can't be explained in simple model for metal with broad bands, since the Seebeck coefficient of a simple metal is usually a few μV/K.

$Sr_3Ru_2O_7$ is a quasi 2D paramagnetic metal with the symmetry of orthorhombic space group Bbcb.[56, 57] Two blocks of distorted $SrRuO_3$ perovskite stacks along the c axis, separated by SrO layers that belong to the symmetry of space group Pban[57]. A rotation angle occurs between the neighboring corner-sharing octahedra in each double perovskite layer, e.g., the Ru-O-Ru is about 165 ° rather 180 ° for pure $Sr_3Ru_2O_7$. As revealed by powder neutron diffraction result, the

rotation angle is about 6.8 ° about the c axis, as shown in Figure 1-7, with intra- and interbilayer RuO_6 octahedra. The distorted octahedra modify the crystal field[58], providing new opportunities to tune the Seebeck coefficient by varying Fermi energy and orbital degeneracy. It is reported that the crystal symmetry restoration of distorted TiO_6 octahedra in $SrO(SrTiO_3)_2$ enhances the degeneracy in the Ti 3d orbitals that notably increases Seebeck coefficient.[59] Hence it is also of great interest to study if the Seebeck coefficient of $Sr_3Ru_2O_7$ benefits from the doping of transition metals in the Ru site.

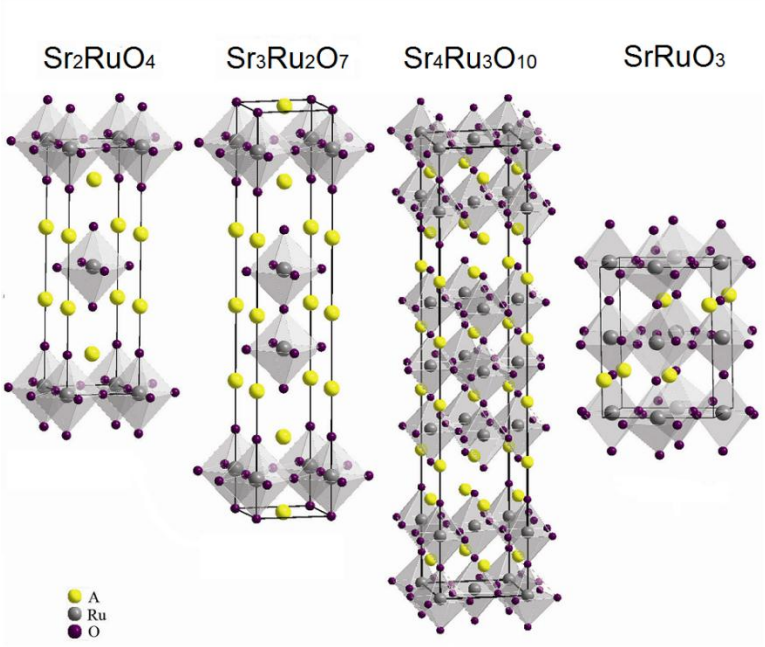

Figure 1-6 Schematic crystal structures for Sr_2RuO_4 (n = 1), $Sr_3Ru_2O_7$ (n = 2), $Sr_4Ru_3O_{10}$ (n = 3) and $SrRuO_3$ (n = ∞).

There have been studies about the structure variation of Mn doping. Upon Mn doping, the unit cell volume shrinks and the rotation angle decreases with x and becomes zero above x = 0.2.[50] Mn doping in the Ru site yields a drastic phase change, e.g., $Sr_3(Ru_{1-x}Mn_x)_2O_7$ becomes AFM insulator with certain amount of doping. Moreover, Mn doping drives the metal-insulator transition to high temperatures, though the magnetic susceptibility maximum temperature

displays nonmonotonic dependence with x. Optical conductivity spectra suggest that Mn doping narrows the bandwidth. Hence the enhanced electron-electron correlation causes the Mott-type metal-insulator transition.[60]

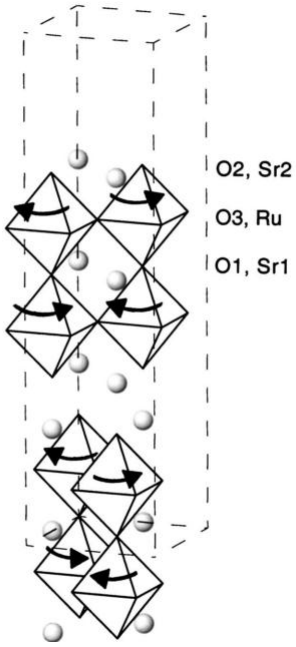

Figure 1-7 Schematic picture of crystal structure of $Sr_3Ru_2O_7$. The arrows indicate the rotations of the octahedra around the c axis, in response to the compression of RuO(3) planes by the large difference of ionic radii of Ru compared to Sr. Picture extracted from Shaked et. al.[61]

More interestingly, though X-ray absorption spectroscopy (XAS) data suggests Mn^{3+} exists in $Sr_3(Ru_{0.9}Mn_{0.1})_2O_7$, the fact that unit cell shrinks, X-ray photoelectron spectroscopy (XPS) shows no change in Ru spectra upon Mn doping and that the increase of S from 1 at x = 0 to 3/2 at x =0.7 derived from high temperature magnetic susceptibility strongly suggest that the oxidation state of Mn in doped compound is 4+, independent of the doping level x. In other words, the band filling remains unchanged. The evolution of spin configuration by Mn doping

from S = 1 to S = 3/2 at higher doping levels with different spin degeneracies provides another opportunity for enhanced Seebeck coefficient.

1.7 Layered Mn-based Compounds

As explained earlier, large ground state degeneracy favors large Seebeck coefficient. The crystal fields play important role to determine the arrangement of electrons. Besides mentioned octahedral crystal field that has triply degenerate t_{2g} bands and doubly degenerate e_g band, there are several other cases that introduce degeneracy, such as cubic, dodecahedral, tetrahedral environment. Their typical energy splitting by crystal fields are shown as Figure 1-8.

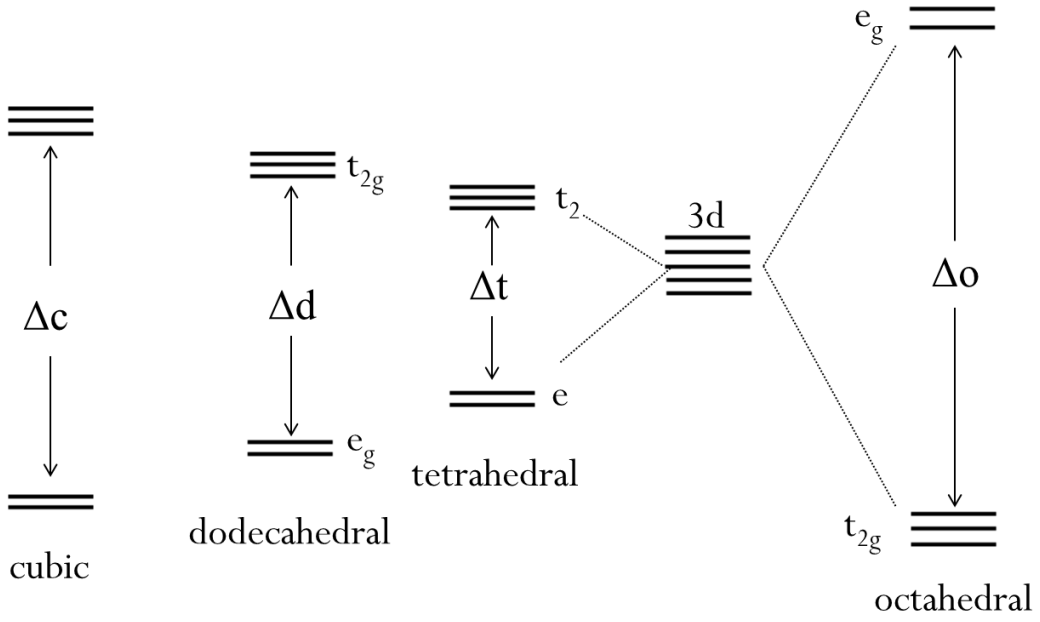

Figure 1-8 Crystal fields for d orbitals in cubic, dodecahedral, tetrahedral and octahedral coordinates.

As depicted, the energy difference Δ between the t_{2g} and e_g bands, usually called $10Δq$, is the energy required for crystal field stabilization. In general, the relationship $\Delta_t < \Delta_d < \Delta_c < \Delta_o$ applies. From this point of view, the tetrahedral crystal field would more easily adopt high spin or intermediate spin states, because the competition between Hund's Rule and Δ directly

determine the electron occupancy and small Δ yields high spin states. According to Heike's formula, multiple spin states may lead to large Seebeck coefficient. Hence, the tetrahedral crystal field could be good candidate for good thermoelectric properties. The tetrahedral crystal field can be considered as the opposite of octahedral one, as shown in Figure 1-8.

As mentioned, the origin of large Seebeck coefficient evolves the entropy change between the ions with different valence values, e.g., the Co^{3+}/Co^{4+} pair in $NaCo_2O_4$. Many other transition metals have multiple valences too, such as Cr^{2+}/Cr^{3+}, Mn^{3+}/Mn^{4+}, Mn^{2+}/Mn^{3+}, Mn^{3+}/Mn^{4+}, Co^{2+}/Co^{3+}, Fe^{3+}/Fe^{4+}. Considering a common tetrahedral structure with Mn at the center, the possible spin states for Mn^{4+}/Mn^{3+} with degeneracy are shown in Figure 1-9. The total degeneracy is calculated as degeneracy of orbitals multiplying degeneracy of spins that is equal to 2*total spin + 1. The combination of Mn^{4+} (HS) and Mn^{3+} (LS) has a degeneracy ratio of 12/1 and the calculated Seebeck coefficient is of 214 μV/K.

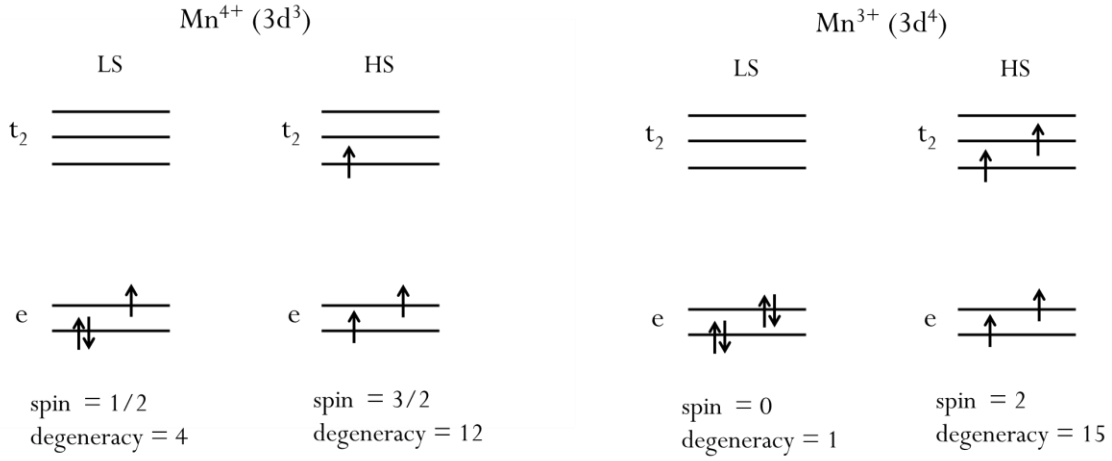

Figure 1-9 High spin and low spin states for Mn^{4+} and Mn^{3+} ions with degeneracy.

Spinel oxide $LiMn_2O_4$ with mixed valence ions Mn^{3+}/Mn^{4+} in both octahedral and tetrahedral sites was observed to exhibit a Seebeck coefficient of -73 μV/K at high temperatures

(1100 K). This value is very close to the calculated result according to generalized Heikes formula $-k_B/e\ln(10/4) = -79\ \mu V/K$.[62] Hence we search layered Mn-based compounds.

The compound $BaMn_2Sb_2$ consists of edge-shared tetrahedral layers stacking along the c axis, separated by Ba layers, as depicted in Figure 1.10 (a). It is isostructural to $BaFe_2As_2$ which is the parent compound of Fe-based superconductors. Density functional calculations of the electronic structures suggest that the compound $BaMn_2Sb_2$ can exhibit very high Seebeck coefficient.[63] $BaMn_2Sb_2$ was also reported to have a relatively large Seebeck coefficient of ~ 225 μV/K at room temperature, though with poor electrical conductivity.[64, 65]

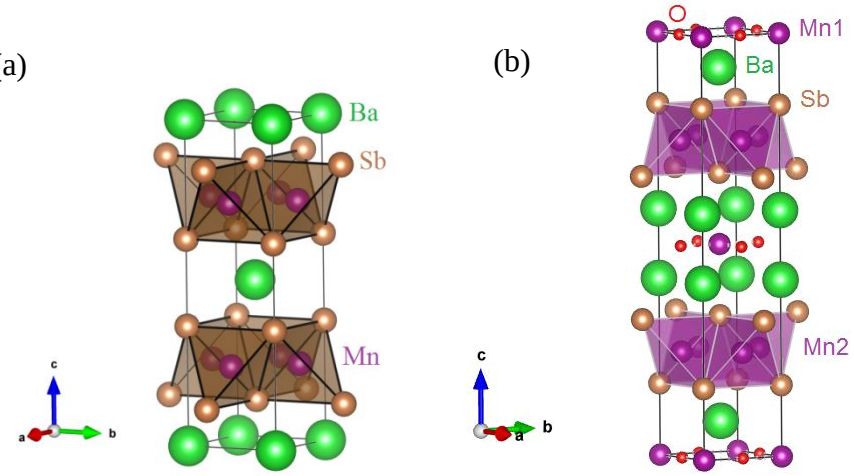

Figure 1-10 Schematic crystal structure of (a) $BaMn_2Sb_2$ and (b) $Ba_2Mn_3Sb_2O_2$.

Another layered compound $Ba_2Mn_3Sb_2O_2$ was reported to have alternating Mn-Sb layer and Mn-O layer.[66] The compound has a body-centered-tetragonal crystal structure. As shown in Figure 1-10(b), the Mn-O layer is similar to the CuO_2 layers in high temperature cuprate superconductors. And the Mn-Sb layer is similar to the FeAs layers in high temperature pnictides. No thermoelectric properties have been reported for this specific layered structure.

After describing the sample synthesis and characterization techniques, we will describe further the thermoelectric properties of these layered transition metal compounds. For understanding of the thermoelectric properties, magnetic properties are also investigated.

Chapter 2 Experimental Techniques and Analytical Procedures

Previous chapter has introduced several layered transition-metal compounds for thermoelectric property study. In order to study the intrinsic properties, high quality samples are needed. Depending on the nature of the compounds, different material synthesis techniques are employed. In this chapter, the experimental techniques including single crystal growth and characterization will be covered.

2.1 Synthesis of Compounds

For the pursuit of appropriate single crystals with desired crystal size and phase, it is necessary to study the temper of the crystals, like the stability in air, morphology, orientation, doping and impurities et al. Usually obtaining the right phase is the very first step to begin with.

2.1.1 Solid State Reaction

The reaction tends to form compounds with lower free energy compared to the reactants. But it has to overcome an energy barrier (denoted by activation energy E_A), by either increasing temperature or decreasing the energy barrier (e.g. catalysis). General process can be described in a few steps: diffusion of reactant to reactive interface, reaction on atomic scales, nucleation of product and growth and diffusion of products away from the reactive interface. Diffusion is often the reaction rate limiting step, which can be characterized by the material's chemical diffusivity D given by

$$D = D_0 e^{\left(-\frac{E_A}{RT}\right)} \qquad 2.1$$

where D_0 is the coefficient of diffusion and R is the gas constant. The typical values can be experimentally determined. For example, oxides have a rather low coefficient of diffusivity between 10^{-12} and 10^{-14} m^2/s. There are 3 typical ways to enhance the diffusivity, either by

increasing the reaction temperature, introducing defects by starting with reagents that decompose prior to or during reaction, such as carbonates, and well grinding so to increase the interface.

The general procedure for a conventional solid state synthesis is described as followings. First of all, we select appropriate starting materials. The effect of melting points, dopings and the reactive nature must be carefully considered. Second, we weigh out the starting materials so that stoichiometry products can be expected. Since diffuse length is very short (at the order of nm for oxides), the grinding and the mixing of the starting materials would be very important for the synthesis of a compound with a homogenous phase. They can be ground in a mortar and pestle or milled in ball mill. Smaller particle size and sufficient mixing help improve homogeneity. It is also a good idea to pelletize the powders to reduce the intimate distance among powder. Since the solid state reaction usually takes place at high temperatures, it is very important to choose a proper sample container to avoid the contamination of impurities. We choose alumina (Al_2O_3) crucibles or boats for reactions that don't need evacuated environment. Sealed quartz tubes are used for the reaction that is sensitive to air. During the heating process, atmosphere can significantly affect the quality of the product. For example, we can produce oxidizing conditions for oxides under air or O_2 flow. We can also provide reducing atmosphere using H_2/Ar, CO/CO_2.

To avoid impurity phases which are favored at low temperatures during cooling process, we can quench the products in the way that products are taken outside of the furnace immediately to be exposed to room temperature, water, or even liquid nitrogen. The rapid cooling process is experimentally proven to reduce or avoid unwanted low temperature phases.

In our work, we mainly use the solid state reaction as first step for our synthesis of single crystals by the floating-zone method that will be described later. After obtaining the products, we

can grind the products into powder and perform X-ray powder diffraction to check if we get the right phase. If impurity phases exist, we may have to repeat the sintering process. Solid state reaction process usually comes out with powder product or sometimes tiny crystals. Experimentally, there are other methods to synthesize desired single crystals.

2.1.2 Metathetical Reaction

In a metathetical reaction process, the precursors exchange ions to form the desired product and by-product. The by-product is usually easy to be separated by dissolving in water, or organic solvent like ethanol, acetone. Sometimes acid is necessary to separate the product.

The metathetical reaction method has significantly improved the synthesis of $PdCoO_2$ crystals. The mixture of $PdCl_2$ and CoO was placed in an alumina crucible and sealed in an evacuated quartz tube. The setup is shown in Figure 2-1(a).

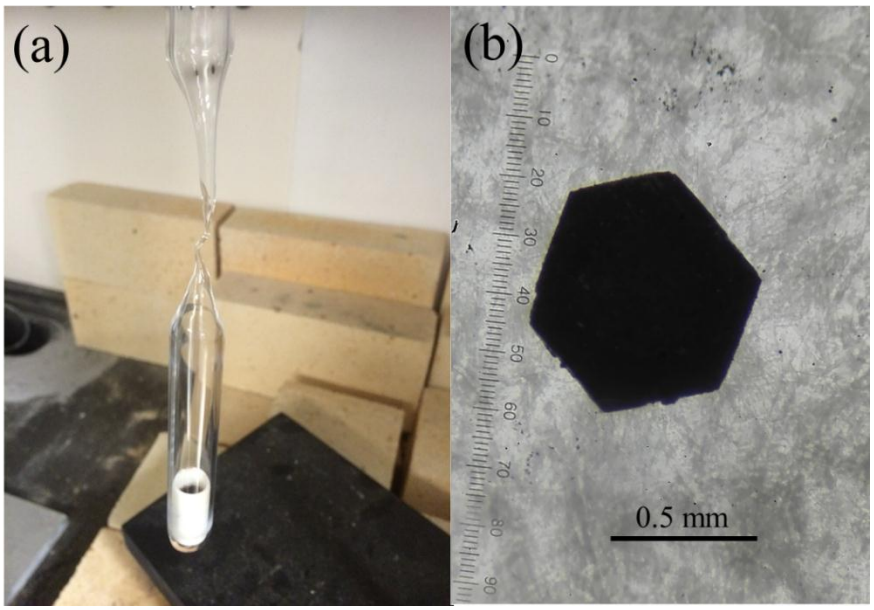

Figure 2-1 (a) The setup for a seal quartz tube with a crucible. The top is being pumping when the middle neck part is sealed. (b) A typical crystal of $PdCoO_2$ grown by the metathetical reaction.

It was then sintered at 700 ℃ for 40 hours. Plate-like crystals were found with typical hexagonal shape. The relatively large crystals are with length of about 0.6 mm and thickness of about 0.06 mm (shown in Figure 2-1(b)). The by-product turns out to be $CoCl_2$, which can be easily dissolved in ethanol. Crystals can be dried easily in air.

2.1.3 Combustion Synthesis

Using precursors that decompose during heating can enhance the diffusivity. Carbonate, metal sulfates and nitrate are the typical starting materials for combustion synthesis. During the reaction, they act as oxidants and decompose to release gas. Once the reaction is initiated, an exothermic reaction occurs and generates certain amount of heat. Hence the reaction becomes self-sustaining. This auto-propagated process can be used directly in the production of high purity, homogeneous oxide powder. Generally, we are looking for combustion synthesis that does not produce toxic gases, or react explosively. In our work, the combustion synthesis with carbonates has produced $Bi_2Sr_2Co_2O_y$ and $Sr_3(Ru_{1-x}Mn_x)_2O_7$ polycrystallines with very high purity.

For the synthesis of polycrystalline $Bi_2Sr_2Co_2O_y$, the starting materials include Bi_2O_3, $SrCO_3$ and Co_3O_4 in stoichiometry ratio. The reaction process can be described as

$$Bi_2O_3 + 2SrCO_3 + \frac{2}{3}Co_3O_4 \rightarrow Bi_2Sr_2Co_2O_y + 2CO_2 \qquad 2.2$$

The mixture of starting materials was sintered at 900 ℃ for 24 hours in air. The product was then ground into powders for future synthesis of single crystals.

For the synthesis of $Sr_3(Ru_{1-x}Mn_x)_2O_7$, a big concern is the heavy evaporation of Ru during the sintering. In order to keep the stoichiometry, we add extra amount of Ru.

$$4SrCO_3 + 3((1-x)Ru + xMnO_2) \rightarrow 4/3Sr_3(Ru_{1-y}Mn_y)_2O_7 + Ru \uparrow \quad 2.3$$

The mixture of starting materials was sintered at 1350 ℃ for 40 hours with O_2 gas flow. In order to avoid the undesired phases Sr_2RuO_4, $Sr_4Ru_3O_{10}$ or $SrRuO_3$ et al., the product was quenched from furnace temperature to room temperature to frozen the desired phase $Sr_3Ru_2O_7$. The product was then ground into powder for future synthesis of single crystals.

Both of the synthesis processes only involve carbonate for combustion synthesis which releases CO_2 during the sintering process and produces high purity polycrystalline at the end.

2.1.4 Flux Method

The principle of the flux method is that the reactants are dissolved in solvents with high diffusivity at high temperatures. Usually they are maintained slightly above the saturation temperature to form complete solution. Then crystals would precipitate under the slow cooling process. The choice of solvent is of great importance. A suitable solvent usually has relatively lower melting point and does not form stable compounds with the reactants. It is better to have a large difference between boiling and melting temperature so that they can maintain working as a stable solvent. The solvent must also be easily separated from the products. They are usually separated by spinning in a centrifuge immediately after taken out from the hot furnace. They can also be removed by chemical etchers. Sometimes we can use part of the reactants itself as solvent. Crystals grown by this method usually exhibit their natural facets.

In our work, we use tin (Sn) as solvent to synthesize $BaMn_2Sb_2$ single crystals. Since Ba metal is very sensitive to oxygen, weighing starting materials was conducted in a N_2-filled glove box. The molar ratio of Ba:Mn:Sb:Sn is equal to 1:2:2:5. Then the mixture was placed in an alumina crucible and immediately sealed in an evacuated quartz tube. Firstly it was sintered at

1150 ℃ for 24 hours. Then it was cooled down slowly at a rate of 5℃ per hour until 700 ℃. After sintering for 24 hours to improve crystal quality, the sample was quenched and spun in a centrifuge to separate the solvent from the products. We can obtain typical plate-like crystals with size of ~1 cm, as shown in Figure 2-2.

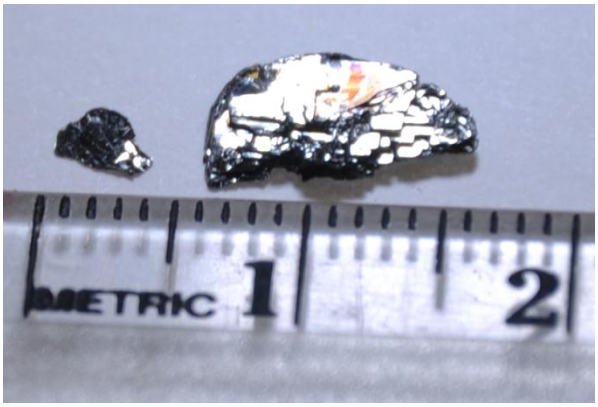

Figure 2-2 $BaMn_2Sb_2$ crystals grown by the Sn flux method. Natural layered structure can be observed.

2.1.5 Floating-zone Method

In order to measure Seebeck coefficient and thermal conductivity, we need to grow large single crystals (at least a few mm long). There are several growth methods that have been widely used, including the Bridgeman method, the Czochralski method and the floating zone method. In our lab, we focus on growing single crystals by floating zone method. A melting zone connecting a feed rod and seed rod is maintained by the light of halogen lamps reflected by two elliptical mirrors. The rods move downward, the melting zone travels along the feed rod. Crystals form progressively on the top of the seed rod. This is a crucible-free approach, thus containing no impurities from the crucible. In addition, this method usually produces relatively large crystals.

The feed rod is made of prepared polycrystalline under hydrostatic pressure. Fill a rubber tube with desired diameter (usually ~5 – 8 mm) with the prepared polycrystalline powder. Then

we make it straight and uniform with the same diameter along the length. After that it will be pressed under hydrostatic pressure for a few minutes. Finally we can have a rod with length ~ 10 – 15 cm. The next step is to sinter the rod at moderate temperatures to make the rod solid enough to hang on the hook in the imaging furnace. The seed can be single crystal or polycrystalline. We use an imaging furnace (Canon Machinery, model: SC1MDH-20020). Figure 2-3 shows the setup of the imaging furnace. The feed rod is hung over the top shaft while the seed rod sits on the bottom shaft. They need to be perfectly aligned. Both shafts can move and rotate at the same time at a preset speed.

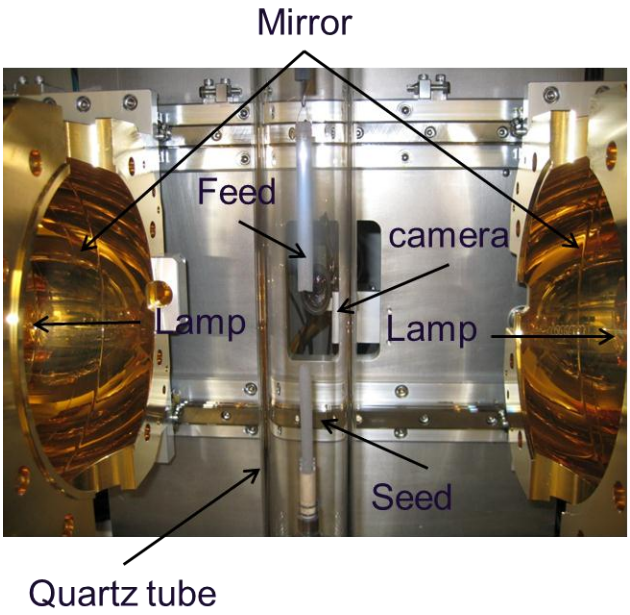

Figure 2-3 Picture of the imaging furnace for floating zone method to grow single crystals. Two halogen lamps are mounted (not shown) at the two focal points of the elliptical mirror that are coated with Au layer for maximum reflection of the lights emitting from the lamps. The heating area will be around 5 mm × 5 mm that forming a floating melting zone between the upper feed rod and the lower seed rod. A camera monitors the growth condition.

A big quartz tube is mounted so to be (1) able to observe and (2) controlling growth environment. Since the furnace system is sealed, desired atmosphere can be applied (the

maximum pressure is no more than 10 atm). Heating is by lights from the halogen lamps that are reflected by the elliptical mirror with Au coating and focused on a small spot (typically 5 mm × 5 mm). The bottom end of the feed rod is molten and connected to the seed. During the growth, the feed and seed are rotated oppositely to help the melting zone keep uniform. Maintaining a stable melting zone is the key to grow high quality crystals. There are a few factors that could affect the melting zone, including the competition of surface tension and gravitation, volume change (feed and seed speed), atmosphere and pressure and power control during the growth. We usually monitor the melting zone and adjust the lamp power and moving speeds of the shafts to stabilize the zone.

For the synthesis of $Bi_2Sr_2Co_2O_9$ single crystals, a ~10 cm long feed rod and a ~3 cm long seed rod were used with the rotation of 20 rpm. The growth speed (seed speed) was about ~1.5m/h and the growth was in air. Figure 2-4(a) shows the rod of the growth. After further polishing, the crystals are found to be easily cleaved perpendicular to the growth direction.

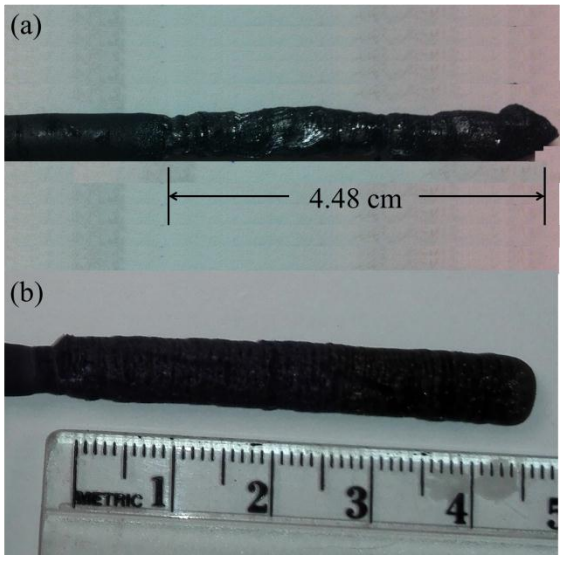

Figure 2-4 Grown crystal of (a) $Bi_2Sr_2Co_2O_{9-\delta}$ and (b) $Sr_3(Ru_{1-x}Mn_x)_2O_7$, the crystal will be polished and cleaved.

For the synthesis of $Sr_3(Ru_{1-x}Mn_x)_2O_7$ single crystal, the feed rod was above 10 cm long. The rotation speed was 25 rpm. The growth speed is set to be relatively fast because of the heavy evaporation of Ru metal. It was set to be 15 mm/h. Depending on the growth conditions, the feed speed ranged from 25 to 30 mm/h. During the growth, a pressure of 10 atm was applied by the mixture of Ar and O_2 gas with 1:1 ratio. The final crystals, as shown in Figure 2-4 (b), were pretty easy to cleave but they were surrounded by a layer of impurities grown simultaneously. We polished the crystals by sand paper before performing any characterization.

2.2 Structural Characterization

The structure characterizations are of great importance. For our work, we rely heavily on X-ray powder diffraction for the phase determination. We also utilize single crystal X-ray diffraction and refinement to figure out the symmetry and the lattice constants. We take advantage of transmission electron microscopy (TEM) to characterize films at atomic resolution. For the purpose of determining doping levels, we use wavelength diffraction spectroscopy (WDS) to figure out the proportions of elements in the system.

2.2.1 X-Ray Powder Diffraction

X-ray diffraction (XRD) has been widely used in exploring the crystalline structure. X-ray used in diffraction experiments usually has wavelength of 0.5 – 1.8 Å, which is comparable to the distance between atoms in a crystal. A conventional generator produces X-ray by striking an energetic beam of particles (e.g. electrons) or radiation at a target material. The wavelength of generated X-ray depends on the electronic structure and atomic number of the target material, as described below.

$$\frac{1}{\lambda} = K(Z - \sigma)^2 \qquad 2.4$$

where λ is the wavelength of the X-ray, K is a proportionality constant, Z is the atomic number of the target atoms, and σ is shielding constant. To generate suitable X-ray for crystallographic studies, metal targets are typically used, such as Mo, Cu. Electrons coming from a heating metal filament are accelerated by a large electrical field and bombarded at the target. A core electrons (e.g. from K-shells) from an atom of the target is excited and kicked out, followed by an electron in a higher energy level (e.g. from the L or M levels) dropping down to fill the core hole. This process emits X-ray radiations with energies that are equal to the energy difference between the upper and lower energy levels. For example, the Kα radiation of Cu has a wavelength of 1.54178 Å.

When X-ray hits a material, it can be scattered by atoms, producing spherical waves. When the material has ordered arrays of atoms, the elastic scattering produces a regular array of periodic spherical waves. The incident X-ray radiations would produce a peak if their reflections interfere constructively. This phenomenon has been well described by Bragg's law.

$$n\lambda = 2dsin\theta \tag{2.5}$$

where n is an integer number (1, 2, 3…), λ is the wavelength of the incident X-ray, d is the distance between scattering crystal planes, and θ is the incident angle of the incident X-ray. There are multiple planes that can reflect X-ray constructively at certain angle θ. These planes are indexed by Miller indices (hkl) and they can be represented as orthogonal to the reciprocal lattice vector, $h\overrightarrow{b_1} + k\overrightarrow{b_2} + l\overrightarrow{b_3}$, where $\overrightarrow{b_1}, \overrightarrow{b_2}, \overrightarrow{b_3}$ are reciprocal lattice vectors. The spacing d can be calculated from the Miller Indices. For any Bragg lattice,

$$\frac{1}{d^2} = \frac{1}{V^2}(C_{11}h^2 + C_{22}k^2 + C_{33}l^2 + 2C_{12}hk + 2C_{23}kl + 2C_{23}kl + C_{31}lh) \tag{2.6}$$

The constants C_{ij} are given by

$$C_{11} = b^2c^2sin^2\alpha$$

$$C_{22} = c^2a^2sin^2\beta$$

$$C_{33} = a^2b^2sin^2\gamma$$

$$C_{12} = abc^2(cos\alpha cos\beta - cos\gamma)$$

$$C_{23} = a^2bc(cos\beta cos\gamma - cos\alpha)$$

$$C_{31} = ab^2c(cos\gamma cos\alpha - cos\beta) \quad 2.7$$

where a, b, c, α,β,γ are the lattice constants. V refers to the volume of a unit cell, which can be represented by

$$V = abc\sqrt{1 - cos^2\alpha - cos^2\beta - cos^2\gamma + 2cos\alpha cos\beta cos\gamma} \quad 2.8$$

For example, a simple cubic crystal has a=b=c and α=β=γ=90°. Then the spacings between crystal planes (hkl) can be calculated as

$$\frac{1}{d^2} = \frac{(h^2+k^2+l^2)}{a^2} \quad 2.9$$

For a hexagonal lattice, the lattice parameters satisfy a=b, α=β=90°, γ=120°. We can find out the d spacings by

$$\frac{1}{d^2} = \frac{4}{3}\left(\frac{h^2+hk+k^2}{a^2}\right) + \frac{l^2}{c^2} \quad 2.10$$

According to Bragg's law, when scanning the incident angle θ in a range, the diffracted X-ray exhibit peaks at constructive interference positions. The d spacing can simply be found in XRD

pattern by figuring out the constructive position θ. On the other hand, the intensity of a diffracted peak contains additional information. The intensity can be described by the following expression:

$$I(hkl) = |S(hkl)|^2 M_{hkl} LP(\theta) TF(\theta) A(\theta) \quad 2.11$$

where S(hkl) refers to structure factor, M_{hkl} denotes the multiplicity, LP(θ), TF(θ) and A(θ) are the Lorentz & Polarization Factor, temperature factor, and absorption correction, respectively. The structure factor reflects the interference of atoms in a unit cell upon incident radiation. It contains the information of the locations of atoms and the atomic form factor f, as shown below.

$$S(hkl) = \sum_i f_i \exp\{-2\pi i(hx_i + ky_i + iz_i\} \quad 2.12$$

where f_i refers to the atomic form factor of the i^{th} atom, x_i, y_i, z_i are the coordinates of the i^{th} atom.

In our work, we use the Panalytical Empyrean X-ray Diffractometer (as shown in Figure 2-5), equipped with PreFIX (prealigned, fast interchangeable X-ray) modules to produce Cu Kα radiation. The working power is at 45kV and 40 mA. The diffractometer also equips a number of optics to improve the measurement. Monochromators are used to narrow the X-ray wavelength distribution. An incident beam monochromator can select only Kα1 radiation (λ = 1.54056 Å) from the tube while a diffracted beam monochromator is used to reduce the fluorescent radiation from the sample before reaching the detector. A 0.04 rad soller slit is used to produce a line-shaped incident beam and to reduce peak asymmetry. A fixed divergence slit is used to limit the vertical divergence and a collimator is used to limit the horizontal divergence. A beam mask (5 mm or 10 mm) is also equipped to limit the beam width. Samples are put in an amorphous Si holder that is installed onto the stage. For power diffraction measurement, the holder is spinning during the measurement. A typical measurement scans 2θ from 5 ° to 90 ° with a step size of 0.026˚. The obtained pattern is compared to standard cards from International Center for

Diffraction Data (ICDD) database by “search & match” function in Highscore. The comparison is mainly based on the peak positions and the relative peak intensities.

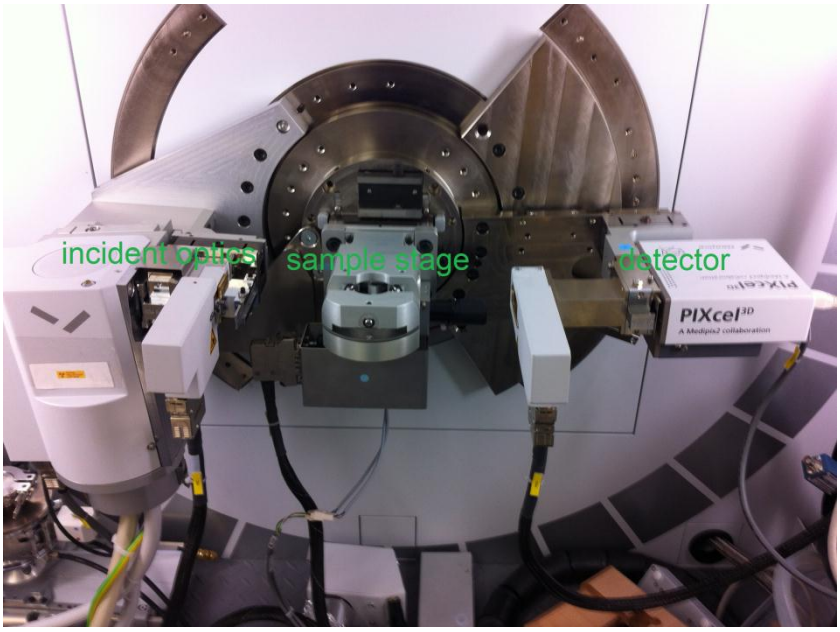

Figure 2-5 Picture of the Panalytical Empyrean X-ray Diffractometer with the sample stage for powders installed.

2.2.2 Single Crystal X-ray Diffraction

The powder X-ray diffraction is mainly used for phase identifications. In order to reveal information about the full unit cell, including lattice constants, atom positions, single crystal X-ray diffraction is a more suitable technique. The incident X-ray hits the crystal and is scattered by the electrons of each atom. The interference of scattered X-ray forms thousands of diffraction spots to the specific directions on a screen. They follow Bragg’s law and the intensity depends on the structure factor. The measured intensities of diffraction pattern can be used to determine the structure factor.

$$I(K) = |S(K)|^2 \qquad 2.13$$

where I(K) is the intensity of peaks and S(K) is the structure factor. However, only the amplitude of S(K) is determined, causing a known phase problem. There are a few ways to determine the phases. One is direct method that estimates phases statistically from the amplitudes of the normalized structure factor. This method is very important in solving the phase problem in chemical crystallography. Another way is to use methods based on the Patterson function which are applied when some heavy atoms are present.

Electron density distributions in crystals can be determined by the positions and intensities of the dots in diffraction pattern upon calculations. The electron density function can be calculated at every point in a single unit cell

$$\rho(x,y,z) = \frac{1}{V}\sum_h \sum_k \sum_l |S(hkl)|\cos\{2\pi(hx_i + ky_i + lz_i) - \phi(hkl)\} \qquad 2.14$$

The structure factor is in reciprocal space and the electron density is in real space. The electron density can be obtained by calculations, giving an electron density map from which the atomic positions can be figured out at the maxima of electron density. The next step is to build a structure model based on all information obtained. The initial structure model is then refined to optimize the fitting of structural parameters between the observed and calculated intensities in the diffraction pattern. Essentially, the structural model must be chemically appropriate and has the estimated standard deviations (R value) as small as possible. Moreover, the number of peaks left in the electron density map should be as small as possible. After the refinement is done, a standard file (CIF: crystal information file) is created to include all the information of the structure, such as atomic coordinates, symmetry so that we can draw the crystal structure.

The single crystal X-ray diffraction was performed on a Nonius KappaCCD diffractometer. The radiation source is a fine-focus sealed tube with graphite monochromator.

The samples are usually of 0.3 – 0.5 mm. The refinement is based on the structure-invariant direct methods.

2.3 Single Crystal Neutron Scattering

Similar to single crystal X-ray diffraction, single crystal neutron scattering provides information about crystal structure as well. The diffraction result can be transformed to the charge and nuclear density mapping. By crystal symmetry analysis, the crystal structure can be refined about lattice parameters and atomic positions. The difference is that neutron itself has ½ spin and can also respond to magnetic moments of ions in the crystal. Neutrons can be reflected by the magnetic moments perpendicular to the incident directions. The final diffraction results also include magnetic Bragg's peaks.

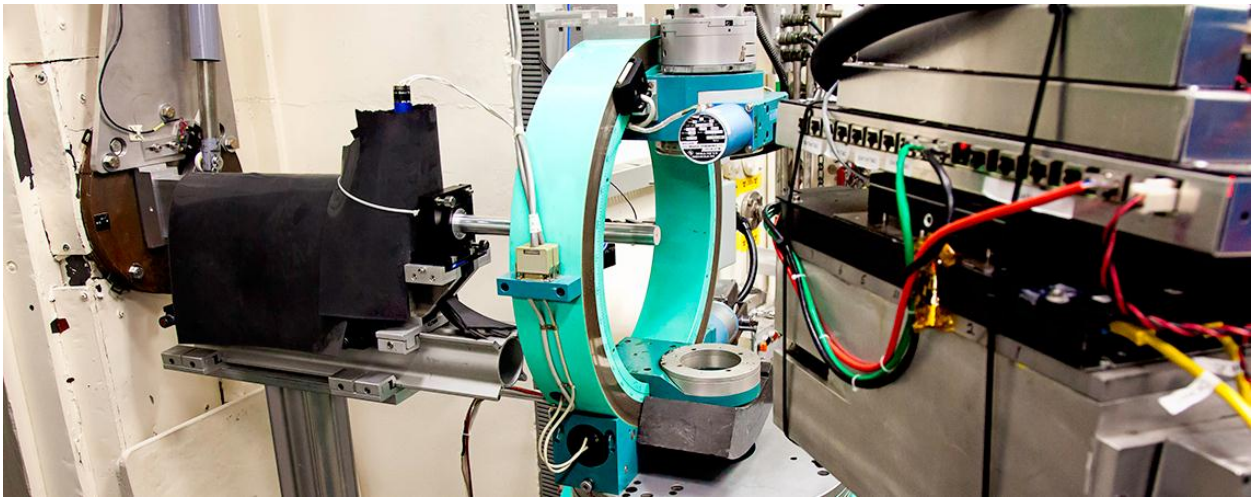

Figure 2-6 Four-Circle diffractometer for HB-3A at Oak Ridge National Lab. Picture adapted from website: https://neutrons.ornl.gov/hb3a.

The neutron scattering measurement was performed in HB-3A at Oak Ridge National Lab (ORNL) with the Four-Circle Diffractometer goniometer, as shown in Figure 2-6. Thermal neutrons are reflected by a multilayer-{110}-wafer silicon monochromator with fixed reflection angle of 48°. Three choices of wavelength are available, 1.003, 1.542, and 2.541 Å. The

scattering angle ranges from 5° to 155° with ^{3}He detector. A closed-cycle helium refrigerator can maintain the sample space from 4.5 to 450 K. An extra furnace can also be installed so that the sample chamber can reach as high as 800 K.

Comprehensive collections of reflections includes both nuclear and magnetic ones. The nuclear structure will be refined by the package FULLPROF (mainly developed for Rietveld analysis of diffraction data). Based on the crystal symmetry and the magnetic propagation vector, the basis vectors for magnetic structure can be generated by SARAH (used for calculations of representational analysis magnetic structure based on nuclear structure). With the same profile parameters, the magnetic structure can be refined, as well as the magnetic moment of ions.

2.4 Electrical and Thermal Transport

After the synthesis and phase identification of samples, we measure physical properties and study the mechanism. For thermoelectric materials, Seebeck coefficient S, electrical resistivity ρ and thermal conductivity κ need to be measured carefully and will give the value of figure of merit ZT to evaluate the potential of the compounds as thermoelectric materials. Further analysis on the results of both electrical and thermal transport measurements will help figure out the intrinsic transport mechanism of compounds.

To obtain accurate results, the electrical resistivity measurements of samples were performed on relatively small samples (typical size: thickness<1mm, width ~1 mm, length ~ 2 mm). The reason is that the quality of single crystal tends to be worse at larger scale, especially for layered compounds that might have stacking faults. To eliminate the effect of contact resistance between contacting leads and sample surface, we use the standard four-probe technique, as shown in Figure 2-7. The probe wires are Pt wires of diameter 50 μm. They are

attached on the surface by Epoxy H20E. Electrical current flows from A to B and the voltage drop between C and D is monitored. The resistance can be obtained based on Ohm's law.

$$R = \frac{V_{CD}}{I_{AB}} \tag{2.15}$$

If the dimensions are determined, the electrical resistivity can be calculated by

$$\rho = \frac{A}{L}R = \frac{AV_{CD}}{LI_{AB}} \tag{2.16}$$

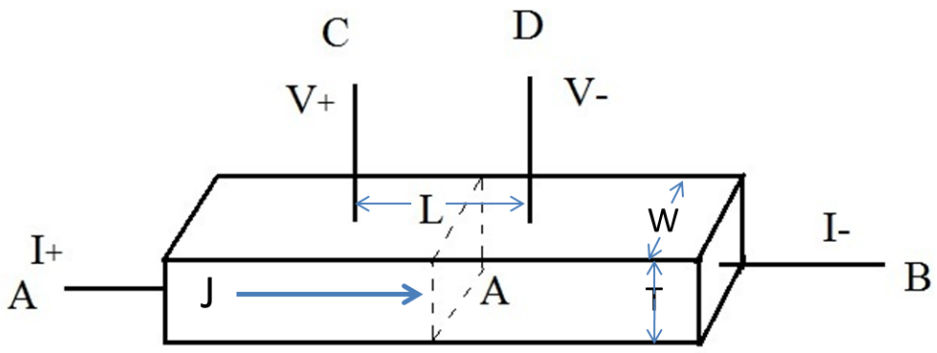

Figure 2-7 Schematic demonstration of the four-probe method for electrical resistivity measurements. L, W, and T denote the length between voltage probes, width and thickness of a sample, respectively. A=W*T is the cross section area.

The resistivity measurements are performed in Physical Property Measurement System (PPMS) made by Quantum Design. For DC resistivity measurement, PPMS can apply a minimum current of 0.01μA and a maximum current of 5 mA while the voltage ranges from 1 – 95 mV. The applied power must be kept small during the measurements, especially for small samples. Even small amount of heat can increase temperature significantly. This might cause

temperature stabilization issue for low temperature measurements. However, for low resistance measurements, the voltage signal may be quite small and coupled with signal noises. These noises could be internal, such as Johnson noise which results from the charge movement by thermal energy. External noise may come from the interferences by electrical equipment. The common method to reduce noise is to use a lock-in amplifier by applying a small AC current. The signal of voltage drop is of sine behavior. Only the signal that has the same frequency as the AC current is picked and noise (white noise, or noise with different frequencies) can be filtered. For low resistance measurement, by carefully selecting the current amplitude, frequency and duration, we can have accurate result with little noise (<-50dB).

Seebeck coefficient S and thermal conductivity κ measurements of samples are also performed by PPMS. Figure 2-8 (a) shows the setup for measurement. By applying a heat pulse at one end of a sample, a temperature gradient across the sample is created. The measurements of the temperature and voltage difference between two regions, the Seebeck coefficient and thermal conductivity can be obtained simultaneously. They are performed by a thermal transport option puck, as shown in Figure 2-8(b). A reference sample Ni metal is installed in the sample puck by four-probe method. A heat pulse is generated by a resister chip in the heater shoe which also solders an electrical current lead. The heat pulse conducts along the sample. A Cernox 1050 thermometer with a voltage lead soldered inside monitors both the temperature and voltage variations during the measurement. Each of the thermometer shoes and heater shoe has a small hole where a copper lead is inserted and held by a stainless steel metric M1 screw. The shoes are connected to the sample puck by 2-inch-long, 0.003-inch-diameter wires. In order to minimize the thermal conduction between the sample and puck, all wires are made of manganin alloy except the current/voltage lead that is made of PD-135 low resistance copper alloy. The cold end

of the sample is connected to the cold foot which contains a Phillips screw and a stainless steel clamp. In order to minimize the radiation between the sample and the environment, a copper isothermal radiation shield covers the whole assembly. When the whole assembly is ready, it is then plugged into the PPMS. A charcoal is used for obtaining high vacuum below 10^{-6} Torr to reduce the contribution of gas to the thermal transport.

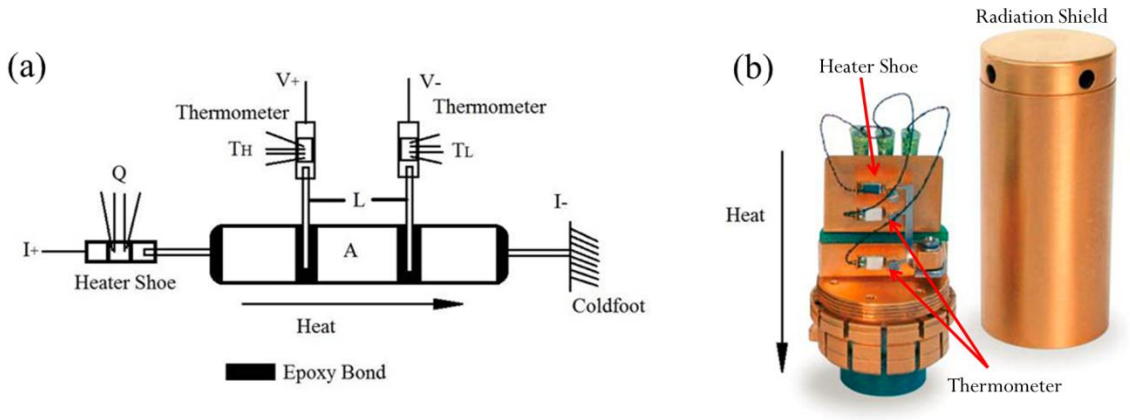

Figure 2-8 (a) Schematic demonstration of thermal transport measurement of a sample. A heat pulse Q created by a heater shoe conducts along the sample. The temperatures and voltages at hot region (T_H, V_+) and cold region (T_L, V_-) are measured. (b) A standard sample puck for thermal transport measurement, provided by Quantum Design. A standard nickel sample is installed.

The principle of the measurements is based on a named two-tau model. The temperature and voltage versus time during one simple measurement is shown in Figure 2-9. The heater is turned on first. Temperature at the hot region of the sample begins to warm, and so does the cool region by heat flow in the sample. When the heater is turned off, both temperatures in the hot region and cold region begin to decrease. At the same time, the induced temperature difference increases during the power on stage and then decreases. The temperature difference finally vanish at long time.

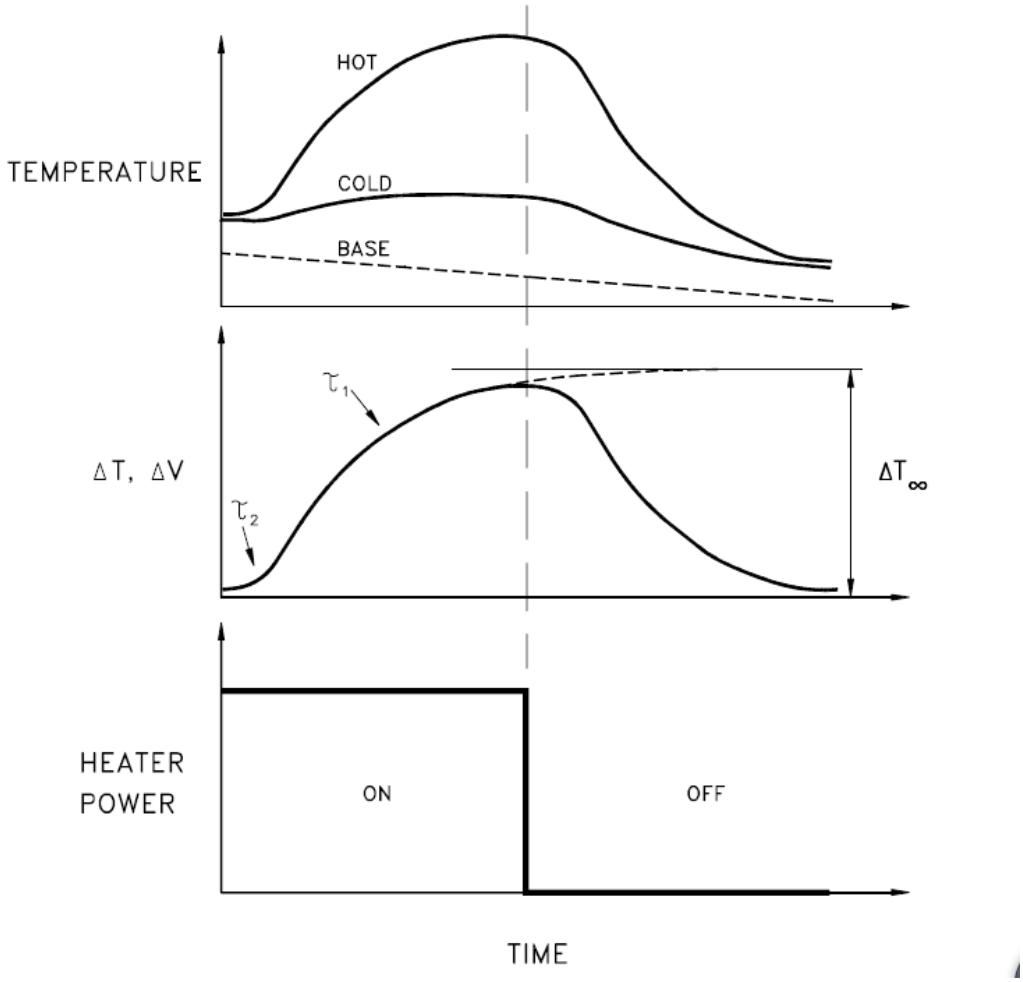

Figure 2-9 Responses of temperature and voltage at hot and cold region in an idealized sample when the heater is turned on and off. The top panel shows the response of hot and cold thermometers during an idealized heat pulse; the middle panel shows the temperature and voltage difference between hot and cold region. The bottom panel shows a square-wave heat pulse.

This data over the duration of the heat pulse is then fitted by two-tau model (provided by PPMS manual from Quantum Design)[17]

$$\Delta T_{model} = \Delta T_{\infty} \times \{1 - \{\tau_1 \times \exp\left(-\frac{t}{\tau_1}\right) - \tau_2 \times \exp\left(-\frac{t}{\tau_2}\right)\}/(\tau_1 - \tau_2) \qquad 2.17$$

where ΔT_∞ denotes the asymptotic temperature drop across the sample if keeping the heater on, and τ_1 and τ_2 represent long and short empirical time constants, respectively. The long time constant τ_1 associates with the thermal diffusion of the sample while the short time constant relates to the contact leads. The thermal conductivity κ can be calculated by

$$\kappa = \frac{QL}{\Delta T_{model} A} \tag{2.18}$$

where Q is heat generated by the heater controlled by input electric current, L is the distance between thermometers and A is the cross section area, respectively.

The Seebeck voltage is fitted similarly. After the ΔT data is fitted to obtain τ_1 and τ_2, the voltage signal between the two thermometers are fitted by a linear least-squares routine.

$$\Delta V_{model} = \Delta V_\infty \times \left\{1 - \frac{\left[\tau_1 \times \exp\left(-\frac{t}{\tau_1}\right) \pm \tau_2' \times \exp\left(-\frac{t}{\tau_2'}\right)\right]}{\tau_1 - \tau_2'}\right\} + bt + c \tag{2.19}$$

where ΔV_∞ is the asymptotic Seebeck voltage drop akin to ΔT_∞, b and c are parameters that describe linear drift and offset voltages, respectively. τ_2' is related to the Seebeck coefficient of the leads. Hence, a well-defined Seebeck coefficient can be measured by

$$S = \frac{\Delta V_{model}}{\Delta T_{model}} \tag{2.20}$$

For the sake of accurate measurement, a delicate system is designed to measure the thermoelectric properties of samples. The samples are usually cut into a bar shape. For different materials, specific dimension requirements are met to improve the measurement. For example, for materials with κ in the range of 2-50 W/m-K, a dimension 8 × (2 × 2) mm^3 is recommended. By contrast, materials with higher κ of 10 – 250 W/m-K are usually cut into a thinner shape of 10

$\times(1 \times 1)$ mm^3 to help maintain a temperature gradient along the sample. Similarly, a sample of $2.5 \times(5 \times 5)$ mm^3 is suitable for the measurement of a material with lower κ of 0.1 – 2.5 W/m-K. Four copper leads are connected to the sample by epoxy. The PPMS can perform thermal transport measurement in the range of 1.9 – 400 K. The typical temperature scanning rate is ±0.5 K/min for T>20 K and ±0.2 K/min for T<20K. A magnetic field of 0 – 14 T may also be applied if necessary. The system error for Seebeck coefficient is ±5% or ±0.5 μV/K (From manual provided by Quantum Design), whichever is greater.

In practice, all the heater and thermometer shoes need to be carefully calibrated before the measurement. Figure 2-10 shows a typical temperature dependence of a heater and thermometer. The resistance of a heater changes very slowly over temperature while that of a thermometer is very sensitive to temperature variations.

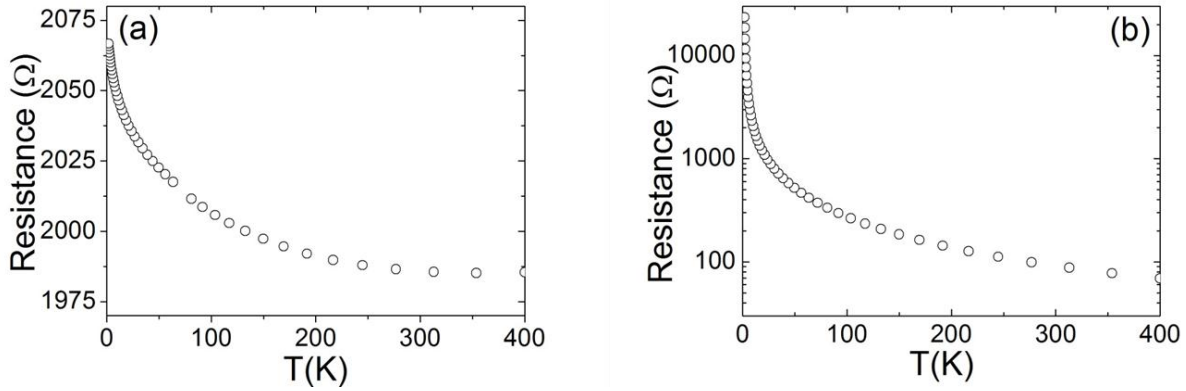

Figure 2-10 The temperature dependence of a heater (a) and a thermometer (b) determined by the calibration process.

A nickel standard sample (grade 201) is used as reference sample. The cross-sectional area is 0.32 mm^2 and the length is 8.3 mm. A typical measurement of Seebeck coefficient S and thermal conductivity κ is shown in Figure 2-11. The tail above room temperature results from the

thermal radiation from the sample and the shoe assemblies. Nickel itself has a negative value of Seebeck coefficient and the magnitude increases almost linearly over temperature.

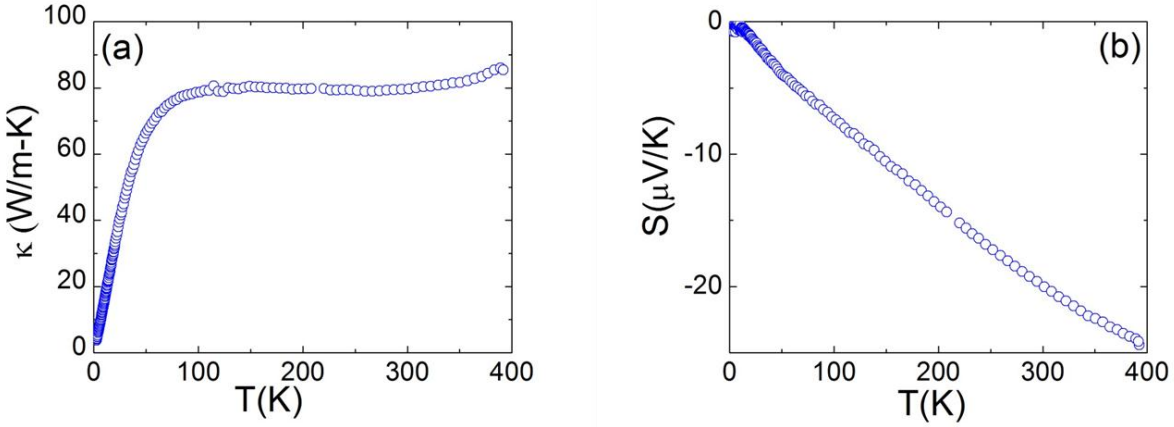

Figure 2-11 Thermal conductivity (a) and Seebeck coefficient (b) measurement of a Nickel standard sample is shown, respectively.

During the measurement, we can observe the fitting curve in a Waveform tab, as shown in Figure 2-12. A good fitting curve implies that the data point taken is reasonable.

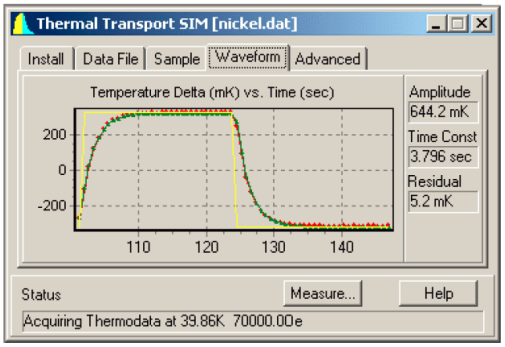

Figure 2-12 An example of fitting process during thermal transport measurement (provided by Quantum Design). The yellow line represents a heat pulse. The time traces of ΔT, along with the fitted curve are displayed.

In practice, a parameter ratio (period over τ_1) also values the quality of a data point. Typically, we need to adjust power and period to let the period ratio above 8 all the time. PPMS is able to measure electrical resistivity at the same time. But we measured separately by

considering the heat generated by electrical current as well as the heat-carrying of an electrical current described by Thomson effect.

2.5 Hall Effect Measurement.

Hall Effect measurement is performed to characterize materials. A number of quantities can be obtained, such as carrier mobility, carrier concentration, carrier type from Hall coefficient (R_H). The principle underlying the Hall Effect is the Lorentz force on moving carriers under magnetic field. As shown in Figure 2-13 (a), when electric current flows under a magnetic field, Lorentz force on the moving charges results in accumulation of charges at one side of the sample. Then a transverse electric field is established which apply opposite force on the charges. At equilibrium, the Lorentz force equals the force by transverse electric field. By measuring the transverse voltage, named Hall voltage, a relationship with the applied current can derive those quantities mentioned above.

From Drude theory, the flow of current in response to electric field can be described by

$$J = \frac{\tau q^2 n}{m} E \equiv \sigma E \qquad 2.21$$

where σ is the conductivity, n is the concentration of carriers, q is the charge, m is the mass of the carrier and τ is the mean free time between collisions. Applying a magnetic field, the equation can be rewritten as

$$J = \sigma E + \frac{\tau q}{m}(J \times B) \qquad 2.22$$

With $\boldsymbol{J}$=J$\boldsymbol{x}$ and $\boldsymbol{B}$=B$\boldsymbol{z}$, the equation can be resolved into two components

$$\sigma E_x = J \qquad 2.23$$

$$\sigma E_y = \frac{\tau q}{m} JB \tag{2.24}$$

The Hall coefficient R_H is defined as

$$E_y = R_H JB \tag{2.25}$$

In the Drude model, the Hall coefficient can be described as

$$R_H = \frac{1}{nq} \tag{2.26}$$

The sign of R_H indicates the type of the charge carriers and the magnitude is inversely proportional to the charge concentration. The Hall Effect is measured by the transverse voltage difference along y axis.

$$\Delta V_H = \frac{R_H}{t} IB \tag{2.27}$$

where t is the thickness of the sample, I is the electrical current.

When measuring the transverse potential difference, the voltage probes may not be precisely aligned, leading to the error caused by the longitudinal contribution of voltage difference (as shown in Figure 2-13(b)).

$$\Delta V_{ab} = \frac{R_H}{t} BI + RI \tag{2.28}$$

There are two methods to eliminate the offset voltage. Scan the magnetic field with fixed current I. Then the slope of the linear relationship between ΔV_{ab} and B is $R_H I/t$. The other method is to apply fields with opposite directions. Then

$$\Delta V_{ab}(+B) - \Delta V_{ab}(-B) = 2\frac{R_H}{t} BI \tag{2.29}$$

Hence the possible errors induced by longitudinal deviation of the two leads can be minimized.

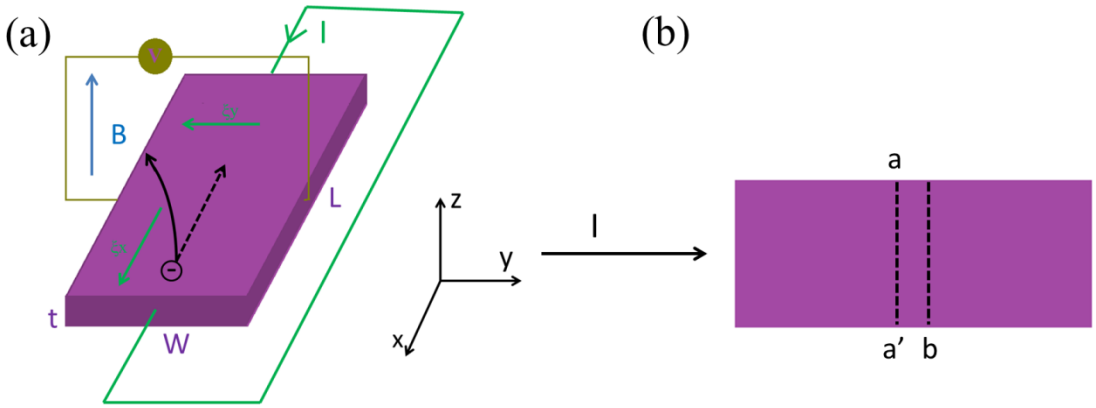

Figure 2-13 (a) Schematic picture showing the setup for measuring Hall Effect. (b) Demonstration of the horizontal offset of Hall voltage measurement.

2.6 Magnetic Properties Measurement.

Magnetic susceptibility characterizes the response of a material subject to external field. It is defined as

$$\chi = M/H \tag{2.30}$$

where M is the magnetization of a material and H is an external field. The magnetization is the density of magnetic moments in the materials. Depending on the magnetic ordering and temperature dependence of the magnetic susceptibility, there are a couple of classifications: diamagnetic, paramagnetic, ferromagnetic, antiferromagnetic and ferrimagnetic. The magnetic susceptibility of the materials except the diamagnetic materials obey the Curie-Weiss law,

$$\chi = \frac{C}{T - T_C} \tag{2.31}$$

$$C = \frac{\mu^2 N_A \mu_0}{3k} \tag{2.32}$$

where N_A is Avogodro's number, k is Boltzman's constant, μ_0 is the permeability of free space, and μ is the effective magnetic moment of ion. For $T_C = 0$ K, it is paramagnetic. For a positive T_C, it is ferromagnetic. For a negative T_C, it is antiferromagnetic. Usually the temperature and field dependence of magnetic susceptibility can reveal the intrinsic magnetic ordering of the materials.

There are a variety of methods to measure the magnetic susceptibility, such as the Guoy method, the Faraday method, and nuclear magnetic resonance (NMR). In our work, we used the Superconducting Quantum Interference Device (SQUID) which is based on Josephson junctions. It has two Josephson junctions in parallel. A Josephson junction is made of two superconducting layers separated by an insulating layer. The insulating layer is thin enough that electrons can tunnel through the barrier. This effect can be described by

$$I_J = I_0 sin\delta \tag{2.33}$$

$$V = \frac{\Phi_0}{2\pi}\frac{d\delta}{dt} \tag{2.34}$$

where I_J is the current flowing through the junction, I_0 is the critical current of the junction, δ is the superconducting phase difference, Φ_0=h/2e is the superconducting flux quantum, V is the voltage across the junction. The critical current can be changed by temperature and magnetic flux. Here voltage is always zero for a DC current below the critical current. A DC SQUID setup is shown as Figure 2-14. Current I is split into two branches. If applying a small magnetic field, a screening current I_s would be induced to circulate the loop to let the total magnetic flux be integers of magnetic flux quantum. In each branch, the current is either $I/2+I_s$ or $I/2-I_s$. A voltage appears as soon as the current exceeds the critical current I_0. For external flux $n\Phi_0 < \Phi < (n+1/2)\Phi_0$, the screening current reduces to $n\Phi_0$. When the external flux exceeds $(n+1/2)\Phi_0$, the flux is increased to $(n+1)\Phi_0$ by the screening current instead. With a shunt resistance, the voltage

variation is directly proportional to the change of magnetic flux. During the measurement, the sample is moved linearly across the detection coils to induce magnetic flux variations.

SQUID provides two measurement options: DC scan and RSO transport. They provide complementary approaches to measure a large range of the magnetization. For DC scan, the sample is moved linearly over a few centimeters (usually 4cm), and a number of voltage signal are collected during the movement. By subsequent fitting of these data points, the magnetization of the sample can be obtained. The detection coils are located at the center of the movement path.

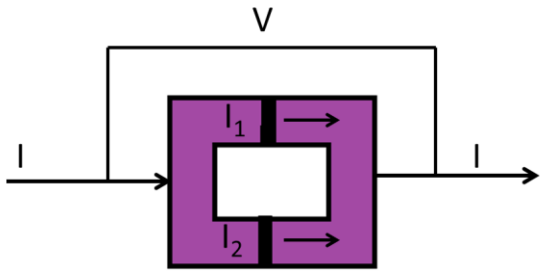

Figure 2-14 Diagram of a DC SQUID. Two superconducting regions are separated by insulating layers (black).

Compared to DC scan, RSO option is relatively faster and is more sensitive to the small magnetic moments. The sample is oscillating at the max slope position during the measurement. Depending on the magnitude of magnetization of samples, DC or RSO is chosen for specific sample. The SQUID instrument can measure the magnetic moments from 1.8 K to 400 K with a magnetic field up to 7 T.

Chapter 3 Thermoelectric Properties of $Bi_2Sr_2Co_2O_y$ Thin Films and Single Crystals

In this chapter, we are going to look in detail at the experiments and the analysis of the thermoelectric properties of a layered cobaltite $Bi_2Sr_2Co_2O_9$, in the form of both single crystal and thin films. Essentially we are looking most closely at how the thermoelectric properties vary with different forms. Moreover, the oxygen vacancies are believed to play important roles in tuning the properties.

3.1 Background

Compounds consisting of alternative conductive and insulating layers were proposed to have large Seebeck coefficient because the electrons are confined to move in two dimensions.[7] This directly reduces the dimensionality of electron movement and forms quantum-well like structures. As a result, the electronic density of states could significantly increases and enhances the Seebeck coefficient which directly depends on the derivative of density of states. Moreover, owing to the near absence of alloy scattering and random interface carrier scattering, high in-plane carrier mobility is possible, benefiting the electrical conductivity. Thermal conductivity, on the other, could be significantly reduced, due to the localization of lattice vibrations. In fact, by choosing different complex blocks, the thermal conductivity could be further reduced.[67] After Terasaki et al. discovered large Seebeck coefficient in layered $NaCo_2O_4$,[68] researchers began to realize the important contributions from spin degeneracy to Seebeck coefficient in strongly correlated electron systems.[21]

Layered cobaltates have attracted great attention for both their fundamental aspects and applications. The common feature is that they consist of CoO_2 layers formed by edge-sharing CoO_6 octahedra. Depending on the interlayer spacer, they may exhibit superconductivity [69],

ionic conduction [70], or good thermoelectric properties [13, 15, 21, 71, 72]. The latter is particularly unexpected because traditional thermoelectric materials are usually semiconductors involving heavy-mass elements such as Bi_2Te_3 [73]. Layered cobaltates like Na_xCoO_2 and $Ca_3Co_4O_9$ contain much lighter elements, yet exhibiting high thermoelectric power (S), low electrical resistivity (ρ), and low thermal conductivity (κ) [13, 18, 71]. These are desired properties for thermoelectric applications, since the efficiency is determined by a quantity called the figure of merit $ZT = S^2/(\rho \cdot \kappa)$. It is considered that CoO_2 layers are responsible for low ρ and low κ. But it is not obvious why this class of materials has high S. Possible mechanisms for large S in cobaltates include (1) the unique electronic structure with the Fermi energy level locates at the edge of a narrow band [8], and (2) the low spin state of Co^{3+} [21]. According to band calculations [8], $Bi_2Sr_2Co_2O_9$ is expected to exhibit higher thermoelectric power than that of Na_xCoO_2 and $Ca_3Co_4O_9$. This prediction is in contradiction with the second scenario, as stoichiometric $Bi_2Sr_2Co_2O_9$ contains Co^{4+} only. On the other hand, oxygen vacancy exists which makes the compound known as $Bi_2Sr_2Co_2O_y$ with $y < 9$. Oxygen vacancy will lead to the mixed valence of Co, thus tuning the thermoelectric properties.

$Bi_2Sr_2Co_2O_9$ exhibits the monoclinic symmetry consisting of two subsystems: a $Bi_2Sr_2O_4$ rock-salt (RS) layer and a CoO_2 (CO) layer [32, 35]. As depicted in Figure 3-1(a), these layers are stacked alternately along the c axis with identical lattice parameters a and c, and angle β, but different lattice parameter b (b_{RS} for the $Bi_2Sr_2O_4$ and b_{CO} for CoO_2). As b_{RS} and b_{CO} are incommensurate [74], $Bi_2Sr_2Co_2O_9$ is characterized to have a misfit structure similar to $Ca_3Co_4O_9$. In addition to the enhancement of phonon scattering for low thermal conductivity, the highly-strained RS layer may give rise to strong electron-phonon coupling [75]. One way to tune such strain is to use different alkaline-earth (AE) metals: the ratio of b_{RS}/b_{CO} increases with increasing

the ionic size of AE, and becomes commensurate when AE = Ba with $b_{RS}/b_{CO} = 2$ [76]. Depositing the material in a substrate should be another effective way to tune the strain. So far, $Bi_2Sr_2Co_2O_y$ has been grown on $LaAlO_3$ and fused silica substrates [77, 78]. Although films grown on fused silica are more epitaxial than that on $LaAlO_3$, the thermoelectric properties are superior in the latter case [77], suggesting that strain plays certain role. In this Letter, we report the thermoelectric properties of $Bi_2Sr_2Co_2O_9$ thin films and single crystals. Comparing our data with others obtained from literature, we discuss the thermoelectric performance of $Bi_2Sr_2Co_2O_9$ in various forms.

3.2 $Bi_2Sr_2Co_2O_9$ Single Crystals and Thin Films: Synthesis and Structures

The $Bi_2Sr_2Co_2O_y$ single crystals were grown by the floating-zone technique, as shown in Figure 2-4(a). The initial chemicals of Bi_2O_3, $SrCO_3$ and Co_3O_4 in stoichiometric molar ratio of 1: 2: 2/3 were well mixed and sintered at 900 °C for 24 hours to form polycrystalline $Bi_2Sr_2Co_2O_y$. After grinding, the reactants were pressed under hydrostatic pressure into two rods with 8 mm diameter and a length of ~ 10 cm for the feed rod and of ~ 3 cm for the seed rod. Crystals were grown at a speed 1.5 mm/h and rotation speed of 20 rpm in air. The resultant crystals have easy cleavage planes perpendicular to the growth direction. The $Bi_2Sr_2Co_2O_y$ thin films were deposited on sapphire (α-Al_2O_3 with the hexagonal structure a = 4.76 Å and c = 12.99 Å) substrates by the pulsed laser deposition (PLD) technique under different growth temperatures and oxygen pressure. The films reported here were grown under 0.03 torr oxygen pressure at growth temperatures 625, 650, 675, 700, and 750 °C, respectively.

The structures of films and crystals were investigated by x-ray diffraction (XRD) using Cu Kα 1 radiation (wavelength = 1.54056 Å) at room temperature. The structures of films were also studied using a VG603 scanning transmission electron microscopy (STEM) operated at 300

keV to obtain high angle annular dark field (also known as Z-contrast) images. The characterizations of the thermoelectric properties of films and crystals were performed in a Physical Property Measurement System (PPMS) using the four-probe method. The Seebeck coefficient and thermal conductivity of crystals were simultaneously measured on samples with typical size of ~ 2 mm × 2 mm × 8 mm. For accurate measurements, the electrical resistivity and Hall coefficient were measured separately on samples with typical size of 2 mm × 0.2 mm × 5 mm. For the crystal samples, thermoelectric properties measurements were performed twice before and after the samples sintered in Ar atmosphere for 50 hours at 500 °C.

Figure 3-1(b) and (c) show the XRD patterns of films grown under 0.03 torr oxygen at 750 °C and 625 °C, respectively. In both cases, the major peaks correspond to the $Bi_2Sr_2Co_2O_9$ phase, as indicated by dots. For the film grown at 750 °C (Figure 3-1(b)), there are signals from the Al_2O_3 substrate (indicated by *) and unknown phases (marked by triangles). XRD intensity from unknown phases decreases with decreasing growth temperature, becoming almost undetectable for the film grown at 625 °C. This suggests that the films grown at lower temperatures have purer desired phase. To understand how impurity phases developed during the growth, films were investigated using STEM. Figure 3-1(d) shows the Z-contrast image of the film grown at 750 °C. Two features are worth noting: (1) the film is mostly single crystallized with well-stacked sequence Bi-O, Sr-O and Co-O, corresponding to the $Bi_2Sr_2Co_2O_9$ phase (see Figure 3-1(a)); and (2) irregular stacking occurs in the first couple of layers next to the substrate. The latter should be the cause for the unknown peaks in XRD pattern (see Figure 3-1(b)). These unidentified phases have very similar layered structure(s) as $Bi_2Sr_2Co_2O_9$. Figure 3-1(e) shows the XRD pattern from powder by crushing single crystals grown by floating zone method, as shown in the inset. All peaks can be indexed with the $Bi_2Sr_2Co_2O_9$ phase with a = 4.99 Å, b =

5.43 Å, and c = 14.89 Å. The lattice parameter c for films is expected to be the same, as all c-axis peak positions are the same in both films and single crystals (Figure 3-1(c)-(e)).

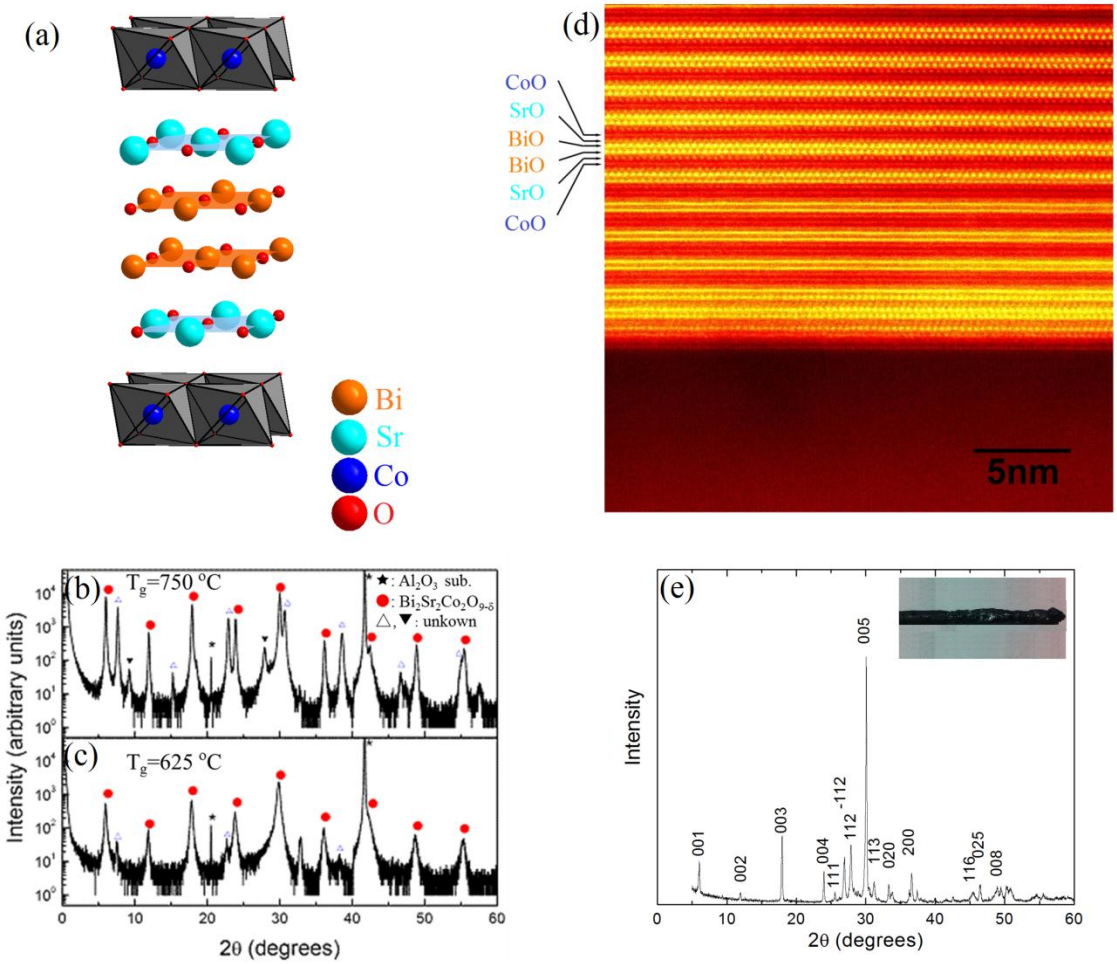

Figure 3-1 (a) Schematic crystallographic structure of $Bi_2Sr_2Co_2O_9$; (b-c) XRD patterns of the $Bi_2Sr_2Co_2O_y$ films on Al_2O_3 grown at 750 °C (b) and 625 °C (c), respectively; (d) TEM image of film grown on Al_2O_3 substrate at 750 °C; (e) XRD pattern of a grounded $Bi_2Sr_2Co_2O_y$ crystal. Inset is the grown crystal by floating zone method.

3.3 Thermoelectric Properties of $Bi_2Sr_2Co_2O_9$ Single Crystals and Thin Films

Figure 3-2 (a) displays the temperature dependence of electrical resistivity (ρ) of $Bi_2Sr_2Co_2O_y$ thin films with the thickness of 1000 Å between 100 and 400 K. For all our film samples, resistivity increases with decreasing temperature. Such semiconducting behavior is

quite different from the films that grown on $LaAlO_3$ or fused silica which show metallic behavior above ~100 K [77, 78]. Quantitatively, ρ for our films initially decreases with decreasing growth temperature then increases after reaching the minimum for the film grown at 700 °C. Such non-monotonic behavior between resistivity and growth temperature is unexpected. As these films were deposited under the same atmosphere (0.03 torr oxygen pressure), the major difference between them would be the reduction of unknown phases with decreasing the growth temperature, which would lead to the monotonic change of ρ with the growth temperature. It is possible that the growth temperature impacts the oxygen content y. With the fixed growth temperature but varied oxygen pressure, electrical resistivity becomes higher than presented in Figure 3.2(a). We thus consider that the growth condition for the film grown at 700 °C is optimal on the Al_2O_3 subtract. Note that ρ for the film grown at 700 °C is (1) almost temperature independent, and (2) even lower than that obtained from the film grown on $LaAlO_3$ [77, 78]. This suggests that strain due to subtracts may play certain role in physical properties of $Bi_2Sr_2Co_2O_y$ films.

Figure 3-2(b) shows the temperature dependence of Seebeck coefficient (S) of the thin films between 100 and 400 K. In this temperature range, S is positive for all samples, implying hole-dominant electrical transport. For each film, the magnitude of S increases with increasing temperature at low temperatures, then tends to saturate above 250 K, except the one for the film grown at 750 °C. Similar to that is seen in electrical resistivity, S depends non-monotonically on the growth temperature. For example, with decreasing growth temperature, S(T = 300 K) initially increases then decreases after reaching the maximum for the sample grown at 675 °C. The maximum Seebeck coefficient (~ 120 μV/K) obtained at 400 K is comparable to the reported value for the film grown on $LaAlO_3$ [77, 17].

Figure 3-2(c) depicts the temperature dependence of electrical resistivity for a $Bi_2Sr_2Co_2O_y$ single crystal between 2 and 400 K. For the as-grown single crystal, ρ decreases with decreasing temperature down to ~ 20 K with a slow upturn at lower temperatures. While theoretical calculations suggest that $Bi_2Sr_2Co_2O_9$ has metallic ground state [8, 79], the low-temperature upturn is attributed to the charge ordering of Co^{3+} and Co^{4+} [35] or pseudogap formation [77, 80]. In the former case, it has to be due to oxygen deficiency so to cause mixed Co^{3+} and Co^{4+}. From this point of view, our as-grown single crystals are closer to stoichiometry. To confirm, the as-grown single crystal was annealed at 500 °C in Ar atmosphere for 50 hours. Such annealing is expected to reduce oxygen, i.e., forming $Bi_2Sr_2Co_2O_{9-\delta}$ with $y = 9 - \delta < 9$. As shown in Figure 3-2(c), resistivity of the Ar-annealed single crystal exhibits non-metallic character ($d\rho/dT < 0$), similar to that seen in our films (Figure 3-2(a)) and the film on silica [16]. Thus, it is conceivable that the upturn of electrical resistivity is related to oxygen deficiency. From this point of view, the film grown at 700 °C is also close to stoichiometry.

In addition to the annealing effect in electrical resistivity, $Bi_2Sr_2Co_2O_y$ single crystals reveal interesting features in Seebeck coefficient (S). Figure 3-2(d) shows the temperature dependence of S for both as-grown and Ar-annealed $Bi_2Sr_2Co_2O_y$. Note that S increases with increasing temperature without sign of saturation in both cases, which is different from that in films (Figure 3-2 (b)). On the other hand, S is enhanced upon the annealing of the single crystal in Ar atmophere, reaching ~ 135 μV/K at 400 K. The increase of both resistivity (Figure 3-2 (c)) and S (Figure 3-2(d)) suggests that Ar annealing reduces carrier concentration in single crystals. According to previous studies [74, 81], the conduction carriers in $Bi_2Sr_2Co_2O_9$ are hole dominant. Annealing in Ar atmosphere likely reduces oxygen content, thus reducing hole concentration.

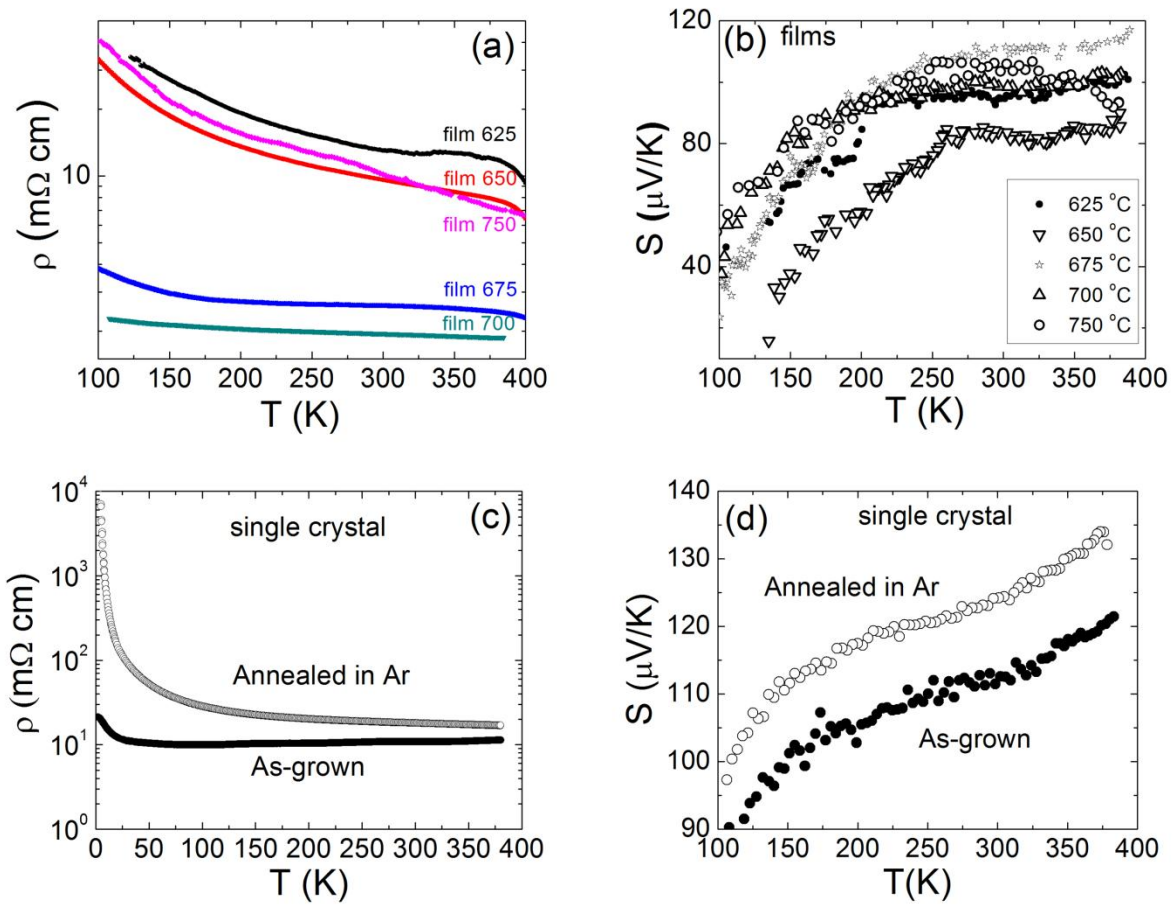

Figure 3-2 Temperture dependence of electrical resistivity (a) and thermpower (b) of the films grown at 625, 650, 675, 700, 750 °C, respectively; (c-d) are temperature dependence of resistivity (c) and Seebeck coefficient (d) of the as-grown and Ar-annealed single crystal samples.

To confirm the carrier type, Hall effect measurements are performed, which reveal positive Hall coefficient (not shown). This is consistent with the positive *S* shown in Figure 3-2, indicating that the conduction carrieres are indeed hole dominant. Figure 3-3(a) shows the temperature dependence of carrier concentration deduced from Hall coefficient. Among films, the carrier concentration tends to decrease with decreasing temperature with the magnitude varying between 10^{16} (film grown at 625 °C) and 10^{19} C/cm^3 (film grown at 675 °C). The carrier concentration of the annealed single crystal exhibits similar temperature dependence as those films, consistent with the semiconducting behavior revealed by electrical resistivity. In contrast,

the carrier concentration for the as-grown single crystal decreases with increasing temperature due to the metallic conduction. To understand the relationship between carrier concentration and electrical conduction, we plot room-temperature ρ versus *n* in Figure 3-3(b). For films, the trend is obvious: higher carrier concentration corresponds to lower electrical resistivity. While crystals show similar trend, their resistivities are roughly three times higher than that of films with the same carrier concentrations. It is likely that the resistivity for our single crystals is overestimated due to error introduced by geometrical configurations, as previous report gave much smaller resistivity for single crystals with similar ρ(T) profile [82].

Seebeck coefficient in layered cobaltates (Na_xCoO_2 [13], $Ca_3Co_4O_9$ [71]) is usually explained by Heike's formula $S = -\frac{k_B}{e}\ln\left(\frac{g_3}{g_4}\frac{x}{1-x}\right)$, where g_3, g_4 are the numbers of possible states of Co^{3+} and Co^{4+} ions, respectively, and *x* is the concentration of Co^{4+} ions [21]. In the simplest case, the optimum Seebeck coefficient is expected to reach $2k_B/e$ = 170 μV/K (k_B is the Boltzmann constant and e is electrical charge) with optimum carrier concentration in the order of 10^{19} C/cm [15, 83]. While the carrier concentration for as-grown single crystals and films grown at 675 °C is at the optimal level, their Seebeck coefficient is in the order of 110 μV/K (at 300 K), lower than the expected value.

Interestingly, annealing our $Bi_2Sr_2Co_2O_y$ single crystals in Ar results in the enhanced Seebeck coefficient (Figure 3-2(d)) but increased resistivity (Figure 3-2(c)) and reduced carrier concentration (Figure 3-3(a)). This is a typical trend seen in bulk materials. The variation of ρ and *S* observed in films seems different from that in single crystals. Compared to single crystals, a film deposited in the $LaAlO_3$ substrate reveals lower ρ and higher S, while the film deposited in silica has higher ρ and lower S [16]. For comparision, we plot both ρ(T = 300 K) and *S*(T = 300

K) for our films in Figure 3-3(c). Remarkably, upon the variation of the growth temperature, ρ(T = 300 K) and S(T = 300 K) exhibit opposite trend, i.e., a film with higher S has lower ρ and vice versa. We recall that there is similar trend in Na_xCoO_2, in which Seebeck coefficient increases but electrical resistivity decreases with increasing x in the range of $0.55 \leq x \leq 0.75$ [84]. Obviously, the combined high S and low ρ would lead to high power factor, S^2/ρ, which is in favor of thermoelectric performance.

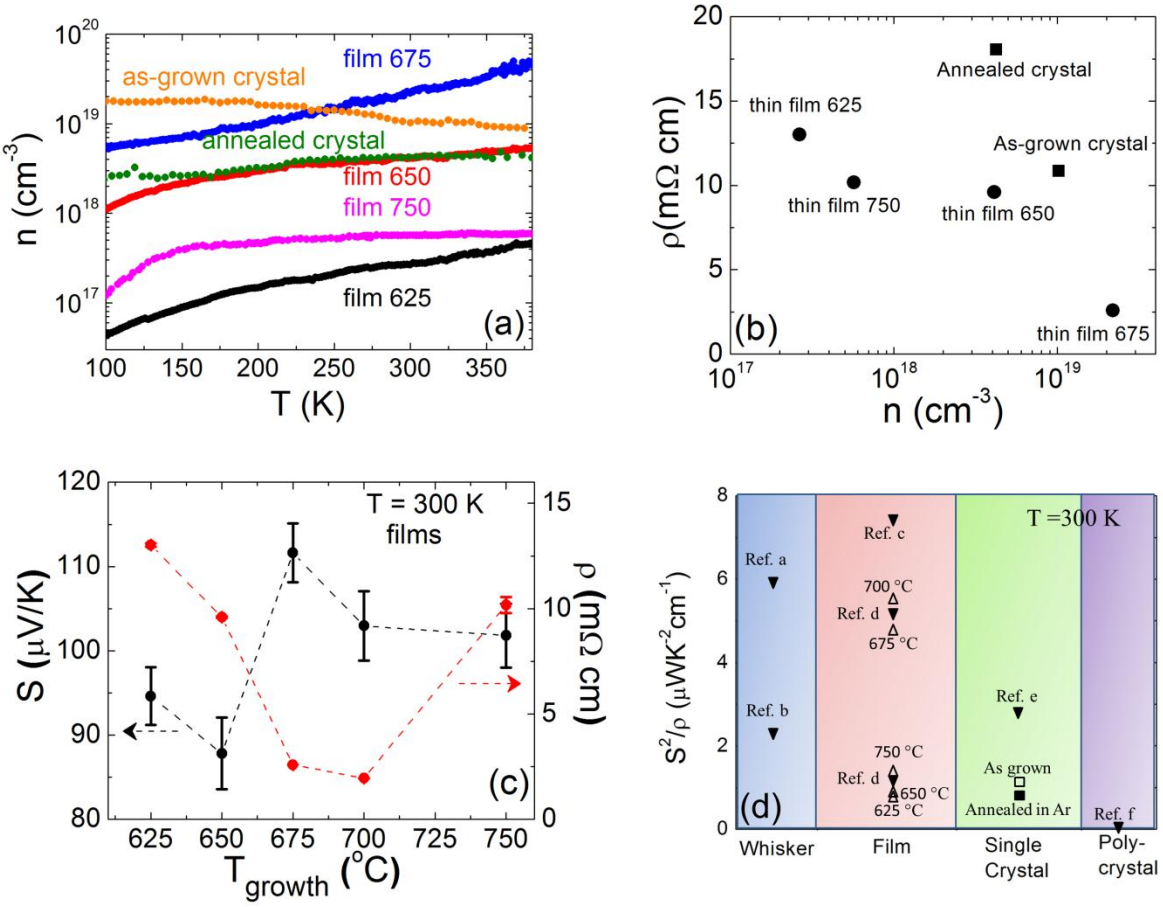

Figure 3-3 (a) Temperature dependence of carrier concentration n deduced from Hall coefficient for as-grown and annealed crystals, and films grown at 625 °C, 650 °C, 675 °C, and 750 °C; (b) Electrical resistivity versus carrier concentration at T = 300 K; (c) The growth temperature dependence of thermpower and electrical resistivity of films at 300 K; (d) The power factor of films and crystals compared to reported results from samples with various forms (whiskers Ref.a,b [85, 86], films Ref.c, d [77, 78], single crystals Ref.e[29], and polycrystal Ref.f[30]).

As pointed out by Ierasaki [83], although Seebeck coefficient has been discussed with the Heikes formula for transition-metal oxides, little is known on how the electrical resistivity is described in the same condition. For the system with non-metallic conduction, the power factor is expected to be independent on the carrier concentration [83]. This is apparently not true for $Bi_2Sr_2Co_2O_y$ films as shown in Figure 3-3(d): S^2/ρ for film grown at 700 °C is more than 5 times larger than that for the film grown at 625 °C. For comparison, Figure 3-3(d) also shows power factor obtained from $Bi_2Sr_2Co_2O_y$ in other forms including polycrystals, single crystals, and wishers. It can be seen that S^2/ρ depends not only on sample in each form but also on sample dimensionality. Overall, lower dimensionality is in favor of high power factor, consistent with the theoretical prediction [87].

With reduced dimensionality, the thermal conductivity (κ) of a system is usually reduced because of enhanced phonon scattering [87]. When material is prepared in forms other than bulk, it is also techniqually challenge to accurately measure κ. Thermal conductivity obtained from single crystals may be considered as the upper bound of thin films. Figure 3-4(a) shows the temperature dependence of in-plane thermal conductivity of $Bi_2Sr_2Co_2O_y$ single crystals before and after annealing between 100 and 400 K. Both increase with increasing temperature, and are almost coincident with each other. It is worth noting that the magnitude of theraml conductivity is much lower than that for $Na_{0.5}CoO_2$ compound [18], which can be attributed to its misfit crystal structure and thick block layer ($Bi_2Sr_2O_4$). Since the thermal conductivity for both as-grown and annealed samples remians unchanged, the electronic contribution to κ is neglegible, i.e., the total thermal conductivity is mainly contributed from phonon. Therefore, we estimate the figure of merit *ZT* for single crystals and films using thermal conductivity presented in Figure 3-4(a). Figure 3-4(b) displays the temperature dependence of *ZT*, which increases with increasing

temperature. At room temperature, the *ZT* of the as-grown crystal is about 0.02. After annealing, *ZT* decreases due to poor electrical resistivity. The film has significantly higher *ZT* than crystals, reaching 0.12 at 400 K.

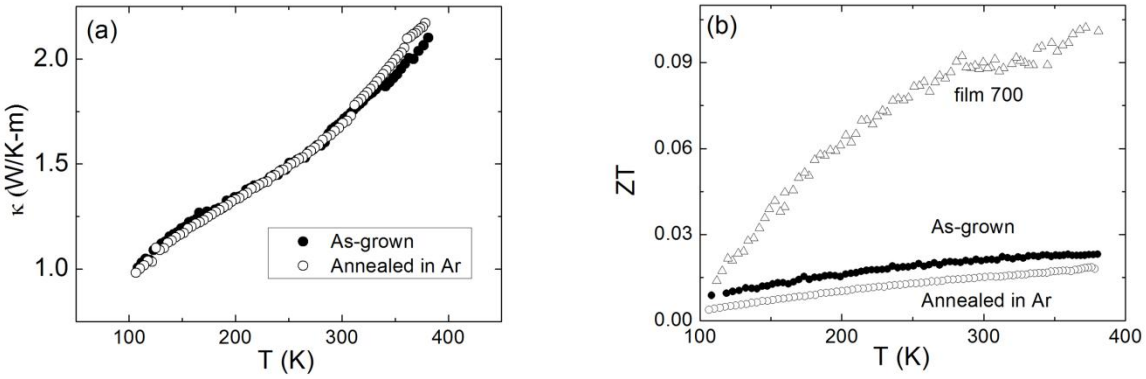

Figure 3-4 The temperature dependence of thermal conductivity (a) and figure of merit *ZT* (b) of as-grown and annealed single crystals. The *ZT* of the film grown at 700 °C is estimated using thermal conductivity shown in (a).

In summary, we have investigated the thermoelectric properties of $Bi_2Sr_2Co_2O_y$ in both the thin-film and single-crystal forms. While all films were grown under the same oxygen atmosphere, their Seebeck coefficient, resistivity, and carrier concentration vary non-monotonically with growth temperature. This indicates that property change cannot be simply due to impurity phase seen in films grown at high growth temperatures. Remarkably, the Seebeck coefficient and electrical resistivity of these films vary with growth temperature in opposite trend: Seebeck coefficient increases while electrical resistivity decreases. This provides great opportunity to tune power factor, which reaches the maximum in the film grown at 700 °C, which is much higher than that for single crystals. Based on the thermoelectric property measurements on single crystals, oxygen vacancy is one of factors that impact the thermoelectric performance in this material. Overall, samples under confined dimensionality show better

thermoelectric properties. Although all films display non-metallic behavior, the high Seebeck coefficient and low thermal conductivity and metallic conduction seen in single crystals strongly suggest that it is possible to improve the thermoelectric performance of $Bi_2Sr_2Co_2O_9$ when prepared in optimal condition.

Chapter 4 Synthesis, Structure and Electrical Properties of $PdCoO_2$

4.1 Crystal Structure of $PdCoO_2$

The obtained single crystal by metathetical reaction is typically hexagonal, as shown in Figure 2-1. The schematic crystal structure is shown in Figure 4-1(a). The XRD pattern of several pieces of single crystals exhibit strong c axis preference, as shown in Figure 4-1(b).

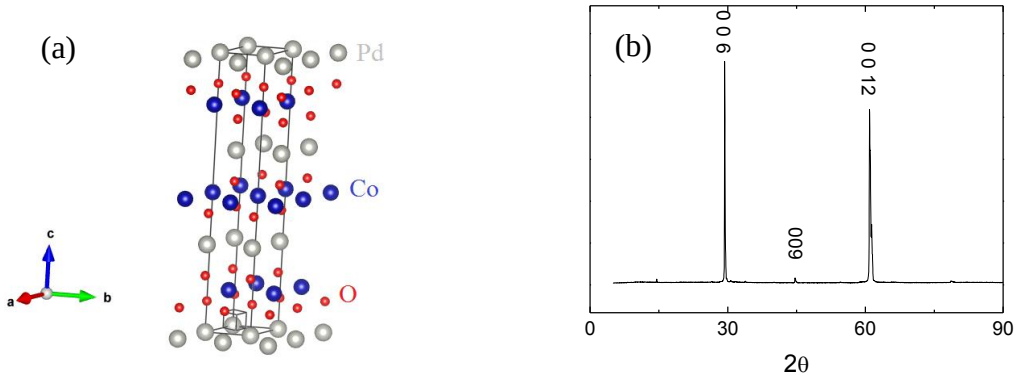

Figure 4-1 (a) Crystal structure of $PdCoO_2$. (b) XRD pattern of the $PdCoO_2$ single crystal.

Refined crystal structure of single crystal XRD result is tabulated in Table 4-1. $PdCoO_2$ crystallize in the trigonal R-3m1 (no.166). It forms layered structure consisting of CoO_2 layers and Pd layers. These layers stack along the c axis which is consistent with the XRD result.

Table 4-1 Crystal structures of $PdCoO_2$ with the space group Trigonal, R-3m1 (Hexagonal) at 293K determined by single crystal X-ray diffraction. The lattice parameters are a = b = 2.8303(3) Å and c = 17.753(2) Å. R = 0.031, wR = 0.082.

atom	site	x	y	z	U_{iso}/U_{eq}
Pd	3a	0	0	0	0.0070(2)
Co	3b	0	0	0.5	0.0053(2)
O	6c	0	0	0.1121(2)	0.0059(6)

4.2 Electrical Resistivity of $PdCoO_2$

Figure 4-2 shows the electrical resistivity measurements of several selected single crystals. Three samples #1, 2 and 3 were measured along the ab plane. As shown in Figure 4-2 (a), all three samples are metallic. They are illustrated in logarithmic scale to better show the strong temperature dependence of the ab plane resistivity in the whole temperature range.

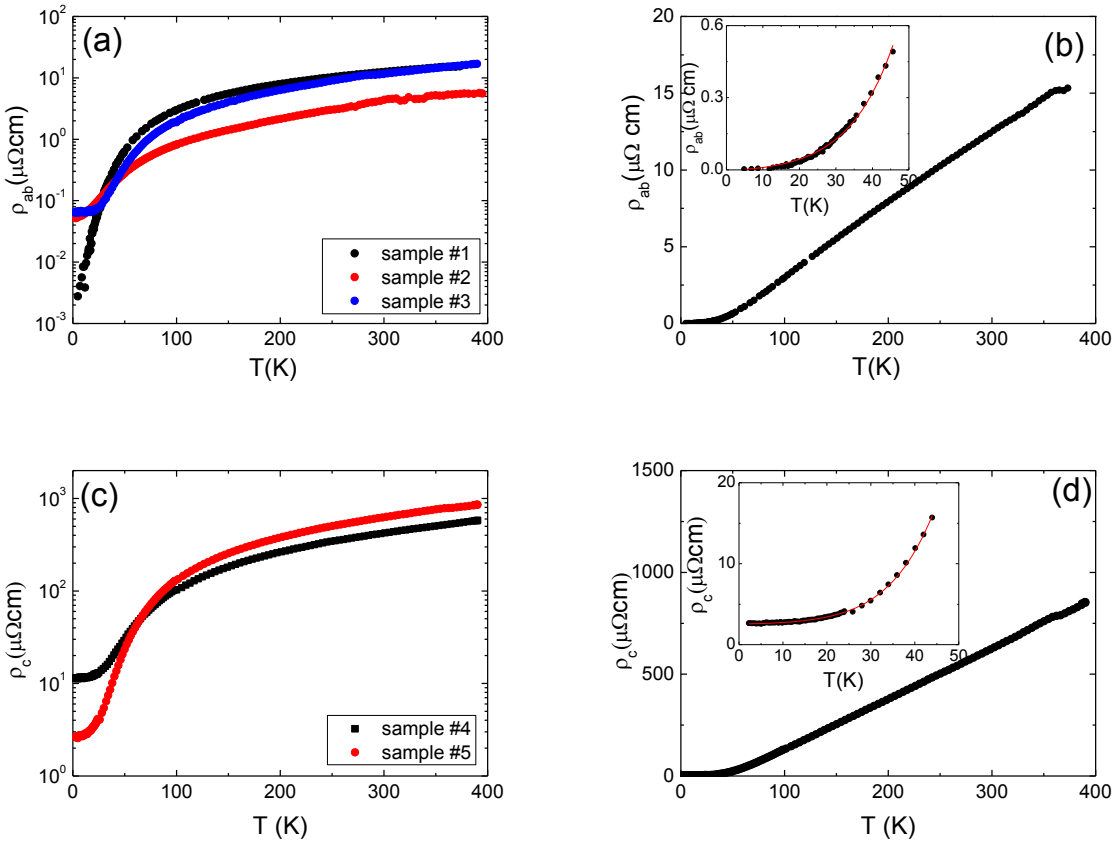

Figure 4-2 Electrical resistivity measurements of (a) samples #1, 2, and 3 along ab plane, (b) samples #3 along ab plane, (c) samples #4, and 5 along c axis and (d) sample #4 along c axis. The inset in (b) and (d) is the enlarged result from 0 to 50 K.

At room temperature, all three samples have a magnitude of a few μΩ cm which is close to reported values.[36, 88-91] However, the low temperature resistivity (residual resistivity) shows strong sample dependence. As temperature approaching 0 K, the resistivity is attributed to the impurities scattering which is dominant at very low temperatures. Hence, the residual resistivity

as well as ρ(300K)/ρ(2K) could indicate the quality of single crystals. For all the three samples, ρ(300K)/ρ(2K) is 406, 81, and 177, respectively. We choose sample #1 for further analysis.

The resistivity of sample #1 decreases to the order of nΩ cm at low temperatures. Above 50 K, the resistivity exhibits linear temperature dependence, which is attributed to the electron-phonon coupling.[90] At low temperatures, as shown in the inset in Figure 4-2(b), the resistivity can be well fitted by $\rho = A + BT^2 + CT^5$, where $B = 9.88 \times 10^{-5}$ μΩ cm/K^2, $C = 1.58 \times 10^{-9}$ μΩ cm /K^5. For a normal metal, resistivity usually has a T^2 term at very low temperatures, due to electron-electron scattering. The T^5 term comes from electron phonon coupling at low temperatures.

Figure 4-2 (c) shows the electrical resistivity along the c axis for samples #4 and 5. Similarly, strong temperature dependence was found. $\rho_c(300K)/\rho_c(2K)$ is 40 and 238 for sample # 4 and 5, mainly due to large difference of residual resistivity at low temperatures near zero. Figure 4-2(d) shows the resistivity at low temperatures (inset) and the whole temperature range. As shown in the inset, low temperature resistivity can be fitted well with the form $\rho = a + bT^2 + cT^5$, where bT^2 and cT^5 terms correspond to the electron-electron scattering and electron-phonon coupling, respectively. The fitting gives $b = 1.64 \times 10^{-3}$ μΩ cm/K^2 and $c = 6.23 \times 10^{-8}$ μΩ cm/K^5. At high temperatures, the resistivity exhibits linear temperature dependence which is also due to electron phonon coupling.

It is worth noting that ρ_{ab} only has the order of nΩ cm at low temperatures, corresponding to a transport mean free path of a few microns. This can be also interpreted as defect density which is in the order of one per 10^5 for $PdCoO_2$. This is a remarkable value for flux-grown single crystals.

Chapter 5 Thermoelectric Properties of $Sr_3(Ru_{1-x}Mn_x)_2O_7$ Single Crystals

5.1 Effect of Mn Doping in $Sr_3(Ru_{1-x}Mn_x)_2O_7$

$Sr_3Ru_2O_7$ crystallizes with a tetragonal structure with space group I4/mmm. Two distorted $SrRuO_3$ layers stack along the c axis, separated by SrO layers, as shown in Figure 5-1(a). The RuO_6 octahedra are connected to each other by the way of corner-sharing.

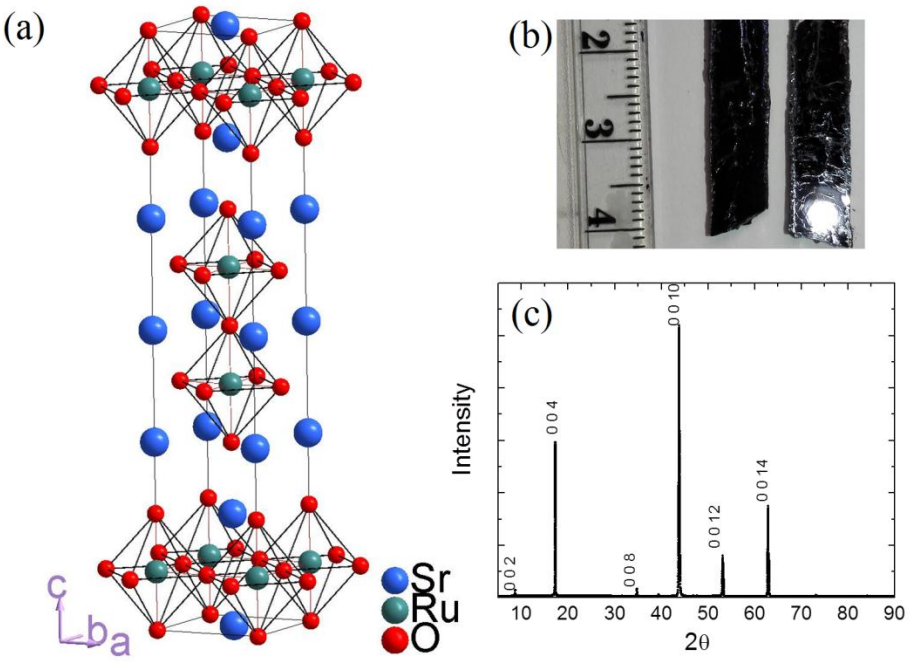

Figure 5-1 (a) Schematic picture of $Sr_3Ru_2O_7$, RuO_6 are connected to its neighbor by corner sharing. (b) Selective picture of grown $Sr_3(Ru_{1-x}Mn_x)_2O_7$, the ruler scale shown is 1 cm. (c) XRD result of the single crystal piece of $Sr_3(Ru_{1-x}Mn_x)_2O_7$. The index labeled is based on the standard pattern for $Sr_3Ru_2O_7$.

As revealed by powder neutron diffraction measurement, the octahedron has a rotation of 6.8 °about the c axis, and the Ru-O-Ru angle is about 165 °.[57] As revealed by single crystal X-ray diffraction measurement, upon Mn doping on the Ru site, the unit cell volume shrinks and the rotation angle becomes smaller and disappear when Mn doping level is above 16%. In this work, $Sr_3(Ru_{1-x}Mn_x)_2O_7$ (x = 0.025, 0.06, and 0.016) single crystals are grown by floating zone

technique. The single crystals are easily cleaved along the c axis, as demonstrated in Figure 5-1(b). XRD result in Figure 5-1(c) of the single crystal confirms the c axis orientation of the surface.

At low temperatures with low and high magnetic fields, the electrical resistivity was observed to follow $\rho_{ab}(T) = \rho_{res} + AT^{\alpha}$ where α depends on the temperature and magnetic field. As T approaches O K, α is found to be 2 at low fields, indicating Fermi liquid behavior.[92, 93] By partially substituting Ru with Mn, the compound changes from metal to insulator. There are some features: (1) the metal-insulator transition is related to an applied magnetic field; (2) the magnitude of electrical resistivity increases significantly with Mn doping level; [60] (3) The metal-insulator transition temperature increases with Mn doping level.[50] In this work, we chose different Mn doping. As shown in Figure 5-2(a), for x = 0.025, the electrical resistivity exhibits metallic behavior where dρ/dT remains positive in the whole temperature range. At x = 0.06, the metal-insulator transition occurs around 20 K. With high value of x = 0.016, the metal-insulator transition is pushed to high temperatures around 140 K. Optical conductivity measurement suggests Mn doping opens a gap that induces the metal-insulator transition.[60]

5.2 Thermoelectric properties of $Sr_3(Ru_{1-x}Mn_x)_2O_7$ Single Crystals

Figure 5-2(b) shows the Seebeck coefficient measurements of $Sr_3(Ru_{1-x}Mn_x)_2O_7$ single crystals. In the whole temperature range, the Seebeck coefficients are positive for all different Mn doping levels, indicating the existence of hole-dominated carrier. Above 100 K, the Seebeck coefficients for all x linearly increase with temperature with very small rate, though there is a sudden jump around 300 K for x = 0.025. This linear behavior indicates metallic nature of the crystals, which is consistent with the electrical resistivity results. Though the difference is small, the Seebeck coefficient is enhanced by higher Mn doping level. This trend is similar to that in

electrical resistivity which increases with Mn doping level. But the magnitude of the variance in Seebeck coefficient by Mn doping is much smaller compared to that in electrical resistivity. Thermal conductivity values of all the single crystals with different doping levels coincide above room temperature and increase with increasing temperature.

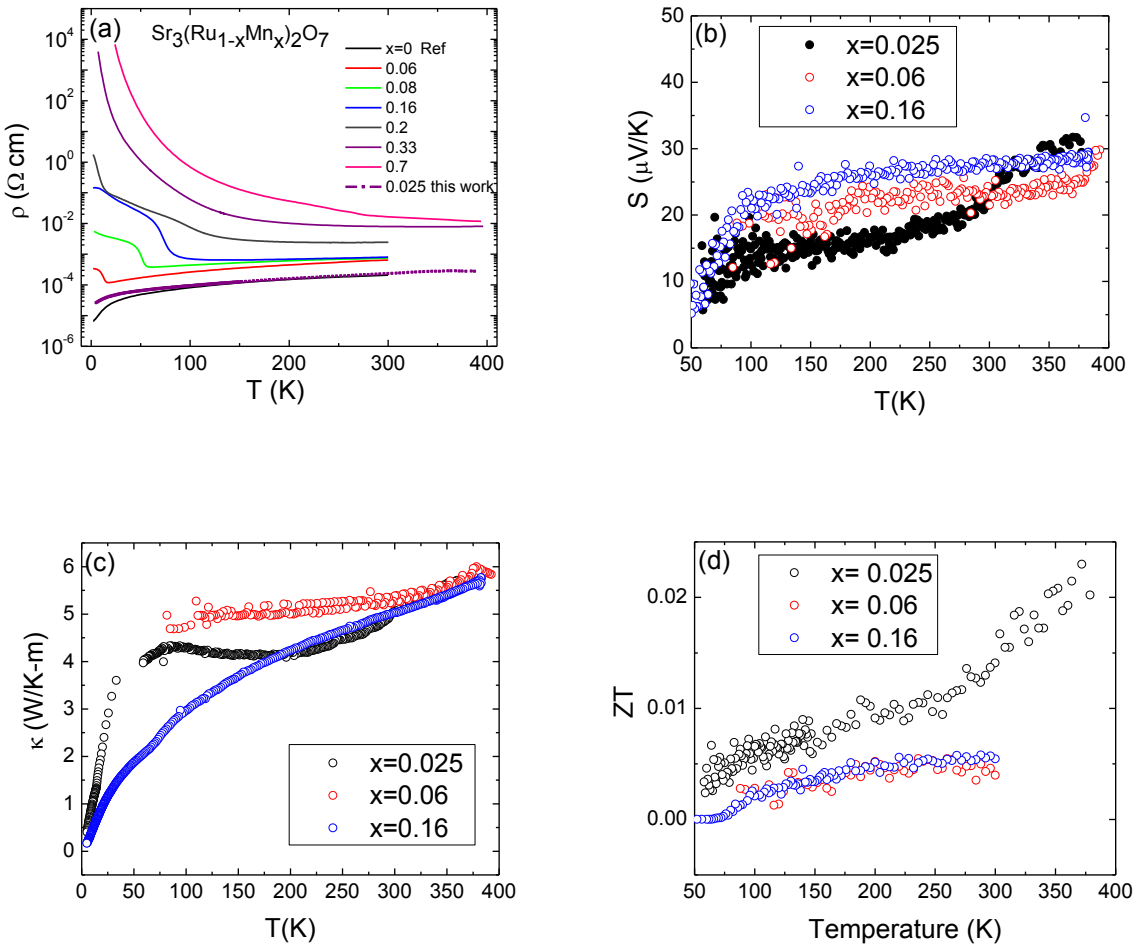

Figure 5-2 (a) The temperature dependence of ab plane electrical resistivity of $Sr_3(Ru_{1-x}Mn_x)_2O_7$ with different doping levels. The x = 0.025 is done by this work while the others are by Biao et al.[50] (b)(c)(d) Temperature dependence of Seebeck coefficient, thermal conductivity and figure of merit ZT for $Sr_3(Ru_{1-x}Mn_x)_2O_7$ with x = 0.025, 0.06 and 0.16.

Figure 5-2(c) shows the thermal conductivity measurement performed simultaneously with Seebeck coefficient measurement. The thermal conductivity below 300 K for x = 0.025

single crystal decreases first then slightly increase with decreasing temperature. At low temperatures, there is an abrupt drop. The thermal conductivity values for other two doping crystals decrease with decreasing temperature. And the thermal conductivity for x = 0.16 single crystal drops much faster at low temperatures. Overall, we find that Mn doping significantly vary the electrical resistivity but the Seebeck coefficient and thermal conductivity do not change too much, especially at high temperatures. These can be reflected in the temperature dependence of figure of merit ZT, as shown in Figure 5-2(d). The values ZT for x = 0.06 and x = 0.16 are almost the same, but the value for x = 0.025 is higher, mainly due to the much lower electrical resistivity than that of the two higher doping crystals.

For correlated systems, Seebeck coefficient depends on the entropy that is related to the degeneracy of carriers.[94] High temperature limit of Seebeck coefficient of a system of interacting localized carriers is governed entirely by the entropy change per added carrier. Mn impurities in $Sr_3Ru_2O_7$ are suggested to act as Mn^{3+} by x-ray absorption spectroscopy (XAS), in the way that the energy position of the $L_{2,3}$ absorption edge is very close to that in $LaMnO_3$.[58] However, X-ray photoelectron spectroscopy (XPS) of Mn-doped $Sr_3Ru_2O_7$ shows that the Ru 3p core levels remain identical with different Mn doping, indicating that the valence of Ru is not changed by Mn doping.[95] Hu et al. suggest that Mn is in the oxidation state of Mn^{4+}, independent of x, with unchanged band filling.[50] This can explain the Seebeck coefficient values are very close for different x, since the degeneracy related with band filling and spin of ions barely changes upon different doping levels. Moreover, the XPS result also reveals the enhanced electron localization by Mn doping.[95] From this point of view, the slightly increased Seebeck coefficient may be related to the electron localizations since Mn is more localized compared to Ru. Optical conductivity measurements suggest that Mn doping narrows the bandwidth.[60] Hence density of

states increases upon Mn doping which can account for the enhancement of Seebeck coefficient by Mn doping.

For the family of $Sr_{n+1}Ru_nO_{3n+1}$, as n increases, the dimensionality increases. The Seebeck coefficient for different n, as shown in Figure 5-3, has a minimum value at n =2. Larger n members have stronger hybridization, resulting in larger band width W. The electron-electron correlation becomes weaker since the effective Coulomb energy U/W is smaller for larger n. For correlated systems, the Seebeck coefficient usually depends on the degeneracy and has a larger value compared to simple metal. Interestingly, as n increases, the density of states $N(E_F)$ also increases and becomes sharper in the vicinity of E_F. The sharp distribution of density of states near Fermi level would enhance Seebeck coefficient for larger n.

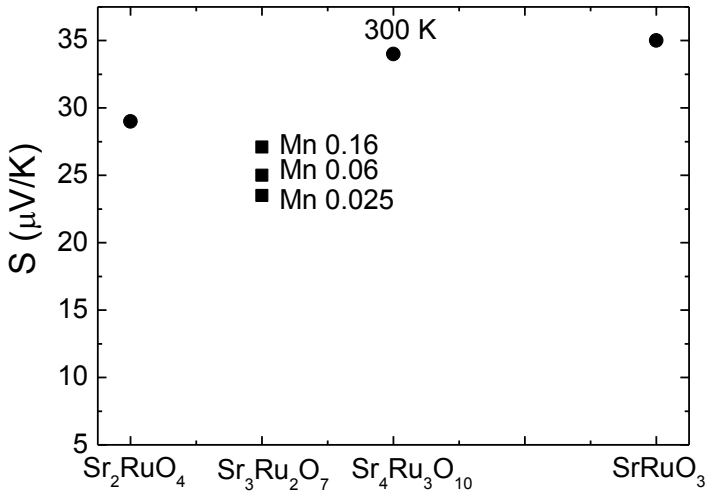

Figure 5-3 Seebeck coefficient for $Sr_{n+1}Ru_nO_{3n+1}$ family with n = 1[54], 2, 3[55] and ∞[53] at 300 K.

Chapter 6 Magnetic, Electrical and Thermal Properties of $BaMn_2Sb_2$

$BaMn_2Sb_2$ crystallizes in tetragonal $ThCr_2Si_2$-type structure[96, 97]. This is isostructural to the AFe_2As_2 (A=Ba, Sr, Ca and Eu) family and $BaMn_2Pn_2$ (Pn = As, P, Bi) family.[98-107] The former family have been found to show superconductivity on doping or by application of external pressure. [108-110] In contrast to the AFe_2As_2 family, $BaMn_2Pn_2$ has semiconducting or insulating ground states and has no structural transition.[103, 105, 107] $BaMn_2As_2$, with a AF ground state, is suggested to have intermediate behaviors between itinerant antiferromagnets AFe_2As_2 and the local moment antiferromagnetic insulator La_2CuO_4.[105, 111] The comparison with these compounds could help understand the relationship between magnetism and thermoelectricity.[112] $BaMn_2Sb_2$ was first synthesized in 1979.[96] Temperature dependence of magnetization was measured up to 300 K, and predicted to be G-type antiferromagnet.[97] The Neel temperature and ordered moment are still unknown. Strong spin dependent hybridization between Mn d states and Sb p states was reported, which is not favorable for high carrier mobility.[63] On the other hand, $BaMn_2Sb_2$ was reported to have large Seebeck coefficient of ~ 225 μV/K at room temperature, though with poor electrical conductivity.[64, 65] In this work, we report the neutron scattering measurement of single crystals to reveal the magnetic structure. We also report the thermal transport properties to help understand possible connection between thermoelectric properties and magnetism.

6.1 Synthesis and Structure

Single crystals of $BaMn_2Sb_2$ was grown out of Sn flux method. Ba rod (Alfa Aesar 99+%), Mn powder (Alfa Aesar, 99.95%), Sb powder (Alfa Aesar, 99.999%), and Sn powder (Alfa Aesar, 99.995%) were taken in the ratio of (1:2:2:5) and placed in alumina crucible. The mixing was performed in a nitrogen-filled glove box. Then the crucible was sealed in an

evacuated quartz tube. The whole assembly was first sintered at 1180 ℃ for 15 h and then slowly cooled down (5℃/h) to 700℃. At this temperature, the sealed quartz tube was taken out from the furnace, spun in a centrifuge immediately and quenched to room temperature. Sn flux was well separated. High yield of plate-like single crystals with surfaces over 5 mm × 5 mm were obtained which are very malleable and easily bent, as shown in Figure 2-2.

The compositions were checked using wavelength dispersive spectroscopy (WDS) on cleaved surfaces of the crystals. Figure 6-1 shows the WDS result of the compound. Only Ba, Mn and Sb can be found with little Sn. The average elemental ratio was found to be Ba: Mn: Sb: Sn = 20.2: 39.2: 40.4: 0.2 which is consistent with 1:2:2 stoichiometry for the $BaMn_2Sb_2$ compound. The inclusion of Sn is negligible. Moreover, extremely strong peaks along (00l) from the XRD pattern can be observed on the flat surface of crystal, indicating that the largest surface is the ab plane. The crystal structure of the crystals were identified using power X-ray diffraction (XRD) with Cu Kα (λ=0.15418 nm) radiation at room temperature. The XRD pattern was scanned in the range from 5 ºto 90 ºwith a 0.02 ºstep size.

From XRD result, we found no impurity phases in our crystals, as shown in Figure 6-2. For single crystal neutron scattering measurement, the initial unit cell parameters were taken as reported for $BaMn_2Sb_2$ ($ThCr_2Si_2$ structure, space group I4/mmm).[113] The final unit cell parameters and atomic positions were calculated from the reflections obtained at 6 K. The obtained unit cell parameters at 6 K are a = b = 4.412(2) Å, c = 14.414(8) Å which are close to the reported room temperature cell parameters.[97] The $BaMn_2Sb_2$ single crystals tend to cleave into thin plates perpendicular to the c axis.

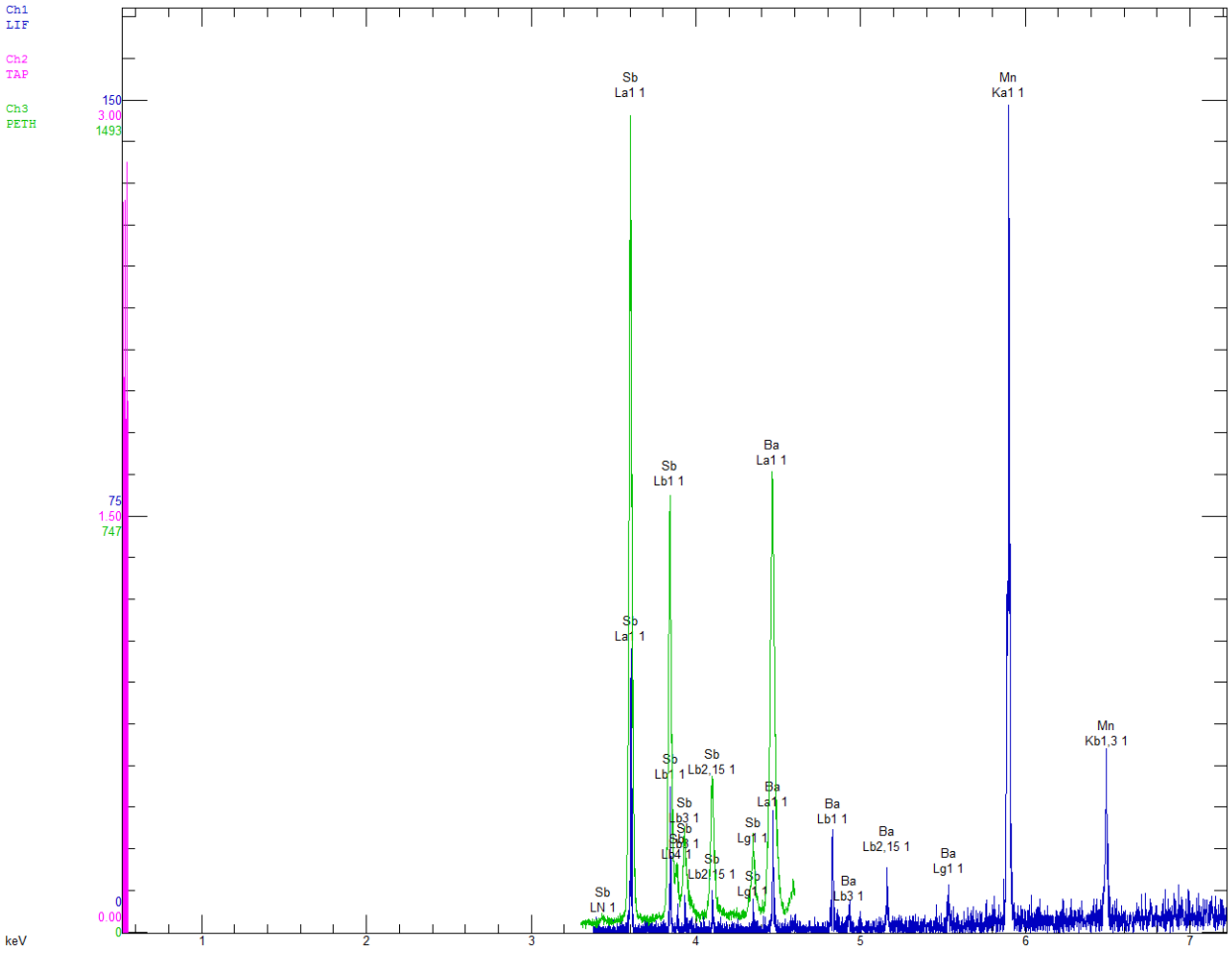

Figure 6-1 WDS result of the compound $BaMn_2Sb_2$. Different colors represent the collecting data point by different crystal detectors. They are LIF (blue), TAF (magenta), and PETH (green), respectively. The electronic core levels of the element Ba, Mn, Sb are labeled.

6.2 Thermoelectric Properties of $BaMn_2Sb_2$ Single Crystal

Electrical resistivity was measured via the four-probe method on a piece of single crystal (~2mm ×4mm ×0.6mm). Big crystals were cut into rectangular shape (~3mm ×10mm ×0.6mm) for ab plane thermoelectric property (Seebeck coefficient S and thermal conductivity κ) measurements. Electrical resistivity measurements were performed separately to avoid the effect of Joule heating during the thermal transport measurements.

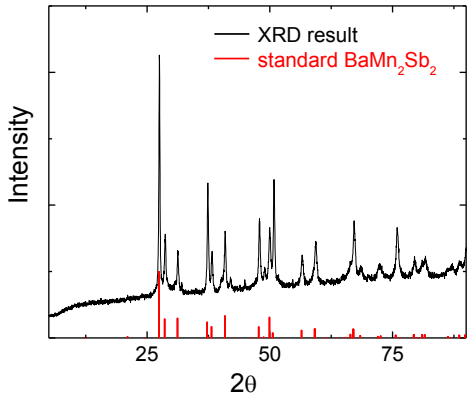

Figure 6-2 XRD result of powder crushed from $BaMn_2Sb_2$ crystal at room temperature. The standard pattern is also shown for comparison.

The thermoelectric properties were characterized in the ab plane only due to the limitations of plate like crystals. As shown in Figure 6-3, the Seebeck coefficient of pure $BaMn_2Sb_2$ is negative between 75 K and 300 K. Above 300 K, it becomes positive and the magnitude increases with increasing temperature. Below 75 K, it increases with decreasing temperature but turns down around 45 K. This change of Seebeck coefficient sign from negative to positive implies that the charge carriers change from electron-dominant to hole-dominant. However, this is quite different from the one reported that shows ~225 μV/K at room temperature.[64] When both hole and electron contribute to the transport, the total Seebeck coefficient can be represented by the Mott relation: $S = \frac{S_n\sigma_n + S_p\sigma_p}{\sigma_n + \sigma_p}$, where $S_{n,p}$, $\sigma_{n,p}$ are the Seebeck coefficient and electrical conductivity for n-type and p-type carriers, respectively. Since S_n and S_p have opposite signs, the magnitude of total Seebeck coefficient is small at low temperatures. The temperature dependence of Seebeck coefficient is very similar to that of $Ba(Fe_{1-x}Ru_x)_2As_2$.[114] The pure $BaFe_2As_2$ is negative below 300 K. By doping Ru at Fe sites, the Seebeck coefficient exhibits a negative minimum first and then shows a positive maximum with decreasing temperature. The thermal conductivity was measured simultaneously, as shown in

Figure 6-3. The curve shows phonon peak at low temperatures at around 60 K with maxima value of about 10 W/Km, similar to that of $BaMn_2Bi_2$.[104] Above 60 K, the thermal conductivity gradually decreases with increasing temperature until 250 K. Then the thermal conductivity begins to increase.

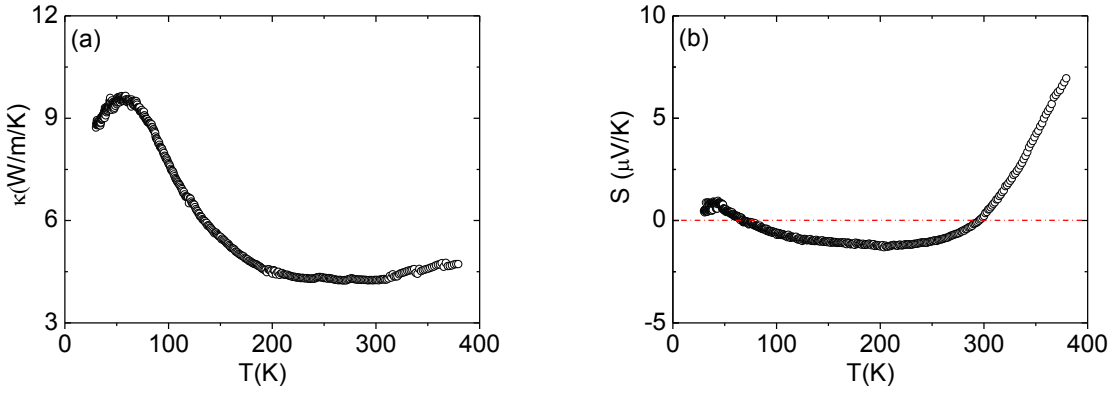

Figure 6-3 Thermal conductivity (a) and Seebeck coefficient (b) of $BaMn_2Sb_2$ measured from 30 K to 380 K.

The ab plane resistivity of $BaMn_2Sb_2$ is shown in Figure 6-4(a). Note that it increases with decreasing temperature, indicating its semiconducting nature. However, the change is much slower below 200 K. To analyze the temperature dependence of electrical resistivity, we quantitatively fit the curve. In Figure 6-4(b) the ab plane conductivity data was fitted using the formula $\sigma = \sigma_0 + Bexp(-\frac{\Delta}{2k_BT})$ where σ_0 and B are constants, k_B is the Boltzmann constant and Δ is the energy gap. From the fitting in Figure 6-4(b), we obtain σ_0 = 0.021(3) $\Omega^{-1}cm^{-1}$, B = 4830(70) $\Omega^{-1}cm^{-1}$, and Δ = 0.411 eV. At low temperatures, we fit the ab plane resistivity as shown in Figure 6-4(c) and obtain $\rho = -6.47(5)\,\mathrm{lnT} + 77.2(1)$ Ω-cm. This crossover from activated exponential to the logarithmic temperature dependence imply anomalous scattering rate temperature dependence, quite similar to the behavior of $Ba_2Mn_2Sb_2O$.[115] Origin of the scattering

in $Ba_2Mn_2Sb_2O$ can be attributed to a phase transition in ab plane at around 60 K, confirmed by both magnetic susceptibility measurement and specific heat measurement. In our $BaMn_2Sb_2$ compound, however, the situation is different. Though $BaMn_2Sb_2$ has antiferromagnetic ground state, there is no sign of phase transition observed in specific measurement.

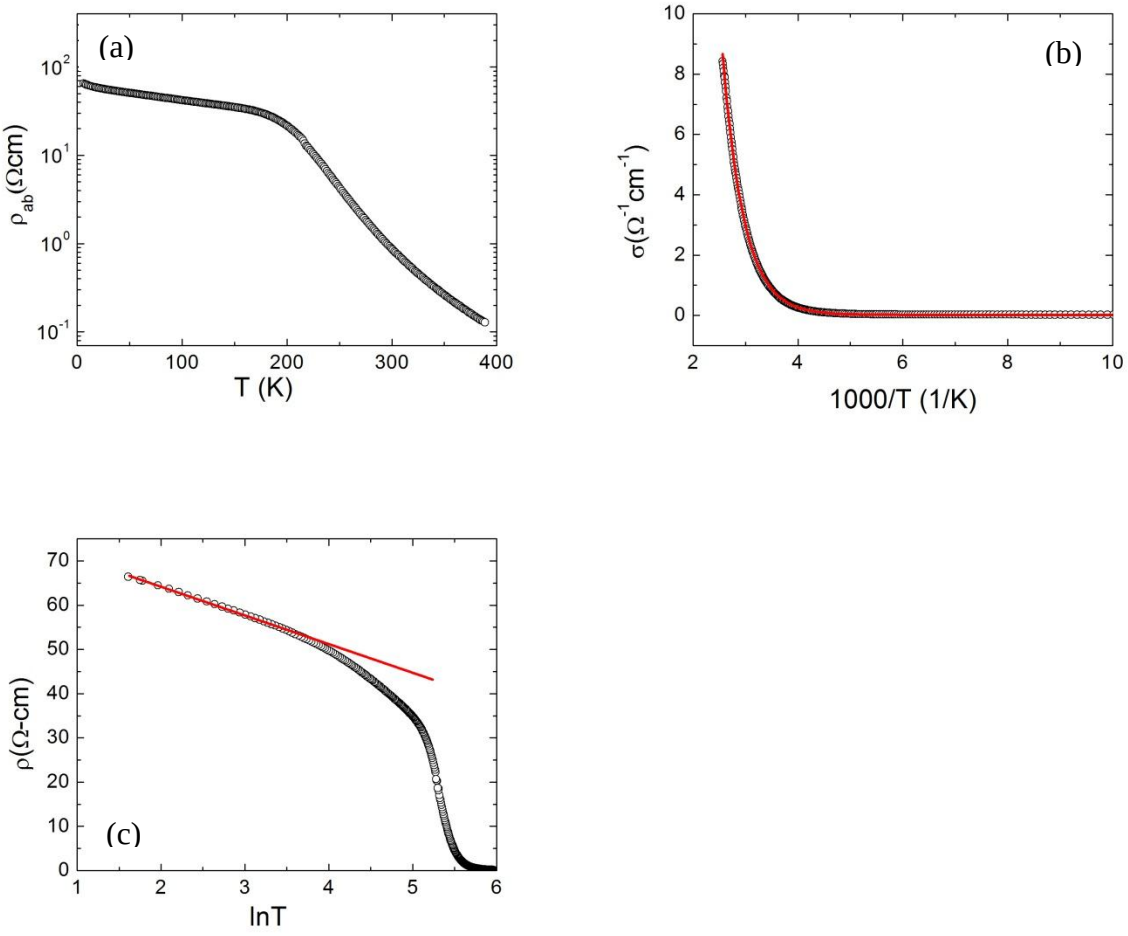

Figure 6-4 (a) Ab plane resistivity of $BaMn_2Sb_2$ measured from 5 K to 390 K. (b) σ versus inverse temperature with fitting in the ranges from 390 K to 100 K. The red solid lines are fitted to $\sigma = \sigma_0 + B\exp(-\Delta/2k_BT)$. (c) At low temperatures, the resistivity is fitted by $\rho = AlnT + B$.

6.3 Magnetic Properties of $BaMn_2Sb_2$ Single Crystal

Small single crystals from the same batch were picked for magnetic susceptibility measurements on a Superconducting Quantum Interference Device (SQUID, by Quantum

Design) from 5 K to 400 K along both the ab plane and the c axis. The temperature dependence of magnetic susceptibility $\chi = M/H$ of $BaMn_2Sb_2$ measured along both the ab plane and the c axis at 1000 Oe is shown in Figure 6-5(a). Along the ab plane, χ increases gradually with decreasing temperature up to 700 K which decreases with a larger slope above 450 K, as shown in the inset. Along c axis χ decreases first and has a minimum at around 150 K, different from previous report (75 K).[97] The minimum at low temperatures can also be observed in the isostructural $BaMn_2P_2$[103] and $BaMn_2Bi_2$.[104] Above this temperature, the magnetic susceptibility increases with temperature. Below the minimum, there is an upturn at very low temperatures.

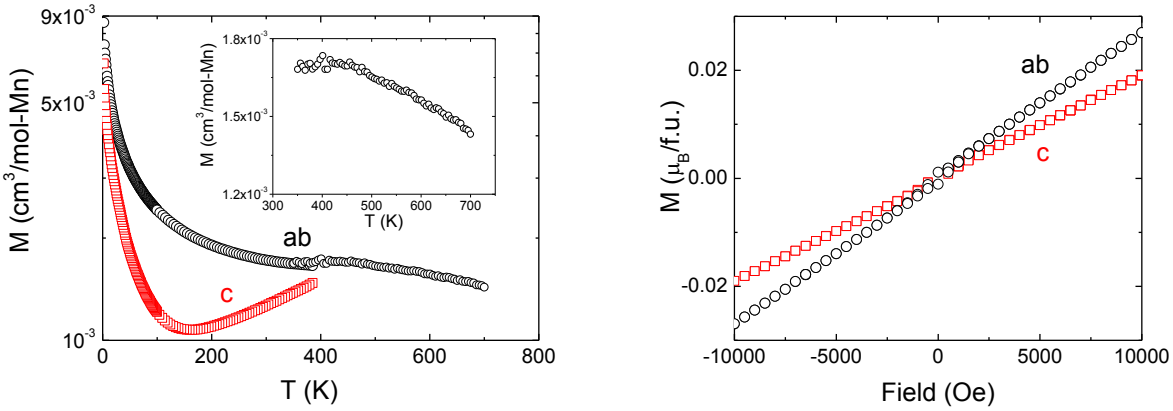

Figure 6-5 (a) Temperature dependence of magnetization M measured at 1000 Oe. Along ab plane, the measurement was done from 2 to 700 K while along c axis the temperature was from 2 K to 400 K. The inset shows the magnetic susceptibility along ab plane from 350 K to 700 K. (b) Magnetization M versus applied magnetic field H isotherm measured at 2 K.

At very low temperatures, the magnetic susceptibility along the ab plane and the c axis crosses. This is quite different from the magnetic susceptibility of $BaMn_2Bi_2$ and $BaMn_2As_2$ along ab plane that is temperature independent below 400K.[116, 117] Moreover, as shown in Figure 6-5(b), the magnetization versus applied field along both the ab plane and the c axis shows linear behavior at 2 K.

6.4 Single Crystal Neutron Scattering Measurement of $BaMn_2Sb_2$

Single crystal neutron diffraction measurements were performed at the HB-3A four-circle diffractometer at the High Flux Isotope Reactor at the Oak Ridge National Laboratory. The incident neutron has wavelength of 1.005 Å. A piece of plate-like (26.2 mg) crystal was used for single crystal structure and magnetic structure determination. The crystal was placed on an Al holder with aluminum foil in an evacuated sample space. The propagation vector is (0, 0, 0). A furnace was installed so that the measurements can be performed in the range from 6 K to 800 K.

The compound $BaMn_2Sb_2$ has a tetragonal structure with the space group I4/mmm (space group 139). Figure 6-6 shows the measurements of nuclear or magnetic reflections of the single crystal at different temperatures. Notice that the intensity profiles are fitted by two Gaussian peaks that correspond to two different single crystal domains in this layered compound. As shown in Figure 6-6(a) and (c), the reflections (1 1 0) and (0 0 2) are nuclear reflections since the intensities remain almost constant over all temperatures. There are also gradual shift of the Gaussian peak to the lower 2θ at higher temperatures, indicating larger lattice parameters due to thermal expansion. In contrast, both (1 0 1) and (3 1 0) reflections have vanishing intensities on warming to high temperatures, indicative of a magnetic phase transition. Note that the intensity of (3 1 0) reflection remains even warming up to 680 K, suggesting a nuclear Bragg peak. In fact, from the temperature dependence of the peak intensities (Figure 6-7(b)) we can observe that the intensity gradually decreases with increasing temperature with a transition at around 443 K. In contrast, at high temperatures, the intensity of reflection (1 0 1) almost vanished above 460 K. Thus magnetic reflection is dominant associated with the (1 0 1) Bragg peak.

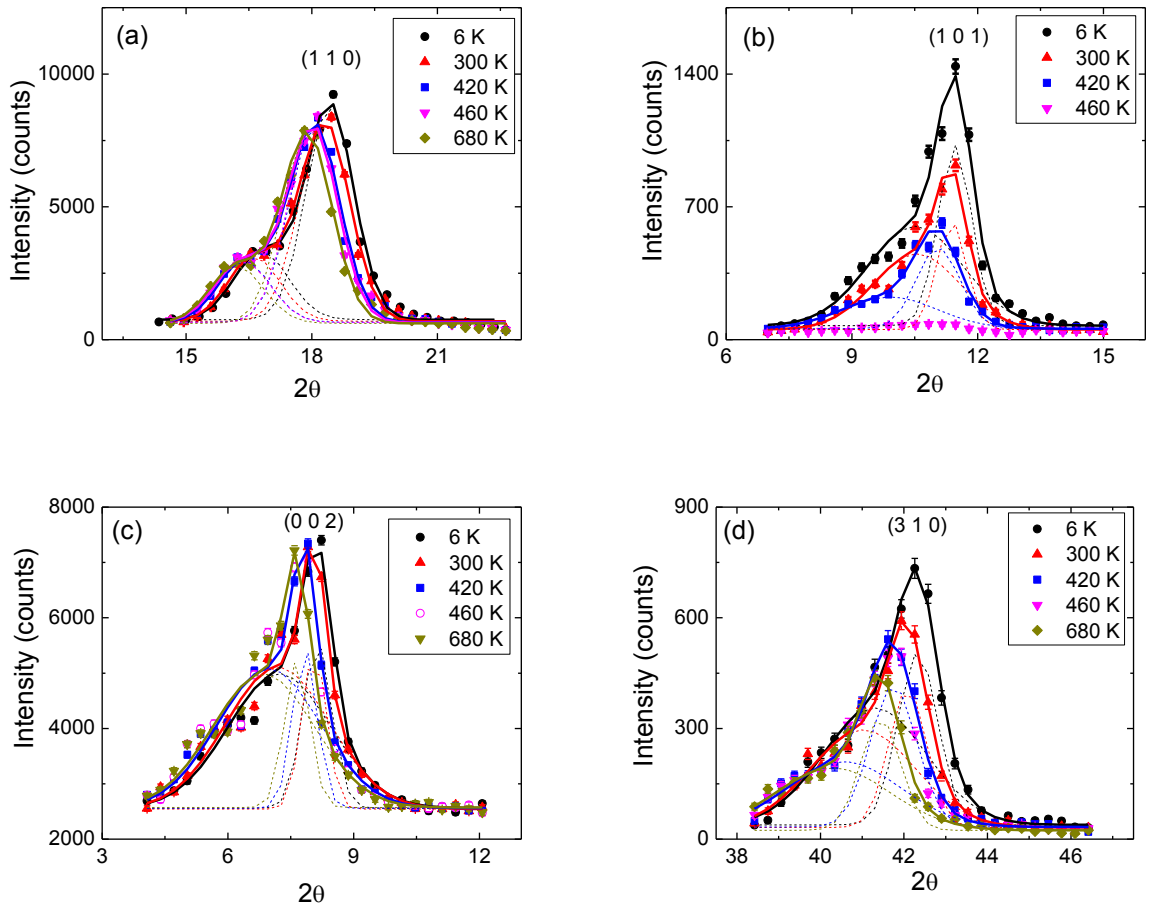

Figure 6-6 Measurements of the (a) (1 1 0), (b) (1 0 1), (c) (0 0 2) and (d) (3 1 0) reflections at different temperatures. The peaks are fitted by the sum of two Gaussian peaks that correspond to two possible single crystal domains.

The magnetic order parameter was measured from 6 K to 760 K, as shown in Figure 6-7(b). The temperature dependence suggests that the magnetic transition is second order in nature. By fitting the data above 350 K using a power law $\mu(T)=\mu_0(1-T/T_N)^{\beta}$, we can obtain the fitting parameters T_N=443.3(2)K and β=0.68(1), close the value for 3D Heisenberg antiferromagnetic model. This value agrees with the trend that $BaMn_2Pn_2$ has lower T_N with heavier pnictides ($BaMn_2P_2$: T_N =750 K, $BaMn_2As_2$: T_N =625 K, $BaMn_2Bi_2$: T_N =400 K).[103, 105, 107]

A set of nuclear and magnetic reflections were measured at T = 6 K by ω scans. The integrated intensities were corrected by Lorentz factor. Then the refinement was performed by Rietveld method using the FULLPROF package with common profile parameters for both nuclear and magnetic structures. The refined crystal structure is shown in Table 6-1. Magnetic representation analysis is performed to choose appropriate basis vectors to describe the magnetic spin structures.

Table 6-1 Crystal structures of $BaMn_2Sb_2$ with the space group I4/*mmm* (no. 139) at 6K determined by single crystal neutron scattering at HB-3A. The lattice parameters are a = b = 4.393(7) Å and c = 13.84(3) Å. RF2 = 8.70, RF2w = 9.94, R_F = 4.98, χ^2 = 1.27.

atom	site	x	y	z	U_{iso} (Å^2)
Ba	2a	0	0	0	0.242(150)
Mn	4d	0	1/2	1/4	0.423(104)
Sb	4e	0	0	0.36643(37)	0.283(96)

The determined magnetic structure by Rietveld refinements in the crystallography ($ThCr_2Si_2$ type) has easy axis along the c axis. Four Mn atoms (0 1/2 1/4), (1/2 0 3/4), (1/2 0 1/4) and (0 1/2 3/4) in the unit cell are aligned antiferromagnetically, as shown in Figure 6-7(a), forming a G type antiferromagnet. This refinement result is similar to the magnetic structure of $BaMn_2As_2$, however, different from the ab plane checkerboard type model predicted.[97, 105] From the refinement, we obtained the ordered moment at T=6 K is μ=3.83(3) μ_B, lower than the high-spin (S=5/2) state Mn^{2+} ($3d^5$) value of 5.0 μ_B, where μ_B is the Bohr magneton, g=2.0 in the expression $\mu=gS\mu_B$.

$BaMn_2As_2$ and $BaMn_2P_2$ are another two isostructural compounds with identical magnetic structure. They have similar values, e.g., $BaMn_2As_2$ has ordered moment μ=3.88(4) μ_B/Mn at T=10 K and the value for $BaMn_2P_2$ is μ=4.2(1) μ_B/Mn. The main reason for this moment reduction was suggested to be the Mn d-Sb p hybridization that the Mn d electron count becomes closer to Mn^{1+} ($3d^6$) rather than Mn^{2+}.[63] On the other hand, in the AFe_2As_2 the values were found to be 0.2 – 1.0 μ_B/Fe which is attributed to the itinerant nature of magnetism.[118] The antiferromagnetic structure was a "stripe structure" where the nearest-neighbor (NN) Fe spins are parallel along one basal-plane axis while antiparallel along the other.

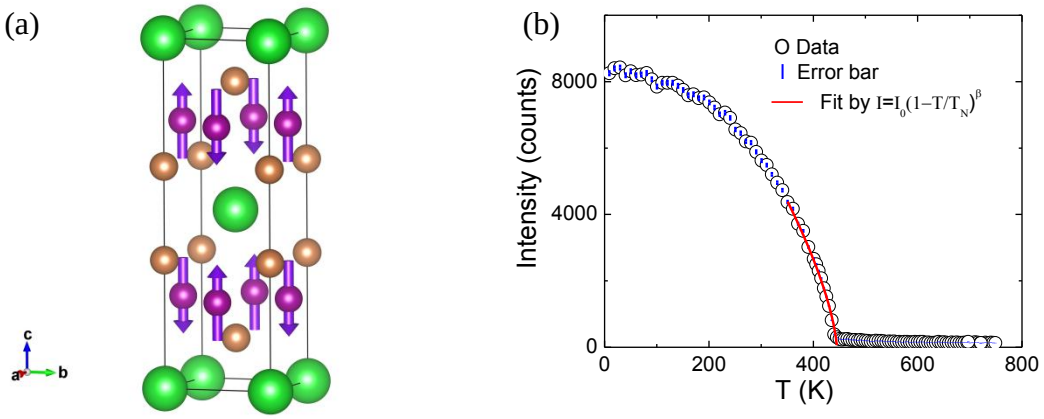

Figure 6-7 (a) Magnetic structure of $BaMn_2Sb_2$ obtained by refinement using FULLPROF package. (b) The temperature dependence of order parameter from 6 K to 760 K. The red solid line is the fitting of $\mu(T)=\mu_0(1-T/T_N)^{\beta}$.

Between two sublattice of this structure are next-nearest-neighbor (NNN) interactions.[119] Within a local moment Heisenberg interaction model, the G-type magnetic structure in AFe_2As_2 compounds can be stabilized if the fourfold AF (NNN) interactions J_2 are dominant over the AF (NN) interactions J_1, in other words, $J_2 \geq J_1/2$.[120] In contrast, as shown in Figure 6-7(a), the Mn spins in $BaMn_2Sb_2$ are collinearly aligned along the c axis antiferromagnetically. The observed

G-type magnetic structure can have NN interactions only, without NNN interaction that are dominant in FeAs-based compounds. This phenomenon has been observed in $BaMn_2As_2$.[105]

Figure 6-8 shows the temperature dependence of heat capacity for $BaMn_2Sb_2$. There is no anomany up to 300 K, indicating no phase transition from 2 K up to 300 K. The heat capacity at about 300 K is 127 J/mol-K, which is close to the classical Dulong Petit heat capacity value given by C=3nR ~ 125 J/mol-K, where n is the number of atoms per formula and R is the molar gas constant.

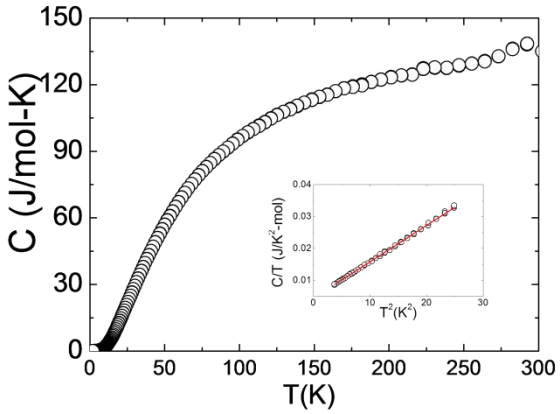

Figure 6-8 The temperature dependence of heat capacity for $BaMn_2Sb_2$ from 2 K to 300 K. Inset shows C(T)/T versus T^2 data below 5 K and linear fit by the expression $C/T=\beta T^2$.

The obtained heat capacity is quite similar to that of $BaMn_2As_2$[117] and $BaMn_2Bi_2$.[107] From the linear fit of C(T)/T versus T^2 by expression $C/T = \beta T^2$, the lattice constributions to the heat capacity were estimated to be β=0.0011(1) J/K^{4}mol. Assume the βT^2 term arises only from the lattice heat capacity, we can estimate the Debye temperature from the obtained β value above using the expression $\Theta_D = (\frac{12\pi^4 Rn}{5\beta})^{1/3}$, where n is the number of atoms per formular (n=5 for $BaMn_2Sb_2$)[121]. θ_D = 207K was obtained for $BaMn_2Sb_2$. Note that, $BaMn_2Sb_2$ is

antiferromagntically orderred at low temperatures, thus the excitations of antiferromagnetic spin waves my also contribute to β.[122]

To summarize, $BaMn_2Sb_2$ crystallizes in the tetragonal $ThCr_2Si_2$-type structure with lattice parameters. The magnetization versus temperature and field reveals that there is no long range ordering in the compound. Indeed, neutron scattering measurement suggests that $BaMn_2Sb_2$ is a G-type antiferromagnet with easy axis along c axis. The Mn atoms have ordered moment $\mu=4.0(5)\mu_B$ at T = 6K. Within a local moment picture, NN interactions in $BaMn_2Sb_2$ are dominant whereas NNN interactions are dominant in the tetragonal phase of the AFe_2As_2 compounds. Moreover, the magnetic transition is second-order in nature without structural distortion, as confirmed by both neutron scattering along (008) scan and specific measurement. The linear fitting of C(T)/T versus T^2 from 2K to 5K gives $\beta=0.0011(1)$ J/K^4mol. Debye temperature estimated from β is θ_D = 207 K. The small Sommerfeld coefficient implies finite density of states as the temperature approaches zero, corresponding to the logrithmic temperature dependence of electrical resistivity at very low temperatures. At higher temperatures, the behavior of electrical resistivity agrees with semiconducting with a small band gap. The change of sign of Seebeck coefficient indicates the change of dominate carrier type. Thermal conductivity increases with decreasing temperature and have a phonon peak at around 60 K.

Chapter 7 Magnetic, Electrical and Thermal Transport of $Ba_2Mn_3Sb_2O_2$ Single Crystal

Recently, new types of compounds were proposed that they might serve as a parent compounds for high-T_c superconductivity. [123, 124] This type of structure contains two different types of layers. One layer is similar to the CuO_2 layers in the high-T_c cuprate that oxygen atoms are located between the nearest neighbor Cu atoms. The primary bonding is Cu-O and a large component of O 2p contributes to the states at Fermi level. The other layer is isostructural to the FeAs layer in the iron pnictide superconductors. As atoms are arranged at either side of Fe square lattice and form tetrahedral coordination with Fe atom at center. The states at Fermi level are dominated by Fe d orbitals due to strong direct Fe-Fe interactions. Cuprate and iron pnictides have been widely studied for their high-T_c superconductivity.[125-132] In these superconductors, superconductivity always appears near static antiferromagnetic (AF) order, suggesting interplay between the magnetism and superconductivity.

$Sr_2Mn_3As_2O_2$ has two inequivalent Mn sites. The schematic crystal structure is shown in Figure 7.1. In the MnO_2 layer, Mn(1) are fourfold coordinated by O ab plane. In contrast, the Mn(2) are fourfold coordinated by As in the MnAs-type layer. Sr atoms act as spacer that separate these two sublattice. Neutron experiments on $Sr_2Mn_3Pn_2O_2$ (Pn = As, Sb) confirmed that there are two distinct magnetic sublattices, Mn(1) and Mn(2).[133] At high temperatures, Mn(2) moments undergo long range G-type antiferromagnetic ordering at Neel temperatures 340 K (As) and 300 K (Sb), observed in neutron scattering experiment with magnetic propagation vector k = (0, 0, 0). The ordered moment is 3.4 μ_B/Mn(2) at 4 K. At low temperatures, Mn(1) moments in $Sr_2Mn_3Sb_2O_2$ order below 65 K with k = (1/2, 1/2, 0) along <100> with ordered moment is of 4.2 μ_B whereas the Mn(1) sublattice in $Sr_2Mn_3As_2O_2$ shows very weak reflections below 75 K.[133]

Hence the replacement of Sb element instead of As affect both Mn sublattices: Neel temperature of the AF ordering in Mn(2) sublattice; long range ordering establishes at low temperatures at 65 K in Mn(1) sublattice. The temperature dependence of magnetization of $Sr_2Mn_3Sb_2O_2$ shows only a broaden maximum at 79 K, without any feature of high temperature AF ordering.[134] There have been the same trend observed in $Ba_2Mn_3Pn_2O_2$ (Pn = P, As, Sb).[134] Though no features about the high temperature ordering have been observed, the broaden maximum position moves to the lower temperatures with heavier pnictide atoms.[134, 135] Moreover, the replacement of spacer Sr atoms by Ba also affect the magnetic properties, revealed by magnetization measurement. The Neel temperature for $Ba_2Mn_3Sb_2O_2$ was deduced as 44 K.[134] The magnetism for the compound cannot be determined by the magnetic susceptibility alone.

Herein, we report the neutron scattering measurement of the $Ba_2Mn_3Sb_2O_2$ to determine the magnetic structure that if the two distinct Mn magnetic sublattices exist. We will describe obtained magnetic structure model and the temperature dependence of the magnetism. We will also report the characterizations of the compound, such as magnetic susceptibility, electrical resistivity, Seebeck coefficient and thermal conductivity.

7.1 Synthesis and Structure of $Ba_2Mn_3Sb_2O_2$

Single crystals of $Ba_2Mn_3Sb_2O_2$ were prepared by a Sn flux method. (The BaO, Mn powder (99.95% pure, Alfa-Aesar), Sb (99.995%, Alfa Aesar) were Sn powder (Alfa Aesar, 99.995%) were taken in the ratio of (2:3:2:5) and placed in high alumina crucible. Then the crucible was sealed in evacuated quartz tube. The whole assembly was first sintered at 1100 ℃ for 15 h and then slowly cooled down (5℃/h) to 700℃. At this temperature, the sealed quartz tube was taken out from the furnace, spun in a centrifuge immediately and quenched to room

temperature.) Sn flux was well separated. High yield of plate-like single crystals with surfaces over 5 mm ×5 mm were obtained which are very malleable and easily bent.

The crystal structure of $Ba_2Mn_3Sb_2O_2$ is shown in Figure 7-1(a). Two different Mn sites are also labeled. The Mn(1) is in Mn-O type layer while Mn(2) is located in MnSb type layer.

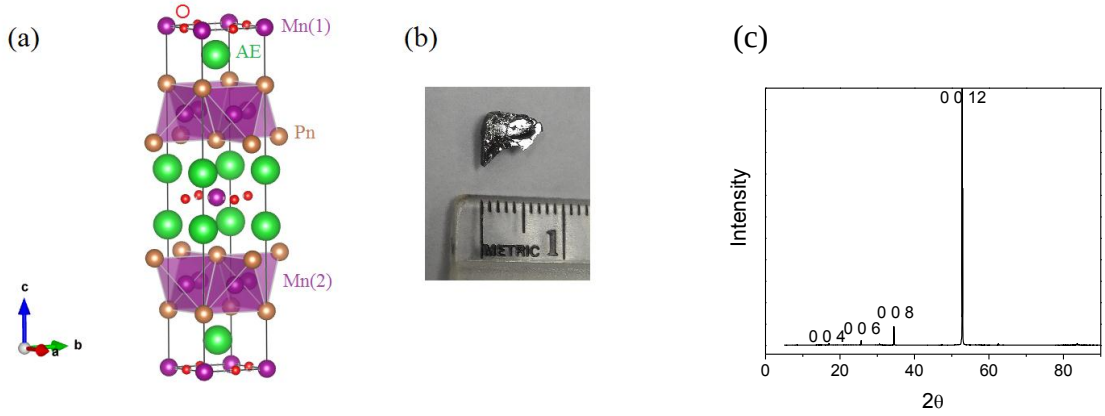

Figure 7-1 (a) Schematic picture of the crystal structure of the $AE_2Mn_3Pn_2O_2$ (AE =Ba, Sr, Pn = As, Sb) compound. (b) Grown crystal of $Ba_2Mn_3Sb_2O_2$. (c) XRD result of plate-like single crystal. The peaks are labeled with c axis diffractions of $Ba_2Mn_3Sb_2O_2$.

The compositions were checked using wavelength dispersive spectroscopy (WDS) on cleaved surfaces of the crystals. The average elemental ratio was found to be Ba: Mn: Sb: O = 2: 2.85 : 1.98 :1.89 which is close to stoichiometry for the $Ba_2Mn_3Sb_2O_2$ compound. The XRD result of a piece of single crystal exhibit very strong diffractions from c axis, as shown in Figure 7-1(b).

7.2 Thermoelectric Properties of $Ba_2Mn_3Sb_2O_2$ Single Crystal

Electrical resistivity was measured via the four-probe method on a piece of single crystal (~1mm ×2mm ×0.6mm). Thin layers of Au were deposited on the surface to improve the electrical contact between sample surface and leads. Big crystals were cut into rectangular shape

(~2mm ×6mm ×0.6mm) for ab plane thermoelectric property (Seebeck coefficient S and thermal conductivity κ) measurements. Electrical resistivity measurements were performed separately to avoid the effect of Joule heating during the thermal transport measurements.

Figure 7-2 shows the temperature dependence of electrical resistivity for the compound $Ba_2Mn_3Sb_2O_2$. With decreasing temperature, the electrical resistivity first increases, then reaches a broad maximum at around 260 K. After that, the electrical resistivity decreases with decreasing temperature and shows a minimum at around 7 K with a residual resistivity of about 33.69 mΩ cm. As the temperature approaching zero, the electrical resistivity increases, suggesting the compound has an insulating rather than a metallic ground state. This is similar to the compound with FeAs type layer occupied by Mn, such as $BaMn_2As_2$, $BaMn_2Sb_2$ with small band gaps.[117] On the other hand, similar metallic behavior of electrical resistivity at high temperatures was observed in compound $Sr_2Mn_2CuAs_2O_2$ where the MnAs layer was partially replaced by Cu.[133] Based on the fact that the $BaMn_2As_2$ with Mn-occupied FeAs type layer has insulating background while the compound $BaCu_2As_2$ with Cu-occupied FeAs type layer shows metallic behavior, the presence of Cu in FeAs layer could introduce metallic ground state.[136] However, in the compound $Ba_2Mn_3Sb_2O_2$, the mechanism may be different. The conductivity of a semiconductor is determined by the carrier concentration (holes and electrons) and carrier mobility. The temperature dependence of carrier mobility for holes and electrons could be different and so is the temperature dependence of carrier concentration.[137] Moreover, the reason for negative coefficient at high temperatures is unknown. Similar behavior was observed in $Sr_2Mn_2CuAs_2O_2$ which was attributed to the possible high-resistivity impurity in the grain boundaries. However, the sample in our measurement is a piece of single crystal, indicating the negative coefficient behavior at high temperatures could be intrinsic.

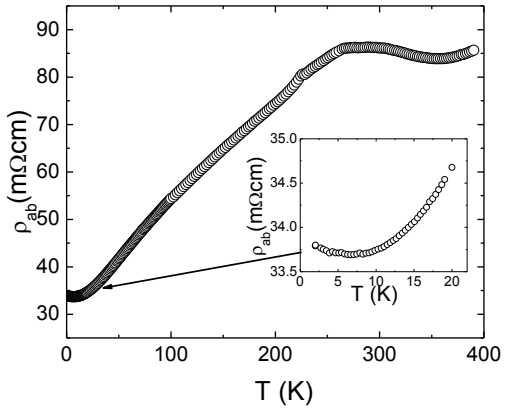

Figure 7-2 The electrical resistivity measurement of $Ba_2Mn_3Sb_2O_2$ from 2 K to 390 K. The inset is the enlarged picture from 2 K to 20 K.

As shown in Figure 7-3(a), the ab plane Seebeck coefficient was measured from 2 K to 390 K. The measurement was performed for both cooling process and warming process and there is no visible difference between them. As temperature increases, the Seebeck coefficient increases first and then decreases with a peak-like shape at around 65 K. The value changes from positive to negative at around 175 K and reaches a negative minimum at about 250 K. At higher temperatures, the Seebeck coefficient increases with increasing temperature up to 390 K. Interestingly, the overall Seebeck coefficient versus temperature curve is quite similar to that of $BaMn_2Sb_2$, though negative Seebeck coefficient range for $BaMn_2Sb_2$ is much larger. This change of Seebeck coefficient sign from negative to positive implies that the charge carriers change from electron-dominant to hole-dominant. When both hole and electron contribute to the transport, the total Seebeck coefficient can be represented by the Mott relation: $S = \frac{S_n\sigma_n + S_p\sigma_p}{\sigma_n + \sigma_p}$, where $S_{n,p}$, $\sigma_{n,p}$ are the Seebeck coefficient and electrical conductivity for n-type and p-type carriers, respectively. Since S_n and S_p have opposite signs, the magnitude of total Seebeck coefficient is reasonably small at low temperatures. For our compound $Ba_2Mn_3Sb_2O_2$, the magnitude of the Seebeck

coefficient in the whole measurement temperature range is less than 5 μV/K. The thermal conductivity was measured simultaneously. The thermal conductivity gradually decreases with decreasing temperature with a sudden drop at 20K.

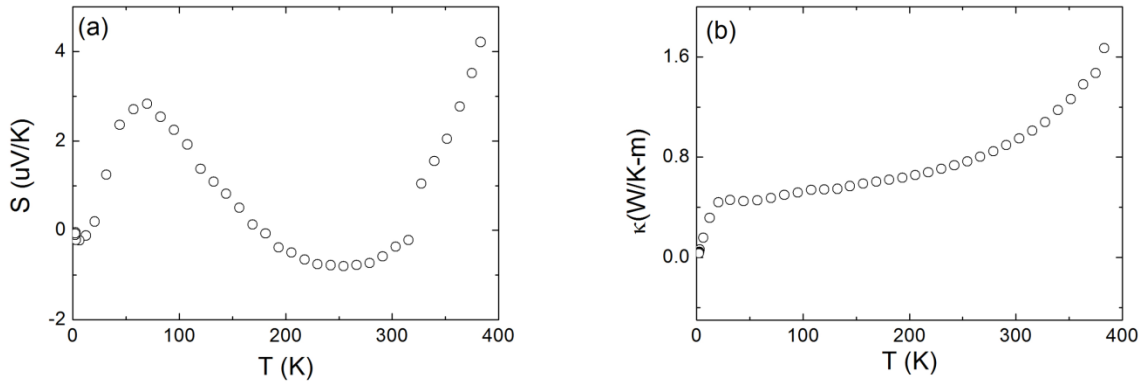

Figure 7-3 (a) Seebeck coefficient and (b) thermal conductivity measurement of the $Ba_2Mn_3Sb_2O_2$ crystal from 390 K to 2 K.

7.3 Magnetic Properties of $Ba_2Mn_3Sb_2O_2$ Single Crystal

Figure 7-4(a) shows the temperature dependence of magnetic susceptibility (χ=M/H) measurement along the ab plane and the c axis. The measurement was performed at 1000 Oe for both ZFC and FC cooling process. There is no visible difference between the ZFC and FC curve that was observed in isostructural $Sr_2Zn_2MnAs_2O_2$ or $Sr_2Mn_3As_2O_2$.[133]

As shown in Figure 7-4(b), the magnetization versus field shows a linear dependence. It also suggests the absence of the possible impurity of MnSb which is ferromagnetic with Tc above 300 K.[138] On the other hand, the magnetic susceptibility increases with decreasing and shows a broad peak at around 67 K. This is consistent with the previous result reported.[134, 135] This broad maximum often indicates low dimensional antiferromagnetic coupling. [139]

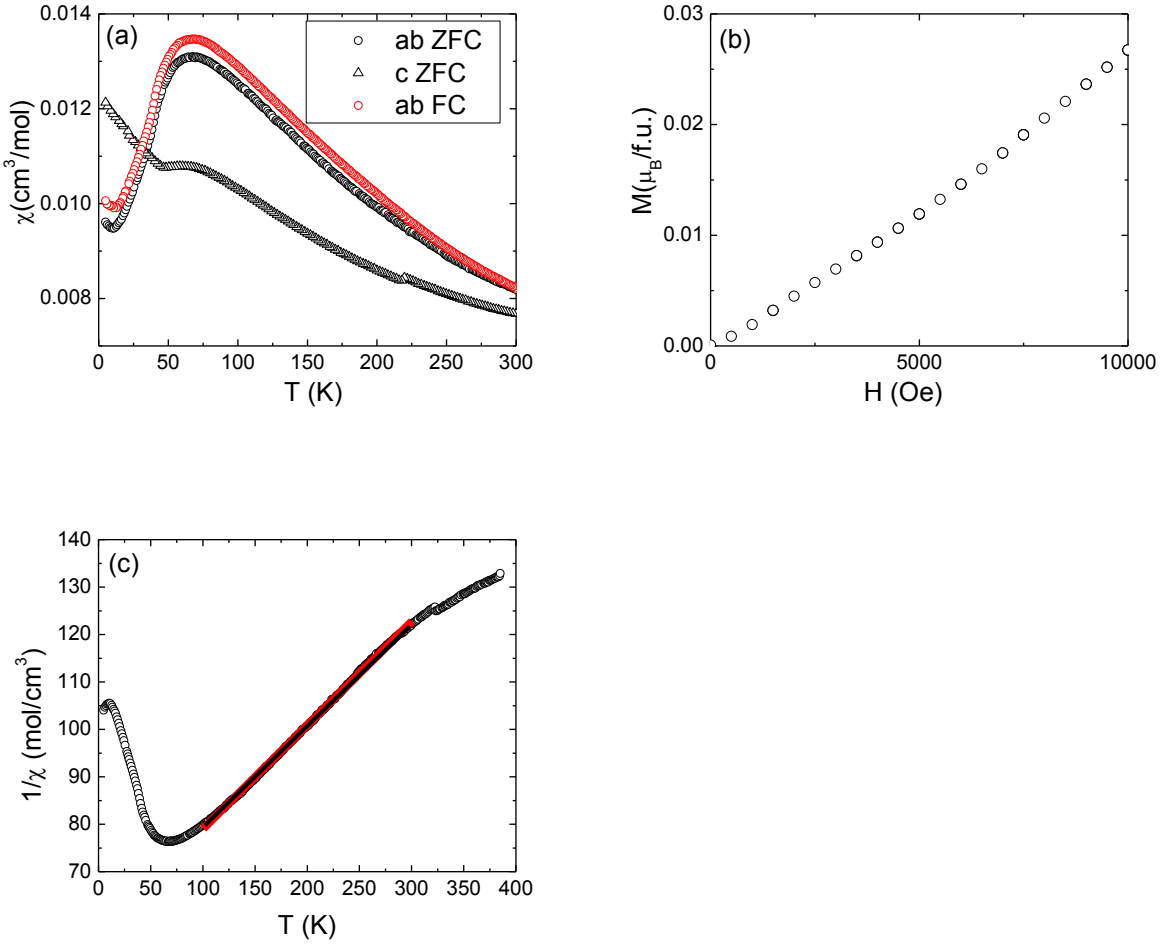

Figure 7-4 (a) Magnetic susceptibility measurement of the $Ba_2Mn_3Sb_2O_2$ crystal. (b) The magnetization versus field along ab plane. (c) $1/\chi$ versus temperature. The fitting from 100 K to 300 K gives $1/\chi=57.17(7) + 0.2184(3)T$.

For the paramagnetic state, we can fit the magnetic susceptibility by Curie-Weiss expression $\chi = \chi_0 + C/(T-\theta)$, where χ_0 is the temperature independent term, C is the Curie constant $C = N_A\mu_{eff}^2/(3k_B)$ and θ is the Weiss temperature, where N_A is the Avogadro's number, μ_{eff} is the effective magnetic moment per formula unit, and k_B is Boltzmann's constant. The χ_0 includes both diamagnetic moments from ions or diamagnetic conduction electron Landau orbital susceptibility and paramagnetic contributions, such as Van Vleck paramagnetism, paramagnetic conduction electron Pauli spin susceptibility, yielding a net small and often negligible value. By setting $\chi_0 = 0$ for fitting, as shown in Figure 7-4(c), we obtain C = 4.59

cm^3K/mol, and θ = -262 K. The negative Weiss temperature indicates antiferromagnetism at low temperatures. As mentioned, the Mn spins are antiferromagnetically ordered in MnSb layer in this temperature range, only the Mn in MnO layer contribute to the paramagnetism. Our value 6.08 μ_B/f.u. is very close to the value of one Mn atoms per formula 5.92 μ_B with $\mu = g\sqrt{S(S+1)}\mu_B$where S=5/2, g = 2.

7.4 Neutron Scattering Measurement of $Ba_2Mn_3Sb_2O_2$ Single Crystal

Single crystal neutron diffraction measurements were performed at the HB-3A four-circle diffractometer at the High Flux Isotope Reactor at the Oak Ridge National Laboratory. The incident neutron has wavelength of 1.546 Å. A piece of plate-like (11.2 mg) crystal was used for single crystal structure and magnetic structure determination. The crystal was placed on an Al holder with strain-free mounting using UHV grease in an evacuated sample space. Two propagation vectors (0, 0, 0) and (1/2, 1/2, 0) were used at 6 K and 100 K to search the possible two distinct magnetic sublattice. Order parameter measurements along (101) with propagation vector (0, 0, 0) were performed in the range from 6 K to 350 K with both warming and cooling process. With the other propagation vector (0.5, 0.5, 0), the magnetic order parameter was measured from 6 K to 100 K.

As shown in Figure 7-5(a), the intensity of the reflection (1 0 1) with propagation vector (0, 0, 0) is almost the same at 6 K and 100 K, then drops at 350 K, indicating a magnetic transition in this temperature range. Note that intensity at 350 K still remains. From Figure 7-5(b), the temperature dependence of the magnetic order parameter suggests a second order transition at 313.9(1) K, obtained by the fitting $I = I_0(T - T_N)^{\beta}$. The fitting parameter β is about 0.329(3), which is much smaller than the 3D antiferromagnetic Heisenberg model. The decreasing with increasing temperature above T_N implies there is also a nuclear reflection

contribution, though the magnetic reflection is dominant, as depicted in Figure 7-5(a). Similarly, there are both magnetic and nuclear reflections in (1 0 3) and (1 0 5), as shown in Figure 7-5(c) and (d). At 350 K, the intensities both remain relatively large values. Moreover, a shift of peak center towards smaller angle can also be observed compared to that at 6 K, exhibiting the thermal expansion effect.

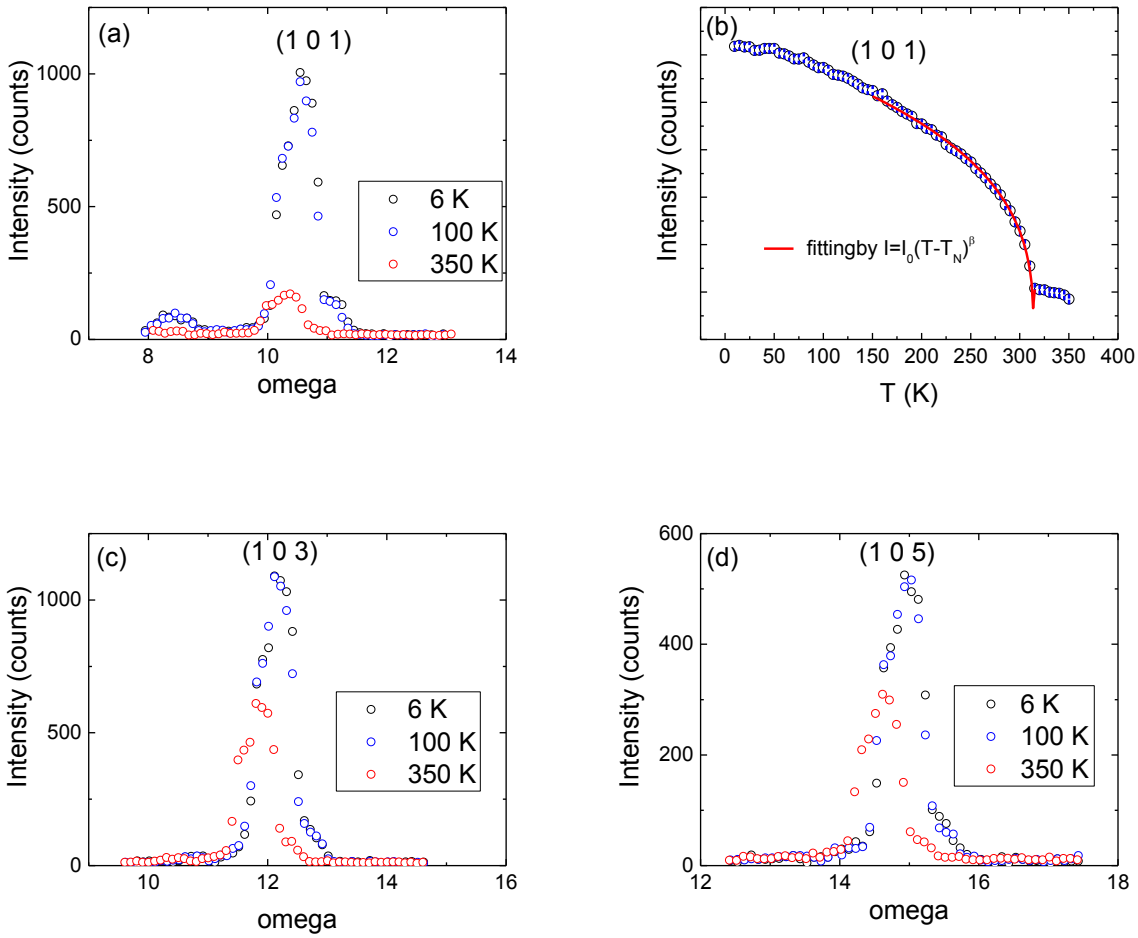

Figure 7-5 (a)(c)(d) Measurement of (1 0 1) (1 0 3) (1 0 5) reflections at 6 K, 100 K and 350 K with the magnetic propagation vector (0, 0, 0). (b) Magnetic order parameter for (1 0 1), fitted by $I = I_0(T - T_N)^{\beta}$.

As indicated by magnetic susceptibility measurement, there may be a new magnetic ordering below 67 K. By choosing magnetic propagation vector (0.5, 0.5, 0), a new set of

magnetic reflections were obtained. As shown in Figure 7-6(a) (b) (c), there are magnetic reflections (1 0 1) (1 0 3) (1 0 5) at 6 K while the intensities almost vanish at 100 K. The magnetic order parameter measurement suggests there is a magnetic transition at 40(1) K. The fitting parameter is 0.46(4) which is larger than the value for propagation vector (0, 0, 0) but also smaller than the 3D antiferromagnetic Heisenberg model.

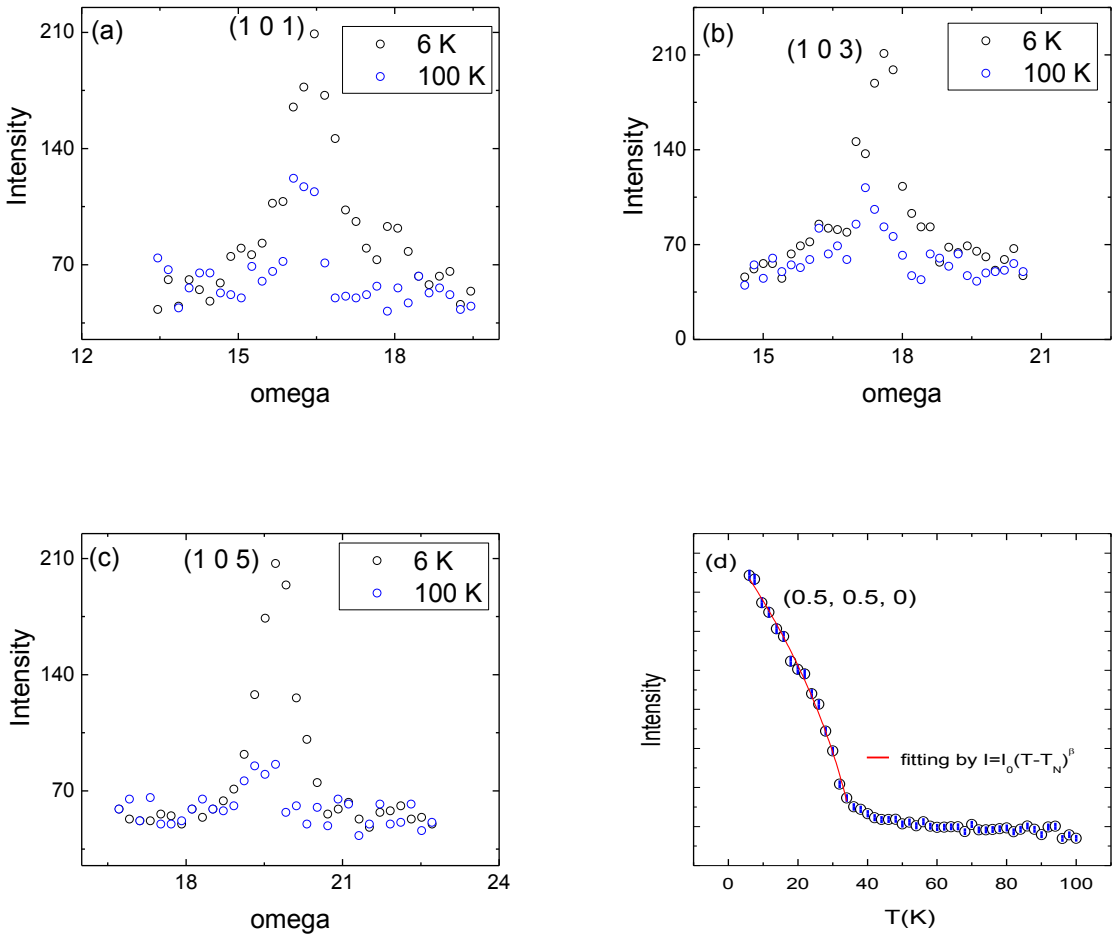

Figure 7-6 (a)(b)(c) Magnetic reflections for (1 0 1), (1 0 3) and (1 0 5) with magnetic propagation vector (0.5, 0.5, 0) at 6 K and 100 K, respectively. (d) Magnetic order parameter for (0.5, 0.5, 0) with propagation vector (0.5, 0.5, 0).

The magnetic structure of $Ba_2Mn_3Sb_2O_2$ can be further revealed by the refinement of the diffraction data at 100 K and 6 K. The refinement result shows that $Ba_2Mn_3Sb_2O_2$ crystallize in

tetragonal space group I4/mmm with lattice parameters a = b = 4.367 Å and c = 20.78 Å, as shown in Table 7-2.

Table 7-2 Crystal structures of $Ba_2Mn_3Sb_2O_2$ with the space group I4/*mmm* (no. 139) at 100 K determined by single crystal neutron scattering at HB-3A. The lattice parameters are a = b = 4.367 Å and c = 20.78. Å. RF = 5.98. χ^2 = 3.98.

atom	x	y	z	U_{iso} (Å^2)
Ba	0	0	0.41788(25)	0.56(24)
Mn1	0	0	0	1.59(0.35)
Mn2	0	1/2	1/4	0.45(0.28)
Sb	0	0	0.16878(21)	0.52(21)
O	0	1/2	0	0.82(19)

Figure 7-7 shows the magnetic structures of $Ba_2Mn_3Sb_2O_2$ with two Mn sublattice. In Mn(2) sublattice, moments of Mn atoms have easy axis along c axis. Each of Mn atoms is antiferromagnetically orderred with its nearest neighbours, exhibiting G-type AFM. The moment obtained from refinement is 3.43(11) μ_B at 6 K. On the other hand, easy axis of Mn(1) moments is along ab plane which is perpendicular to that of Mn(2) moments. In each layer of Mn(1) sublattice, the moment of Mn atom is antiparallel to those of its four nearest neighbors. The obtained effective moment for Mn(1) is 3.55(5) μ_B, close to that of Mn(2). Hence, $Ba_2Mn_3Sb_2O_2$ has two Mn sublattice with similar magnitude of magnetic moments but in perpendicular directions. Moreover, a broad magnetic peak (0.5, 0.5, 0) suggest that the magnetic correlations of Mn(1) could be short range. This is consistent with the previous result that β may imply two dimensional magnetic correlations.

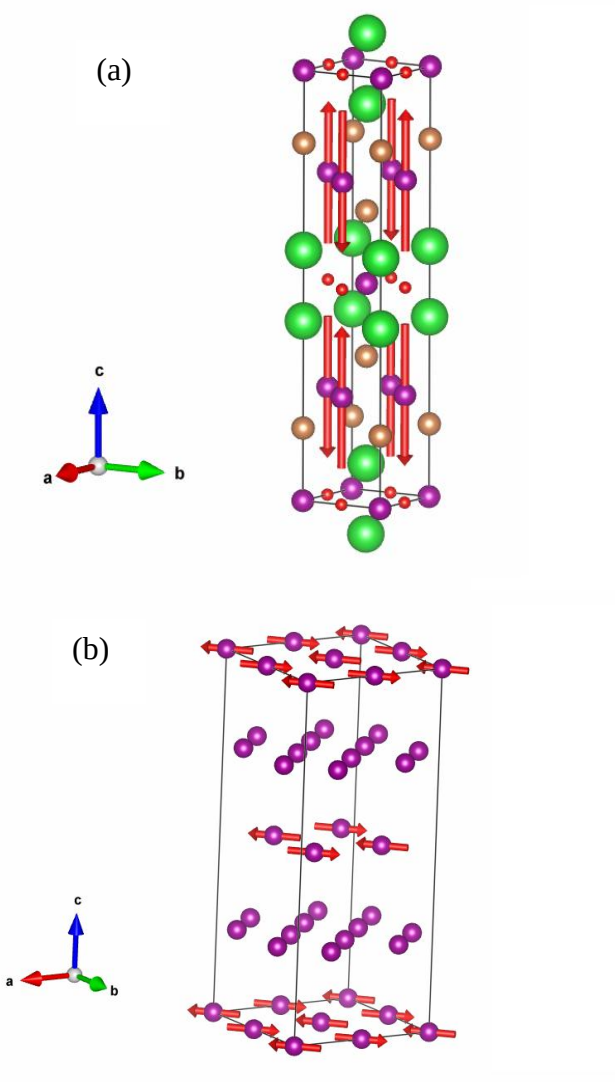

Figure 7-7 Demonstration of determined magnetic structure of (a) Mn(2) sublattice and (b) Mn(1) sublattice.

In summary, $Ba_2Mn_3Sb_2O_2$ is a layered compound which has MnO layer and MnSb layer alternatively stacking along the c axis, separated by Ba layer. The Mn atoms at two different types of layer form two independent sublattice: Mn (1) in MnO layer is in magnetic order below 40 K while Mn(2) in MnSb layer exhibits G type antiferromagnetism with T_N = 314 K. The magnetic susceptility shows no anomaly around 314 K but a broad maximum at about 67 K. Fitting to Curie-Weiss law, we obtain Weiss temperature θ = - 262 K, correspoinding to

antiferromagnetism. Electrical resistivity of the compound shows metallic behavior. The Seebeck coefficient also has negative to positive transition at low temperatures. The magnitude of Seebeck coefficient is less than 5 μV/K from 5 K to 390 K. Thermal conductivity of the compound increases with increasing temperature.

Chapter 8 Summary

Work for this dissertation sheds light on understanding the physical properties of a couple of layered transition metal compounds, including studies on thermoelectric, electrical and magnetic properties. High quality of single crystals of $Bi_2Sr_2Co_2O_9$, $Sr_3(Ru_{1-x}Mn_x)_2O_7$, $PdCoO_2$, $BaMn_2Sb_2$ and $Ba_2Mn_3Sb_2O_2$ are grown by either floating zone method or flux method.

The thermoelectric properties of single crystal and thin film $Bi_2Sr_2Co_2O_9$ are investigated. Although all films display non-metallic behavior, the high Seebeck coefficient and low thermal conductivity and metallic conduction seen in single crystals strongly suggest that it is possible to improve the thermoelectric performance when prepared in optimal condition.

The electrical resistivity $PdCoO_2$ shows metallic behavior with small magnitudes, only a few μΩ cm at room temperature. Strong anisotropy was observed between ab plane and c axis. At low temperatures, the resistivity has both electron-electron scattering and electron phonon coupling terms. At high temperatures, the resistivity shows linear temperature dependence, due to electron phonon coupling.

The layered perovskite $Sr_3(Ru_{1-x}Mn_x)_2O_7$ was investigated for x = 0.025, 0.06 and 0.16. By Mn doping, a metal-insulator transition occurs with higher transition temperature at higher doping levels. The electrical resistivity remains low at room temperature. On the other hand, the Seebeck coefficient is enhanced by Mn doping, which can be attributed to the increased density of states due to narrowing of bandwidth. The thermal conductivity has almost the same value for crystal with different doping levels.

$BaMn_2Sb_2$ crystallizes in the tetragonal $ThCr_2Si_2$ type structure, isostructural to the parent compound of Fe based superconductor $BaFe_2As_2$. However, there is no structural transition in

this compound. Single crystal Neutron scattering suggest G type antiferromagnetism with T_N = 443 K. There is no anomaly observed in specific heat measurement. The linear fitting of C(T)/T versus T^2 from 2K to 5K gives Sommerfeld coefficient γ=0.0064(1) J/K^2mol, β=0.0011(1) J/K^4mol. Debye temperature estimated from β is θ_D = 207 K. At higher temperatures, the behavior of electrical resistivity agrees with semiconducting with a small band gap. The change of sign of Seebeck coefficient indicates the change of dominate carrier type. Thermal conductivity increases with decreasing temperature and have a phonon peak at around 60 K.

$Ba_2Mn_3Sb_2O_2$ is another layered compound which has Cu-O type MnO layer and FeAs type MnSb layer alternative stacking along c axis, separated by Ba layer. The Mn atoms at two different type layers form two independent sublattice: Mn (1) in MnO layer is in magnetic order below 40 K while Mn(2) in MnSb layer exhibits G type antiferromagnetism with T_N = 314 K. The magnetic susceptility shows no anomaly around 314 K but a broad maximum at about 67 K. By Curie-Weiss law, the fitting gives Weiss temperature θ = -262 K, correspoinding to antiferromagnetism. The electrical resistivity measurement suggest insulating ground state. On the other hand, at higher temperatures, the compound shows metallic behavior. The Seebeck coefficient also has negative to positive transition at low temperatures. The magnitude of Seebeck coefficient is less than 5 μV/K from 5 K to 390 K. Thermal conductivity of the compound increases with increasing temperature.

References

1 K. Biswas, J. He, I. D. Blum, C.-I. Wu, T. P. Hogan, D. N. Seidman, V. P. Dravid, and M. G. Kanatzidis, Nature 489, 414 (2012).

2 K. Chao and M. Larsson, edited by S. N. Karmakar, S. K. Maiti and J. Chowdhury (Springer Berlin Heidelberg, 2007), Vol. 156, p. 151.

3 G. A. Slack, *Handbook of Thermoelectrics* (CRC, Boca Raton, 1995).

4 G. J. Snyder and E. S. Toberer, Nat Mater 7, 105 (2008).

5 A. F. Ioffe, *Semiconductor thermoelements, and Thermoelectric cooling* (Infosearch, ltd., 1957).

6 H. J. Goldsmid, *Thermoelectric refrigeration* (Plenum Press, 1964).

7 L. D. Hicks and M. S. Dresselhaus, Phys. Rev. B 47, 12727 (1993).

8 T. Takeuchi, T. Kondo, T. Takami, H. Takahashi, H. Ikuta, U. Mizutani, K. Soda, R. Funahashi, M. Shikano, M. Mikami, S. Tsuda, T. Yokoya, S. Shin, and T. Muro, Phys. Rev. B 69, 125410 (2004).

9 J. M. O. Zide, D. Vashaee, Z. X. Bian, G. Zeng, J. E. Bowers, A. Shakouri, and A. C. Gossard, Phys. Rev. B 74, 205335 (2006).

10 G. Chen, Phys. Rev. B 57, 14958 (1998).

11 R. Venkatasubramanian, E. Siivola, T. Colpitts, and B. O'Quinn, Nature 413, 597 (2001).

12 H. Ohta, S. Kim, Y. Mune, T. Mizoguchi, K. Nomura, S. Ohta, T. Nomura, Y. Nakanishi, Y. Ikuhara, M. Hirano, H. Hosono, and K. Koumoto, Nat Mater 6, 129 (2007).

13 I. Terasaki, Y. Sasago, and K. Uchinokura, Phys. Rev. B 56, R12685 (1997).

14 I. Terasaki, Y. Sasago, and K. Uchinokura, in *Thermoelectrics, 1998. Proceedings ICT 98. XVII International Conference on*, 1998), p. 567.

15 K. Kurosaki, H. Muta, M. Uno, and S. Yamanaka, J. Alloy. Compd. 315, 234 (2001).

16 M. Lee, L. Viciu, L. Li, Y. Wang, M. L. Foo, S. Watauchi, R. A. Pascal Jr, R. J. Cava, and N. P. Ong, Nat Mater 5, 537 (2006).

17 Y. Wang, N. S. Rogado, R. J. Cava, and N. P. Ong, Nature 423, 425 (2003).

18 K. Takahata, Y. Iguchi, D. Tanaka, T. Itoh, and I. Terasaki, Phys. Rev. B 61, 12551 (2000).

19 D. G. Clarke, S. P. Strong, P. M. Chaikin, and E. I. Chashechkina, Science 279, 2071 (1998).

20 R. Ray, A. Ghoshray, K. Ghoshray, and S. Nakamura, Phys. Rev. B 59, 9454 (1999).

21 W. Koshibae, K. Tsutsui, and S. Maekawa, Phys. Rev. B 62, 6869 (2000).

22 S. Lambert, H. Leligny, and D. Grebille, J. Solid State Chem. 160, 322 (2001).

23 A. C. Masset, C. Michel, A. Maignan, M. Hervieu, O. Toulemonde, F. Studer, B. Raveau, and J. Hejtmanek, Phys. Rev. B 62, 166 (2000).

24 Q. Yao, D. L. Wang, L. D. Chen, X. Shi, and M. Zhou, J. Appl. Phys. 97, 103905 (2005).

25 T. A. Tyson, Z. Chen, Q. Jie, Q. Li, and J. J. Tu, Phys. Rev. B 79, 024109 (2009).

26 Y. N. Huang, B. C. Zhao, J. Fang, R. Ang, and Y. P. Sun, J. Appl. Phys. 110, 123713 (2011).

27 A. Satake, H. Tanaka, and T. Ohkawa, J. Appl. Phys. 96, 931 (2004).

28 Y. Wang, Y. Sui, X. J. Wang, W. H. Su, and X. Y. Liu, J. Appl. Phys. 107, 033708 (2010).

29 T. Fujii and I. Terasaki, in *Thermoelectrics, 2002. Proceedings ICT '02. Twenty-First International Conference on*, 2002), p. 199.

30 R. Funahashi, I. Matsubara, and S. Sodeoka, Appl. Phys. Lett. 76, 2385 (2000).

31 T. Yamamoto, I. Tsukada, K. Uchinokura, M. Takagi, T. Tsubone, M. Ichihara, and K. Kobayashi, Jpn. J. Appl. Phys. 39, L747 (2000).

32 H. Leligny, D. Grebille, O. Pérez, A. C. Masset, M. Herveieu, C. Michel, and B. Raveau, Comptes Rendus de l'Académie des Sciences - Series IIC - Chemistry 2, 409 (1999).

33 H. Leligny, D. Grebille, O. Pérez, A. C. Masset, M. Hervieu, and B. Raveau, Acta Crystallographica Section B 56, 173 (2000).

34 J. D. Baran, M. Molinari, N. Kulwongwit, F. Azough, R. Freer, D. Kepaptsoglou, Q. M. Ramasse, and S. C. Parker, The Journal of Physical Chemistry C 119, 21818 (2015).

35 T. Fujii, I. Terasaki, T. Watanabe, and A. Matsuda, Jpn. J. Appl. Phys. 41, L783 (2002).

36 R. D. Shannon, D. B. Rogers, C. T. Prewitt, and J. L. Gillson, Inorg. Chem. 10, 723 (1971).

37 M. Tanaka, M. Hasegawa, and H. Takei, Czech. J. Phys. 46, 2109 (1996).

38 H.-J. Noh, J. Jeong, J. Jeong, E.-J. Cho, S. B. Kim, K. Kim, B. I. Min, and H.-D. Kim, Phys. Rev. Lett. 102, 256404 (2009).

39 M. Tanaka, M. Hasegawa, T. Higuchi, T. Tsukamoto, Y. Tezuka, S. Shin, and H. Takei, Physica B 245, 157 (1998).

40 V. Eyert, R. Frésard, and A. Maignan, Chem. Mat. 20, 2370 (2008).

41 K. Kim, H. C. Choi, and B. I. Min, Phys. Rev. B 80, 035116 (2009).

42 R. D. Shannon, C. T. Prewitt, and D. B. Rogers, Inorg. Chem. 10, 719 (1971).

43 C. W. Hicks, A. S. Gibbs, A. P. Mackenzie, H. Takatsu, Y. Maeno, and E. A. Yelland, Phys. Rev. Lett. 109, 116401 (2012).

44 M. Hasegawa, I. Inagawa, M. Tanaka, I. Shirotani, and H. Takei, Solid State Commun. 121, 203 (2002).

45 K. P. Ong, D. J. Singh, and P. Wu, Phys. Rev. Lett. 104, 176601 (2010).

46 S. Ohta, T. Nomura, H. Ohta, and K. Koumoto, J. Appl. Phys. 97, 034106 (2005).

47 K. H. Lee, S. W. Kim, H. Ohta, and K. Koumoto, J. Appl. Phys. 100 (2006).

48 R. J. Bouchard and J. L. Gillson, Materials Research Bulletin 7, 873 (1972).

49 F. Lichtenberg, A. Catana, J. Mannhart, and D. G. Schlom, Appl. Phys. Lett. 60, 1138 (1992).

50 B. Hu, G. T. McCandless, V. O. Garlea, S. Stadler, Y. Xiong, J. Chan, E. W. Plummer, and R. Jin, Phys. Rev. B 84, 174411 (2011).

51 G. Cao, S. K. McCall, J. E. Crow, and R. P. Guertin, Phys. Rev. B 56, R5740 (1997).

52 N. Keawprak, R. Tu, and T. Goto, Mater. Trans. 49, 600 (2008).

53 T. Maekawa, K. Kurosaki, H. Muta, M. Uno, and S. Yamanaka, J. Alloy. Compd. 387, 56 (2005).

54 H. Yoshino, K. Murata, N. Shirakawa, Y. Nishihara, Y. Maeno, and T. Fujita, J. Phys. Soc. Jpn. 65, 1548 (1996).

55 Z. Xu, X. Xu, R. S. Freitas, Z. Long, M. Zhou, D. Fobes, M. Fang, P. Schiffer, Z. Mao, and Y. Liu, Phys. Rev. B 76, 094405 (2007).

56 S.-I. Ikeda, Y. Maeno, S. Nakatsuji, M. Kosaka, and Y. Uwatoko, Phys. Rev. B 62, R6089 (2000).

57 Q. Huang, J. W. Lynn, R. W. Erwin, J. Jarupatrakorn, and R. J. Cava, Phys. Rev. B 58, 8515 (1998).

58 M. A. Hossain, Z. Hu, M. W. Haverkort, T. Burnus, C. F. Chang, S. Klein, J. D. Denlinger, H. J. Lin, C. T. Chen, R. Mathieu, Y. Kaneko, Y. Tokura, S. Satow, Y. Yoshida, H. Takagi, A. Tanaka, I. S. Elfimov, G. A. Sawatzky, L. H. Tjeng, and A. Damascelli, Phys. Rev. Lett. 101, 016404 (2008).

59 Y. Wang, K. H. Lee, H. Hyuga, H. Kita, K. Inaba, H. Ohta, and K. Koumoto, Appl. Phys. Lett. 91 (2007).

60 R. Mathieu, A. Asamitsu, Y. Kaneko, J. P. He, X. Z. Yu, R. Kumai, Y. Onose, N. Takeshita, T. Arima, H. Takagi, and Y. Tokura, Phys. Rev. B 72, 092404 (2005).

61 H. Shaked, J. D. Jorgensen, S. Short, O. Chmaissem, S. I. Ikeda, and Y. Maeno, Phys. Rev. B 62, 8725 (2000).

62 T. D. Sparks, A. Gurlo, and D. R. Clarke, Journal of Materials Chemistry 22, 4631 (2012).

63 J. An, A. S. Sefat, D. J. Singh, and M.-H. Du, Phys. Rev. B 79, 075120 (2009).

64 H. F. Wang, K. F. Cai, H. Li, L. Wang, and C. W. Zhou, J. Alloy. Compd. 477, 519 (2009).

65 H. F. Wang, K. F. Cai, and S. Chen, J. Mater. Sci: Mater. Electron 23, 2289 (2012).

66 E. Brechtel, G. Cordier, and H. Schäfer, in *Zeitschrift für Naturforschung B*, 1979), Vol. 34, p. 777.

67 E. S. Landry, M. I. Hussein, and A. J. H. McGaughey, Phys. Rev. B 77, 184302 (2008).

68 I. Terasaki, Y. Sasago, and K. Uchinokura, Phys. Rev. B 56, R12685 (1997).

69 R. Jin, B. C. Sales, P. Khalifah, and D. Mandrus, Phys. Rev. Lett. 91, 217001 (2003).

70 J. N. Reimers and J. R. Dahn, J. Electrochem. Soc. 139, 2091 (1992).

71 M. Shikano and R. Funahashi, Appl. Phys. Lett. 82, 1851 (2003).

72 K. Koumoto, I. Terasaki, and R. Funahashi, MRS Bull. 31, 206 (2006).

73 D. A. Wright, Nature 181, 834 (1958).

74 T. Yamamoto, K. Uchinokura, and I. Tsukada, Phys. Rev. B 65, 184434 (2002).

75 H. W. Ou, J. F. Zhao, Y. Zhang, B. P. Xie, D. W. Shen, Y. Zhu, Z. Q. Yang, J. G. Che, X. G. Luo, X. H. Chen, M. Arita, K. Shimada, H. Namatame, M. Taniguchi, C. M. Cheng, K. D. Tsuei, and D. L. Feng, Phys. Rev. Lett. 102, 026806 (2009).

76 M. Hervieu, A. Maignan, C. Michel, V. Hardy, N. Créon, and B. Raveau, Phys. Rev. B 67, 045112 (2003).

77 S. F. Wang, A. Venimadhav, S. M. Guo, K. Chen, Q. Li, A. Soukiassian, D. G. Schlom, M. B. Katz, X. Q. Pan, W. W. Ng, M. D. Vaudin, and X. X. Xi, Appl. Phys. Lett. 94, 022110 (2009).

78 S. F. Wang, Z. C. Zhang, L. P. He, M. J. Chen, W. Yu, and G. S. Fu, Appl. Phys. Lett. 94, 162108 (2009).

79 D. J. Singh, Phys. Rev. B 61, 13397 (2000).

80 T. Itoh and I. Terasaki, Jpn. J. Appl. Phys. 39, 6658 (2000).

81 T. Mizokawa, L. H. Tjeng, P. G. Steeneken, N. B. Brookes, I. Tsukada, T. Yamamoto, and K. Uchinokura, Phys. Rev. B 64, 115104 (2001).

82 F. Chen, K. L. Stokes, and R. Funahashi, Appl. Phys. Lett. 81, 2379 (2002).

83 I. Terasaki, J. Appl. Phys. 110, 053705 (2011).

84 T. Motohashi, E. Naujalis, R. Ueda, K. Isawa, M. Karppinen, and H. Yamauchi, Appl. Phys. Lett. 79, 1480 (2001).

85 R. Funahashi and I. Matsubara, Appl. Phys. Lett. 79, 362 (2001).

86 R. Funahashi and M. Shikano, Appl. Phys. Lett. 81, 1459 (2002).

87 M. S. Dresselhaus, G. Chen, M. Y. Tang, R. G. Yang, H. Lee, D. Z. Wang, Z. F. Ren, J. P. Fleurial, and P. Gogna, Adv. Mater. 19, 1043 (2007).

88 M. Tanaka, M. Hasegawa, and H. Takei, J. Cryst. Growth 173, 440 (1997).

89 M. Hasegawa, T. Higuchi, M. Tanaka, T. Tsukamoto, S. Shin, and H. Takei, Mater. Trans. 42, 961 (2001).

90 H. Takatsu, S. Yonezawa, S. Mouri, S. Nakatsuji, K. Tanaka, and Y. Maeno, J. Phys. Soc. Jpn. 76, 7 (2007).

91 C. W. Hicks, A. S. Gibbs, A. P. Mackenzie, H. Takatsu, Y. Maeno, and E. A. Yelland, Phys. Rev. Lett. 109, 116401 (2012).

92 S. A. Grigera, R. S. Perry, A. J. Schofield, M. Chiao, S. R. Julian, G. G. Lonzarich, S. I. Ikeda, Y. Maeno, A. J. Millis, and A. P. Mackenzie, Science 294, 329 (2001).

93 R. S. Perry, L. M. Galvin, S. A. Grigera, L. Capogna, A. J. Schofield, A. P. Mackenzie, M. Chiao, S. R. Julian, S. I. Ikeda, S. Nakatsuji, Y. Maeno, and C. Pfleiderer, Phys. Rev. Lett. 86, 2661 (2001).

94 P. M. Chaikin and G. Beni, Phys. Rev. B 13, 647 (1976).

95 H. Guo, Y. Li, D. Urbina, B. Hu, R. Jin, T. Liu, D. Fobes, Z. Mao, E. W. Plummer, and J. Zhang, Phys. Rev. B 81, 155121 (2010).

96 E. Brechtel, G. Cordier, and H. Schafer, Z.Naturforsch.,B 34, 921 (1979).

97 S.-Q. Xia, C. Myers, and S. Bobev, European Journal of Inorganic Chemistry 2008, 4262 (2008).

98 A. I. Goldman, D. N. Argyriou, B. Ouladdiaf, T. Chatterji, A. Kreyssig, S. Nandi, N. Ni, S. L. Bud'ko, P. C. Canfield, and R. J. McQueeney, Phys. Rev. B 78, 100506 (2008).

99 C. Krellner, N. Caroca-Canales, A. Jesche, H. Rosner, A. Ormeci, and C. Geibel, Phys. Rev. B 78, 100504 (2008).

100 N. Ni, S. L. Bud'ko, A. Kreyssig, S. Nandi, G. E. Rustan, A. I. Goldman, S. Gupta, J. D. Corbett, A. Kracher, and P. C. Canfield, Phys. Rev. B 78, 014507 (2008).

101 N. Ni, S. Nandi, A. Kreyssig, A. I. Goldman, E. D. Mun, S. L. Bud'ko, and P. C. Canfield, Phys. Rev. B 78, 014523 (2008).

102 J. Q. Yan, A. Kreyssig, S. Nandi, N. Ni, S. L. Bud'ko, A. Kracher, R. J. McQueeney, R. W. McCallum, T. A. Lograsso, A. I. Goldman, and P. C. Canfield, Phys. Rev. B 78, 024516 (2008).

103 S. L. Brock, J. E. Greedan, and S. M. Kauzlarich, J. Solid State Chem. 113, 303 (1994).

104 K. Wang and C. Petrovic, Appl. Phys. Lett. 103 (2013).

105 Y. Singh, M. A. Green, Q. Huang, A. Kreyssig, R. J. McQueeney, D. C. Johnston, and A. I. Goldman, Phys. Rev. B 80, 100403 (2009).

106 Z. Ren, Z. Zhu, S. Jiang, X. Xu, Q. Tao, C. Wang, C. Feng, G. Cao, and Z. a. Xu, Phys. Rev. B 78, 052501 (2008).

107 B. Saparov and A. S. Sefat, J. Solid State Chem. 204, 32 (2013).

108 M. Rotter, M. Tegel, and D. Johrendt, Phys. Rev. Lett. 101, 107006 (2008).

109 A. S. Sefat, R. Jin, M. A. McGuire, B. C. Sales, D. J. Singh, and D. Mandrus, Phys. Rev. Lett. 101, 117004 (2008).

110 L. A. Patricia, Y. T. C. Ko, G. Jack, M. P. Chiara, M. C. Jacqueline, G. L. Gilbert, and E. S. Suchitra, Journal of Physics: Condensed Matter 21, 012208 (2009).

111 D. C. Johnston, *Handbook of Magnetic Materials* (Elsevier, Amsterdam, 1997).

112 P. Dai, Reviews of Modern Physics 87, 855 (2015).

113 G. Gordier and H. Z. N. Schaefer, B: Anorg. Chem., Org. Chem. 32, 383 (1977).

114 H. Hodovanets, E. D. Mun, A. Thaler, S. L. Bud'ko, and P. C. Canfield, Phys. Rev. B 83, 094508 (2011).

115 J. Li, C. E. Ekuma, I. Vekhter, M. Jarrell, J. Moreno, S. Stadler, A. B. Karki, and R. Jin, Phys. Rev. B 86, 195142 (2012).

116 B. Saparov and A. S. Sefat, (2013).

117 Y. Singh, A. Ellern, and D. C. Johnston, Phys. Rev. B 79, 094519 (2009).

118 T. Yildirim, Physica C: Superconductivity 469, 425 (2009).

119 Y. Su, P. Link, A. Schneidewind, T. Wolf, P. Adelmann, Y. Xiao, M. Meven, R. Mittal, M. Rotter, D. Johrendt, T. Brueckel, and M. Loewenhaupt, Phys. Rev. B 79, 064504 (2009).

120 Z. P. Yin, S. Lebègue, M. J. Han, B. P. Neal, S. Y. Savrasov, and W. E. Pickett, Phys. Rev. Lett. 101, 047001 (2008).

121 C. Kittel, *Introduction to Solid State Physics 4th ed.* (Wiley, New York, 1966).

122 E. S. R. Gopal, *Specific Heat At Low Temperatures* (Plenum, New York, 1966).

123 L. M. Volkova, Superconductor Science and Technology 21, 095019 (2008).

124 T. C. Ozawa and S. M. Kauzlarich, Science and Technology of Advanced Materials 9, 033003 (2008).

125 P. A. Lee, N. Nagaosa, and X.-G. Wen, Reviews of Modern Physics 78, 17 (2006).

126 M. A. Kastner, R. J. Birgeneau, G. Shirane, and Y. Endoh, Reviews of Modern Physics 70, 897 (1998).

127 M. Fujita, H. Hiraka, M. Matsuda, M. Matsuura, J. M. Tranquada, S. Wakimoto, G. Xu, and K. Yamada, J. Phys. Soc. Jpn. 81, 011007 (2011).

128 J. M. Tranquada, G. Xu, and I. A. Zaliznyak, Journal of Magnetism and Magnetic Materials 350, 148 (2014).

129 D. C. Johnston, Advances in Physics 59, 803 (2010).

130 W. Jinsheng, X. Guangyong, G. Genda, J. M. Tranquada, and R. J. Birgeneau, Reports on Progress in Physics 74, 124503 (2011).

131 G. R. Stewart, Reviews of Modern Physics 83, 1589 (2011).

132 J. G. Bednorz and K. A. Müller, Zeitschrift für Physik B Condensed Matter 64, 189 (1986).

133 R. Nath, V. O. Garlea, A. I. Goldman, and D. C. Johnston, Phys. Rev. B 81, 224513 (2010).

134 S. L. Brock and S. M. Kauzlarich, J. Alloy. Compd. 241, 82 (1996).

135 N. T. Stetson and S. M. Kauzlarich, Inorg. Chem. 30, 3969 (1991).

136 D. J. Singh, Phys. Rev. B 79, 153102 (2009).

137 F. J. Morin and J. P. Maita, Physical Review 96, 28 (1954).

138 T. Okita and Y. Makino, J. Phys. Soc. Jpn. 25, 120 (1968).

139 M. E. Fisher, Philos. Mag. 17, 1731 (1962).

Vita

Zhenyu Diao was born on October 08, 1988, in Tengzhou, Shandong Province, China. He graduated from University of Science and Technology of China, Hefei, China, with a Bachelor of Science in Applied Physics in July 2008. Later he received a Master of Philosophy in material science and engineering from The Chinese University of Hong Kong, Hong Kong, in Aug 2010. In Jan 2011, he came to Baton Rouge and started his research in Dr. Rongying Jin's group in the Department of Physics and Astronomy in Louisiana State University, Baton Rouge, Louisiana. He expects to receive his Doctor of Philosophy degree in physics in December, 2016.